UNIVERSITÀ DEGLI STUDI
DI MODENA E REGGIO EMILIA

DOTTORATO DI RICERCA IN MODELLISTICA, SIMULAZIONE COMPUTAZIONALE E CARATTERIZZAZIONE MULTISCALA PER LE SCIENZE DEI MATERIALI E DELLA VITA

Ciclo XXVII

Computational NMR Spectroscopy: a new way to determine the structure of Oxide Glasses

Candidato
Elisa Gambuzzi

Relatore (Tutor): Dott. Alfonso Pedone

Coordinatore del Dottorato e Direttore della Scuola di dottorato: Prof. Ledi Menabue

Yeni hayatim' a

Index

Preface iv
Chapter 1. Introduction to oxide glasses 1
1.1 History of glass technology 1
1.2 Glass generation from a thermodynamic point of view 3
1.3 General description of glass structure 4
1.4 Structural characterization: potentialities and limits of experimental techniques 7
1.5 Challenges of a synergetic experimental-computational approach 9
1.6 Glasses under study 11
1.7 Details about synthesis and origin of glass samples 13
Bibliography 14
Chapter 2. Computational methods 19
2.1 Generation of glass structural models 19
2.1.1 State of the art of glass structural modelling 19
2.1.2 Core-shell classical molecular dynamics 20
2.2 DFT Geometry Optimization of Structural Models and NMR parameter calculations 24
2.2.1 DFT calculations performed with CASTEP 24
2.2.2 Details for NMR parameter calculations 26
2.3 Simulation of NMR spectra 28
2.3.1 Background of computer simulations of solid state MAS NMR spectra 30
Bibliography 35
Chapter 3. ^{29}Si NMR spectroscopy: silicon environment in silicate and aluminosilcate glasses 39
3.1 Experiments of Silicon-29 NMR spectroscopy: information and challenges 39
3.2 Comparison between experimental and theoretical ^{29}Si MAS spectra 40
3.3 Silicon second coordination sphere: framework disorder 44
3.4 Silicon second coordination sphere: non-framework disorder 49
3.5 Relationships between ^{29}Si δ_{iso} and Si–O–T angles 52
3.6 Final remarks 53
Bibliography 55

Chapter 4. ^{27}Al NMR spectroscopy: aluminium environment in aluminosilicate glasses …… 57
4.1 Aluminium-27 NMR spectroscopy: experimental details and challenges …….. 57
4.2 Comparison of experimental and theoretical data …….. 58
4.3 Aluminium second coordination sphere: framework disorder 63
4.4 Aluminium second coordination sphere: non-framework disorder …….. 66
4.5 Relationships between ^{27}Al δ_{iso} and inter-tetrahedral angles 66
4.6 Final remarks …… 68
Bibliography ……..... 69
Chapter 5. ^{17}O NMR spectroscopy: oxygen environment in silicate and aluminosilicate glasses …… 71
5.1 Cation Distribution around Oxygen Atoms in Na–Ca Silicate Glasses …….. 72
5.2 Cation Distribution around Oxygen Atoms in Na–Ca Aluminosilicate Glasses …….. 78
5.3 ^{17}O NMR fingerprints of TBOs …… 84
5.4 Correlations between ^{17}O NMR Parameters and Local Geometry ……... 87
5.5 Final remarks …… 91
Bibliography ……..... 93
Chapter 6. ^{23}Na 3QMAS NMR spectroscopy: sodium environment in silicate and aluminosilicate glasses …….. 95
6.1 ^{23}Na 3QMAS spectra collection and fitting procedure …… 96
6.2 Validation of the MD-derived structural models …….. 99
6.3 Relationships between ^{23}Na NMR parameters and Na^+ local environment ……... 101
6.4 Local and medium-range environment: determination of the role of Na^+……... 105
6.5 Final remarks …… 106
Bibliography ……..... 107
Chapter 7. ^{43}Ca NMR spectroscopy: Ca environment in silicate and aluminosilicate glasses …… 111
7.1 History of the challenging ^{43}Ca NMR spectroscopy …… 112
7.2 ^{43}Ca 3QMAS spectra collection …… 113
7.3 Comparing Experimental and theoretical data: validation of the models …… 114

7.4 Correlations between ^{43}Ca NMR parameters and Ca local structural features 117
7.5 Dependence of local structural features on Ca role 120
7.6 Final remarks 121
Bibliography 122
Chapter 8. Conclusions 125
8.1 Interpretation and predictive ability of the MD-GIPAW method 125
8.2 Improvement of structural characterization of glasses 127
8.3 Future perspectives 129
Acknowledgements 131
Appendix A 133
Appendix B 135
Appendix C 137
List of Publications 139

Preface

Properties of glasses depend on their structures, as well as for all materials. However, the great advantage offered by glasses consists of the possibility to easily modify the structure by solely changing the composition. For example, the addition of CaO and Na_2O lows the T_g, and favors chemical reactivity, CeO_2 provides glasses with optical and antioxidant properties and the addition of Al_2O_3 confers chemical durability.

Then, the key to improve glass performances is to determine accurate relationships between structure, composition and properties.

However, glasses are amorphous systems and this imply that the full elucidation of their structure remains unreachable by using those powerful experimental techniques that allowed accurate determination of spatially ordered structures.

In the last decades, the development of algorithms for materials modelling and the emergence of powerful computing resources allowed scientists to get insight into glass features by modelling their structures and properties. Nowadays, simulation remains the most powerful, cheapest and most challenging approach for glass structure elucidation and deserves empowerment.

However, it is essential that structural models soundly reproduce the real system under study, then a continuative comparison between simulated data and available experimental counterparts on reference systems is mandatory.

All the work presented in this thesis is based on the synergetic computational-experimental approach, where the focal concept is:

experiment validates theory,

and theory explains experiment.

During the Ph. D., protocols for the modelling of oxide glasses were applied and optimized with the aim to i) obtain sound structural models for glasses of technological, geological and biomedical interest and ii) point out structure-properties relationships.

This manuscript presents the main part of the work done during the doctoral study: computational NMR spectroscopy of Na,Ca-containing silicate and aluminosilicate glasses of geological and technological interest and study of the correlation between NMR spectroscopic and structural properties. The investigation was carried out by employing molecular dynamics, computational NMR spectroscopy, and Solid State Magic Angle Spinning (MAS) NMR as experimental counterpart technique. NMR experiments were carried out at the "Laboratoire de Structure et Dynamique par Résonance Magnétique (LSDRM)" in the CEA Saclay research center, under the supervision of Dr. Thibault Charpentier.

The thesis is divided into 8 chapters, the first one introduces to the history of glass technology, to glass structure and structural characterization. Chapter 2 describes computational methods and details, while the remaining chapters present results and discussions. Each chapter is focused on findings relative to a specific NMR-active nucleus: ^{29}Si, ^{27}Al, ^{17}O, ^{23}Na and ^{43}Ca. A final chapter provides final remarks and future perspectives.

Beyond the main work, parallel works were carried out in collaboration with other research groups, but the discussion of the relative results is omitted from the present thesis to keep the dissertation fluent.

These works were focused on the elucidation of the structure of glasses for optical, biomedical and nuclear waste confinement applications. Some of the produced results have already been published and available in journal articles referred to in the "List of publications" (page 141).

In particular, Ce-containing phosphosilicate glasses were generated via classical molecular dynamics (MD) in continuation to the development of force field parameters for the Ce^{3+}–O and Ce^{4+}–O atom pairs. [1] The force field was validated by comparing the generated models with XRD experiments, for crystalline phases, and k-edge EXAFS results [2] for glasses for optical applications.

Subsequently the structure of Ce-doped bioglasses with antioxidant properties were generated, and modelled data were employed to explain the correlation between structure, bioactivity and antioxidant properties of the glasses.

A further computational study was conducted on Mo, Ba, Na-containing silicate glasses. These systems are considered as reference compositions for the study of the immobilization of ^{99}Mo radionuclide in nuclear waste confinement glasses. Polarizable Ion Model (PIM) molecular dynamics protocols were developed and validated by comparing the outcoming structural models with Neutron Diffraction data and *ab initio* MD-derived models. Further validations were conducted by comparing MAS NMR spectroscopy data with theoretical counterparts calculated within a project to training stable a brand-new implementation for GIPAW calculation in the VASP code [3], where time and memory management for large systems were optimized.

Bibliography

[1] Gambuzzi E, Pedone A. On the structure of Ce-containing silicophosphate glasses: a core–shell molecular dynamics investigation. Phys Chem Chem Phys 2014;16:21645–56. doi:10.1039/C4CP02577F.

[2] Rygel JL, Chen Y, Pantano CG, Shibata T, Du J, Kokou L, et al. Local Structure of Cerium in Aluminophosphate and Silicophosphate Glasses. J Am Ceram Soc 2011;94:2442–51. doi:10.1111/j.1551-2916.2011.04596.x.

[3] Kresse G, Furthmüller J. Efficient iterative schemes for ab initio total-energy calculations using a plane-wave basis set. Phys Rev B 1996;54:11169–86. doi:10.1103/PhysRevB.54.11169.

CHAPTER 1

Introduction to oxide glasses

History, structural characterization, systems under study

The present chapter provides a dissertation about the history of glass technology, glass structure, glass structural characterization and the synergetic experimental-computational approach adopted in this work.

1.1. History of glass technology

Humankind recognized the utility of oxide glasses since the Bronze age, when natural geological glasses, like obsidian, were employed to produce cutting-edge utensils and, later, jewels and artistic handicraft.

The first glass making procedure was developed about 5500 years ago in the Mesopotamian region and consisted of mixing sea sand, marine shells and seaweed ash, [1] heating the batch until melting (~1200°C - 1500°C) and rapidly cooling the melt. This is the melt-quench process. The obtained material is an overcooled liquid that, cooled below the glass transition temperature (T_g), presents the structural features of a liquid and the mechanical properties of a solid.

At the beginning, contrarily to pottery, glass vessel manufacturing required a very time- and energy-consuming procedure to obtain vessels starting from the high temperature melt material. Thus, glass was a luxury material addressed to creative vessel production only. Later, during the 1st century BC, glass blowing was discovered on the Mediterranean coast, and vessel production time and costs were drastically reduced. From then on, glass

became a widely used and requested material, especially in the Roman Empire where, starting from the 1st century AC, glass was also employed for architectural purposes.

Form the invention of blowing technique, glass technology remained essentially unvaried since 1848, when the engineer Henry Bessemer developed a quite expensive process to produce a continuous ribbon of flat glass by pushing the melt between rollers. Actually, the XIX century saw the passage from handcrafted to industrial glass production.

The last revolutionary improvement in industrial glass making technology is dated in the 1950s, when the float glass process allowed to obtain cheap, uniformly thick sheets of glass with a very flat surface. About the 90% of the currently employed flat glass is still produced with this method.

Since glasses were first manufactured, they had been as much widely employed as barely characterized materials: nothing was known but their approximate chemical composition. For tens of hundreds of years, the impossibility to investigate their properties contributed to limit the conception of a wide-range of glass applications. Chemical composition of glasses remained almost unvaried until the XIX century, when the glass making palette was extended from 15 to 40 elements. [2] The currently standard glass making elements Aluminum and Boron were discovered at the turning of XIX and XX centuries.

Nonetheless, the outstanding scientific development occurred in the XX century provided scientists with accurate and powerful techniques for structural and chemical characterization of materials, like diffraction and radiation absorption techniques. This development paved the way to the discovery of all the potentialities of oxide-based glasses.

Nowadays, the application of glasses goes much beyond architectural and containment purposes: glasses are employed in high-technology applications like optical devices fabrics, biomedical materials, electronic devices, photovoltaic applications, and nuclear waste confinement. [3–7]

1.2. Glass generation from a thermodynamic point of view

Glasses are super-cooled liquids: their topology is similar to the liquid phase under high-temperature conditions, but the fast cooling process produces a sudden raising of viscosity, impeding the structural units to arrange each other in a crystalline lattice. It is important to notice that the glass generation is not a phase transition of any kind, despite the remarkable change in the physical properties of a material through its *glass transition*.

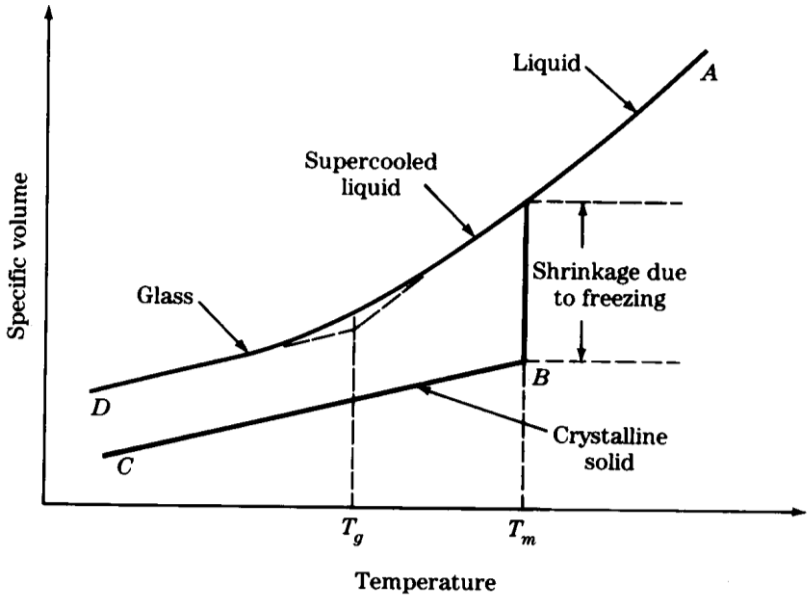

Figure 1.1. A comparison of volume variation in glass transition and crystallization processes.

The *glass transition process* of a liquid to an amorphous solid is a reversible process from a hard and brittle state into a molten state or rubber-like state. During the glass transition the thermodynamic equilibrium between solid and liquid phases is never reached: the crystallization process do not happen and glasses are metastable systems that tend to crystallize on the long period (thousands of years) or, faster, whether their composition favors chemical zoning having a stoichiometry similar to crystalline compounds. Contrarily to crystallization process, the glass transition is not characterized by a sudden change in thermodynamic properties, like specific volume (**Figure 1.1**) or enthalpy, at a certain temperature. Rather, the glass transition temperature, T_g, is defined as the temperature at which the viscosity of the material is equal to $10^{13.5}$ Pa·s. Further, the T_g can be outlined on the plot of heat capacity versus T during fast cooling. This plot is similar to the trend of specific volume shown in **Figure 1.1**. T_g corresponds to the intersection of the lines coinciding with the slopes of the two different linear regions defined in **Figure 1.1** as "glass" and "liquid".

Below the T_g, an amorphous material, may be a liquid or a rubber-like material, exhibits the mechanical properties of an amorphous solid.

1.3. General description of glass structure

Oxide based glasses are solid materials where "structural units" characterized by short-range order (within 2-3 atoms) are arranged, with respect to each other, with no special order. Thus, contrarily to crystalline materials, glasses lack the translational properties of identical unit cells. Structural units are tetrahedra $(T^{n+}O_{4/2})^{(8-n)}$, where T are *network former*

cations (Si, Al, B, etc…), eventually linking each other by sharing Oxygen atoms, named *bridging oxygen* atoms (BOs).

In the 1920s, empirical observation led Goldschmith [8] to define as glass former oxides those T_mO_n oxides where T cations present tetrahedral coordination in the molten phase.

Before the 1930s, glasses were meant to be an ensemble of nanocrystals (~20 Å) disposed with no reciprocal order, but in 1932 Zachariasen [9] proposed a valid model for the structure of oxide-based glasses. The basic idea was derived by the observation that mechanical properties of glasses are similar to those of crystals of the same composition. Hence, Zachariasen concluded that atoms in a glass are linked together by the same forces as in crystals. This supposition lead to the elaboration of the Continuous Random Network, shown in **Fig. 1.2** [9], which rules are:

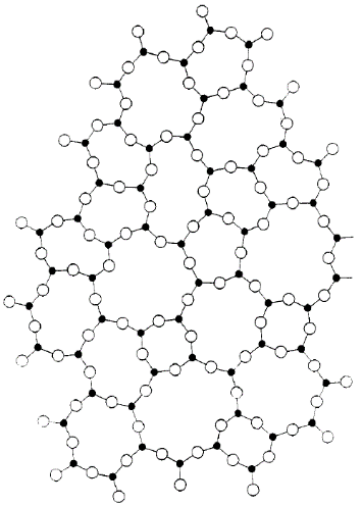

Figure 1.2. The Continuous Random Netowrk proposed by Zachariasen (1932)

1. oxygen atoms are linked to no more than 2 former atoms, T;
2. the oxygen coordination around T is small (i.e.: 3 or 4);
3. oxygen polyhedra do share corners but not edges or faces;
4. at least three corners are shared.

Nowadays, about 80 years later, we know that these rules are respected in most cases, except for some rare exceptions that can be present in some

cases, like tricluster Oxygen (TBO, O atoms bonded to 3 former atoms in tetrahedral coordination) or 2-merbers rings that imply edge-sharing. [10–12] Nonetheless, the addition of *network modifier oxides* (M_mO_n) to glass composition introduces O atoms that can be employed by some network former cations to fulfill the tetrahedral coordination. In this case, M cations locally compensate the consequent framework negative charge. The outcoming structure is described by the *Compensated Continuous Random Network*. The charge compensation is preferably conducted by low field strength cations (i.e.: Na^+, Li^+). When the tetrahedral coordination of all T cations is reached, the introduction of further M_mO_n provides *non-bridging oxygen* atoms (NBOs) that depolymerize the network, while M cations occupy depolymerized regions. In 1985, the structure of modified glasses where described by Greaves [13] in the *Modified Random Network* model (**Fig. 1.3** [13]).

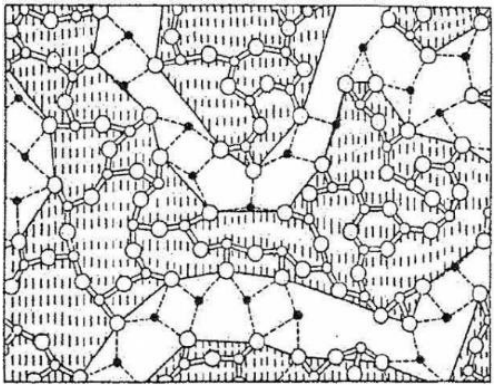

Figure 1.3. The Modified Random Network model proposed by Greaves (1985)

Beyond former and modifier oxides, *intermediate oxides* (R_mO_n), provide cations, R, which can behave as network former or extra-framework cation depending on glass overall composition. When network charge compensation is required and no modifier cation (M) is available, intermediate cations (R) assume higher coordination and exit the glass network.

In 1971, Stanworth [14] proposed a classification of glass-forming oxides based on electronegativity of cations in the cation–O bond. Highly electronegative cations, which form covalent bonds, are network former (i.e.: Si^{4+}, B^{3+}, P^{5+}, Ge^{2+}). Intermediate oxides present less covalent R–O bonds (Al^{3+}, Pb^{2+}), while modifier oxides present basically ionic M–O, and M cations have low ionic strength (alkali and alkaline-earth ions).

1.4. Structural characterization: potentialities and limits of experimental techniques

The structure of glasses lacks of symmetry in the coordination of extra-framework ions and lacks of periodicity for medium- and long-range structure. This entails that all those powerful diffraction techniques that allow the full elucidation of periodic system structures (i.e. crystals), provide few information on the overall structure of a glass. This information is limited to average bond lengths and coordination numbers of cations and is usually provided by Extended X-Ray Absorption Fine Structure (EXAFS), X-Ray Diffraction (XRD) and Neutron Diffraction (ND). Diffraction patterns of glasses can also provide a rough idea of the level of disorder of the medium and long-range structure of a given sample.

However, the characterization of medium-range structure can be supported by other absorption techniques. For example, Raman spectroscopy is useful to investigate the polymerization of glass network, because it provides information on the presence of TO_4 isolated tetrahedra, T_2O_6 chain links, T_2O_5 sheet units, etc… [15]

Infra-Red (IR) spectroscopy is sensitive to the local environment because the vibrational modes of structural units in a glass are assumed to be independent. [16] Quantitative information can be obtained from the detection of T–O–T symmetric and asymmetric stretching and bending modes, as well as for valence angles (O–T–O) bending modes. [17,18]

Among experimental techniques, solid state Nuclear Magnetic Resonance (NMR) is one of the most challenging because it provides information on both short- and medium-range environment of NMR-active nuclei. Nuclear probes provide different response depending on the chemical and topological nature of their neighborhood, making NMR spectroscopy a very sensitive technique.

In the present thesis, solid state Magic Angle Spinning (MAS) NMR spectroscopy is the reference experimental technique for glass structure investigation. MAS is based on the idea that orientation-dependent anisotropic interaction, which cause significant band broadening in solid state samples, can be averaged to zero by rapidly rotating the sample about the axis of the sample holder. The axis is inclined at the magic angle, $\theta_m = \arctan\sqrt{2} = 54{,}7356°$, with respect to the direction of the external magnetic field, **B**. The MAS technique reduce anisotropic interactions and leaves the isotropic ones (for spin-1/2 nuclei) allowing to get more accurate and interpretable NMR spectra of solid samples.

Nonetheless, the interpretation of NMR experiments on multicomponent glasses can be ambiguous due to the noticeable chemical and topological variability in samples. The interpretation can be carried out by following two paths.

a) The first consists of comparing the data obtained from glasses to NMR response of crystalline samples having similar compositions,

subsequently trying to assign the peaks in the glass spectra or by the principle of analogy.

b) The second, more recent, approach is the *experimental-computational* method [19], which was adopted during the work presented in this thesis and is described in next paragraph.

1.5. Challenges of a synergetic experimental-computational approach

The synergetic experimental-computational approach lies in the concept that experiment verifies the theory and theory explains experiment.

Actually, a model is sound and useful whether it reproduces chemical and physical properties of interest of the studied system. The accomplishment of this condition is the consequence of a well-calibrated computational method, where all protocols and parameters are chosen properly by a continuative comparison between computed data and reference experimental counterparts, during all the phases of the development of the computational protocol. Experimental counterpart must be similar to systems under study from a chemical-physical point of view and must have been very accurately characterized. In this viewpoint, *experiment validates the theory*.

In the specific case of structural models, EXAFS, XRD and ND data are often employed as experimental references. [20–27]

Once the theory is validated, the computational protocol can be applied to the interpretation of more complex experimental information. **Figure 1.4** shows a scheme of the experimental-computational approach adopted during this research work [19].

For a given glass sample, which structure is unknown, we generate a structural model via classical Molecular Dynamics (MD) simulations. Contrarily to the sample, the structure of the model is well-known. On one hand, we process the sample, collect NMR spectra and extract NMR parameters. On the other hand, we submit MD-derived models to NMR parameters calculations by plane waves Density Functional Theory (DFT) formalism and then simulate the NMR spectra with a homemade code[28] based on the resolution of spin-effective Hamiltonians. The theory underlying the simulation of NMR spectra will be presented more in detail in the following chapter. Once we have both experimental and theoretical counterparts, we compare them and check the agreement. If there are discrepancies, we undertake an iterative process that consists of: i) refinement of the structural model by adjusting simulation parameters (i.e.:

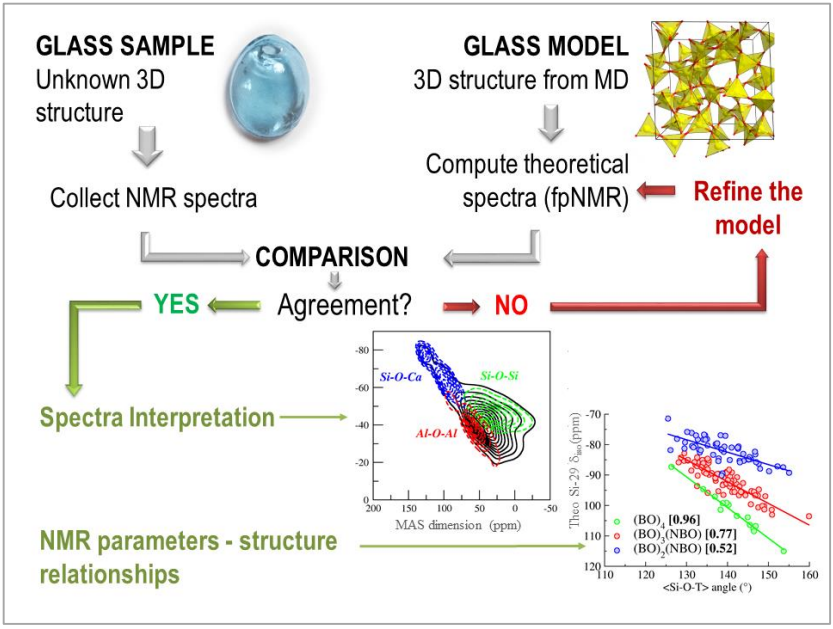

Figure 1.4. A scheme of the experimental-computational approach

quench rate, interatomic potentials, length of the simulation) and ii) re-calculation of NMR parameters and spectra simulation. The iterative process continues until a good agreement between experimental and theoretical NMR data is reached.

If the agreement is good, it is possible to proceed with peak assignation and spectra interpretation and with the elaboration of relationships between NMR parameters and structure.

It is worth noticing that the computational protocol for NMR parameter calculation was previously validated for all investigated NMR-active nuclei (^{17}O, ^{29}Si, ^{27}Al, ^{23}Na, ^{43}Ca). For this procedure, crystalline phases that are accurately characterized in terms of structure and NMR response were employed to test the soundness of the results of the DFT calculations. **Chapter 2** presents a more exhaustive description of computational protocols at the MD and DFT levels.

1.6. Glasses under study

Table 1.1. Composition (mol%) of the glasses.

glasses		SiO_2	Al_2O_3	Na_2O	CaO
silicate	CS	50%	---	---	50%
	NS	75%	---	25%	---
	CSN	60%	---	20%	20%
aluminosilicate	NAS	78%	11%	11%	---
	CAS	60%	20%	---	20%
	CASN	60%	10%	10%	20%

The target systems of the research presented in the following chapters are Ca, Na silicate and aluminosilicate glasses. These kind of glasses, which compositions are listed in **Table 1.1**, are interesting from both a geological and a technological point of view, being simplified versions of more complex systems like magmas and glasses for advanced and basic applications. In fact, their practical use ranges from optic fibers manufacturing to high-level nuclear waste confinement. Moreover, SiO_2 and Al_2O_3 are the main constituents of Earth's crust and containments, where they are present together with many other oxides to form very complex multicomponent materials.

Being so important, these glasses inspired many investigations about thermodynamics and transport properties, heat capacity of melts, silica activity and viscosity. [15, 29–37] The awareness that physical properties of amorphous materials depend very strongly on structure, and that glass structure depends, in turn, on chemical composition led to many experimental structural investigations. [12, 30, 38–41] However, the necessity to depict more accurate descriptions of short- and medium-range structural arrangements pushed the present work on structural characterization.

The state of the art on ternary and quaternary silicate and aluminosilicate composition provided a clear idea of general structural features. Indeed, their structure can be described by a combination of the Compensated Continuous Random Network and the Modified Random Network (see section 1.3). The network has been understood in terms of interconnected $(SiO_{4/2})^{4-}$ and, eventually $(AlO_{4/2})^{5-}$, tetrahedra. Non-framework cations can locally compensate the excess of negative charge of Al-containing networks and/or

depolymerize networks by forming non-bridging oxygen atoms NBOs (i.e. oxygen atoms connected to only one network former cation).

NMR spectroscopy, being so sensitive to short- and medium-range environment of probe nuclei, is challenging for providing more details on glass structures, like Q^n speciation of network formers, network chemical disorder, etc... Each nuclei provide signals that generate spectra very rich of structural information. In the present thesis, NMR spectroscopy of all NMR-active nuclei available for the aforementioned compositions were considered. The difficulties of interpretation of experimental spectra were overcame by the employment of computational NMR spectroscopy. The coupling of experimental and theoretical ^{29}Si, ^{27}Al, ^{17}O, ^{23}Na and ^{43}Ca NMR spectroscopies allowed us to depict accurate descriptions of short- and medium-range structural arrangements in Ca,Na-containing silicate and aluminosilicate glasses.

1.7. Details about synthesis and origin of glass samples

The present thesis is organized as to present NMR spectroscopy procedures and details, whilst does not focus on synthesis procedures of glass samples. This choice is due to the fact that synthesis were not carried out in our laboratory and procedures are described in already published papers.

Among the 6 compositions listed in **Table 1.1**, only four of them were synthesized by some of my collaborators during their research activity. Actually, CSN, CAS and CASN samples were synthesized by Angeli et al. [42] in 2007, and kindly granted to Thibault Charpentier for the collection of ^{29}Si MAS spectra at Laboratoire de Structure et Dynamique par Résonance

Magnétique (LSDRM). NAS glass was synthesized by Daniel Caurant on purpose for this research activity and its synthesis procedure is reported in reference [43].

All samples were synthesized by melting and quenching oxides and carbonates, some of which were enriched in NMR-active isotopes, as declared in the dedicated chapters together with NMR experimental data acquisition protocols.

CS and CN compositions have no corresponding experimental counterpart. However, experimental ^{17}O NMR data acquired on similar compositions by Stebbins and Xue in two works dated 2003 [44] and 2006 [45] were integrated in our computational-experimental method to provide new insights on Oxygen environment. CS and CN synthesis details are described in ref. [45] and [44], respectively.

Bibliography

[1] Kühne K. Zur Kenntnis silikatischer Werkstoffe und der Technologie ihrer Herstellung. 2 Jahrtausend, Berlin: Z. Akademie-Verlag; 1969.

[2] Kühnert H. Briefe und Dokumente zur Geschichte des VEB Optik Jenaer Glaswerk Schott & Genossen. Jena: n.d.

[3] Donald IW, Metcalfe BL, Taylor RNJ. The immobilization of high level radioactive wastes using ceramics and glasses. J Mater Sci 1997;32:5857–87.

[4] Stefanovsky SV, Ptashkin AG, Knyazev OA, Dmitriev SA, Yudintsev SV, Nikonov BS. Inductive cold crucible melting of actinide-bearing murataite-based ceramics. J Alloys Compd 2007;444-445:438–42. doi:10.1016/j.jallcom.2007.01.067.

[5] Lee J-C, Kim TG, Lee W, Han S-H, Sung Y-M. Growth of CdS Nanorod-Coated TiO_2 Nanowires on Conductive Glass for Photovoltaic Applications. Cryst Growth Des 2009;9:4519–23. doi:10.1021/cg9005373.

[6] Jones JR. Review of bioactive glass: From Hench to hybrids. Acta Biomater 2013;9:4457–86. doi:10.1016/j.actbio.2012.08.023.

[7] Sanghera J., Aggarwal I. Active and passive chalcogenide glass optical fibers for IR applications: a review. J Non-Cryst Solids 1999;256-257:6–16. doi:10.1016/S0022-3093(99)00484-6.

[8] Goldschmidt VM. Geochemische Verteilungsgesetze der Elemente VIII. Vid Akad Skr Oslo 1926;8:137.

[9] Zachariasen WH. The atomic arrangement in glass. J Am Chem Soc 1932;54:3841–51. doi:10.1021/ja01349a006.
[10] Tossell JA, Horbach J. O Triclusters Revisited: Classical MD and Quantum Cluster Results for Glasses of Composition (Al_2O_3)2(SiO_2). J Phys Chem B 2005;109:1794–7. doi:10.1021/jp0454873.
[11] Pedone A, Gambuzzi E, Malavasi G, Menziani MC. First-principles simulations of the 27Al and 17O solid-state NMR spectra of the CaAl2Si3O10 glass. Theor Chem Acc 2012;131. doi:10.1007/s00214-012-1147-5.
[12] Stebbins JF, Xu Z. NMR evidence for excess non-bridging oxygen in an aluminosilicate glass. Nature 1997;390:60–2.
[13] Greaves GN. EXAFS and the structure of glass. J Non-Cryst Solids 1985;71:203–17. doi:10.1016/0022-3093(85)90289-3.
[14] Stanworth JE. Oxide Glass Formation from the Melt. J Am Ceram Soc 1971;54:61–3. doi:10.1111/j.1151-2916.1971.tb12176.x.
[15] McMillian P. Structural studies of silicate glasses and melts-Applications and limitations of Raman spectroscopy. Am Min 1984;69:622–44.
[16] Tarte P. Physics in Non-Crystalline solids. Amsterdam: Elsevier; 1964.
[17] Efimov AM. Quantitative IR spectroscopy: Applications to studying glass structure and properties. J Non-Cryst Solids 1996;203:1–11. doi:10.1016/0022-3093(96)00327-4.
[18] Condrate RA. The Infrared and Raman Spectra of Glasses. In: Pye LD, Stevens HJ, LaCourse WC, editors. Introd. Glass Sci., Boston, MA: Springer US; 1972, p. 101–35.
[19] Charpentier T, Menziani MC, Pedone A. Computational simulations of solid state NMR spectra: a new era in structure determination of oxide glasses. RSC Adv 2013;3:10550. doi:10.1039/c3ra40627j.
[20] Du J, Kokou L, Rygel JL, Chen Y, Pantano CG, Woodman R, et al. Structure of Cerium Phosphate Glasses: Molecular Dynamics Simulation: Structure of Cerium Phosphate Glasses. J Am Ceram Soc 2011;94:2393–401. doi:10.1111/j.1551-2916.2011.04514.x.
[21] Kokou L, Du J. Short- and medium-range structures of cerium aluminophosphate glasses: A molecular dynamics study. J Non-Cryst Solids 2014;403:67–79. doi:10.1016/j.jnoncrysol.2014.07.014.
[22] Mountjoy G. Molecular dynamics, diffraction and EXAFS of rare earth phosphate glasses compared with predictions based on bond valence. J Non-Cryst Solids 2007;353:2029–34. doi:10.1016/j.jnoncrysol.2007.02.027.
[23] Cormier L, Ghaleb D, Neuville DR, Delaye J-M, Calas G. Chemical dependence of network topology of calcium aluminosilicate glasses: a computer simulation study. J Non-Cryst Solids 2003;332:255–70. doi:10.1016/j.jnoncrysol.2003.09.012.
[24] Du J, Corrales LR. Compositional dependence of the first sharp diffraction peaks in alkali silicate glasses: A molecular dynamics study. J Non-Cryst Solids 2006;352:3255–69. doi:10.1016/j.jnoncrysol.2006.05.025.
[25] Horbach J, Kob W, Binder K. Structural and dynamical properties of sodium silicate melts: an investigation by molecular dynamics computer simulation. Chem Geol 2001;174:87–101. doi:10.1016/S0009-2541(00)00309-0.
[26] Lusvardi G, Malavasi G, Cortada M, Menabue L, Menziani MC, Pedone A, et al. Elucidation of the Structural Role of Fluorine in Potentially Bioactive Glasses by Experimental and Computational Investigation. J Phys Chem B 2008;112:12730–9. doi:10.1021/jp803031z.

[27] McLaughlin J., Zwanziger J. Modeling glasses using the reverse Monte Carlo algorithm: addition of nuclear magnetic resonance and expanded coordination number constraints. J Mol Graph Model 1999;17:275–84. doi:10.1016/S1093-3263(99)00035-2.
[28] Pedone A, Charpentier T, Menziani MC. Multinuclear NMR of CaSiO3 glass: simulation from first-principles. Phys Chem Chem Phys 2010;12:6054–66. doi:10.1039/b924489a.
[29] Cormier L, Neuville DR. Ca and Na environments in Na2O–CaO–Al2O3–SiO2 glasses: influence of cation mixing and cation-network interactions. Chem Geol 2004;213:103–13. doi:10.1016/j.chemgeo.2004.08.049.
[30] Duxson P, Provis JL, Lukey GC, Separovic F, van Deventer JSJ. 29 Si NMR Study of Structural Ordering in Aluminosilicate Geopolymer Gels. Langmuir 2005;21:3028–36. doi:10.1021/la047336x.
[31] Neuville DR, Mysen BO. Role of aluminium in the silicate network: In situ, high-temperature study of glasses and melts on the join SiO2-NaAlO2. Geochim Cosmochim Acta 1996;60:1727–37. doi:10.1016/0016-7037(96)00049-X.
[32] Toplis MJ, Dingwell, Donald B., Hess K-W, Lenci T. Viscosity, fragility, and configurational entropy of melts along the join SiO2-NaAlSiO4. Am Min 1997;82:979–90.
[33] Leko VK, Mazurin OV. Analysis of Regularities in Composition Dependence of the Viscosity for Glass-Forming Oxide Melts: II. Viscosity of Ternary Alkali Aluminosilicate Melts. Glass Phys Chem 2003;29:16–27.
[34] Xue X, Kanzaki M, Neuville DR, Kawamoto T. Structure and properties of silicate melts and fluids. Geochim Cosmochim Acta 2004;68:5011. doi:10.1016/j.gca.2004.08.025.
[35] Provis JL, Duxson P, Lukey GC, van Deventer JSJ. Statistical Thermodynamic Model for Si/Al Ordering in Amorphous Aluminosilicates. Chem Mater 2005;17:2976–86. doi:10.1021/cm050219i.
[36] Neuville D. Viscosity, structure and mixing in (Ca, Na) silicate melts. Chem Geol 2006;229:28–41. doi:10.1016/j.chemgeo.2006.01.008.
[37] Richet P, Nidaira A, Neuville DR, Atake T. Aluminum speciation, vibrational entropy and short-range order in calcium aluminosilicate glasses. Geochim Cosmochim Acta 2009;73:3894–904. doi:10.1016/j.gca.2009.03.041.
[38] Neuville DR, Cormier L, Montouillout V, Massiot D. Local Al site distribution in aluminosilicate glasses by 27Al MQMAS NMR. J Non-Cryst Solids 2007;353:180–4. doi:10.1016/j.jnoncrysol.2006.09.035.
[39] Kuryaeva RG. Degree of polymerization of the CaAl2Si2O8 aluminosilicate glass. Glass Phys Chem 2006;32:505–10. doi:10.1134/S1087659606050026.
[40] Henderson GS, Neuville DR, Cormier L. An O K-edge XANES study of glasses and crystals in the CaO–Al2O3–SiO2 (CAS) system. Chem Geol 2009;259:54–62. doi:10.1016/j.chemgeo.2008.08.023.
[41] Mysen BO, Richet P. Silicate glasses and melts properties and structure. Amsterdam; Boston: Elsevier; 2005.
[42] Angeli F, Gaillard M, Jollivet P, Charpentier T. Contribution of 43Ca MAS NMR for probing the structural configuration of calcium in glass. Chem Phys Lett 2007;440:324–8. doi:10.1016/j.cplett.2007.04.036.
[43] Gambuzzi E, Pedone A, Menziani MC, Angeli F, Caurant D, Charpentier T. Probing silicon and aluminium chemical environments in silicate and aluminosilicate glasses by

solid state NMR spectroscopy and accurate first-principles calculations. Geochim Cosmochim Acta 2014;125:170–85. doi:10.1016/j.gca.2013.10.025.
[44] Lee SK, Stebbins JF. Nature of Cation Mixing and Ordering in Na-Ca Silicate Glasses and Melts. J Phys Chem B 2003;107:3141–8. doi:10.1021/jp027489y.
[45] Lee SK, Stebbins JF. Disorder and the extent of polymerization in calcium silicate and aluminosilicate glasses: O-17 NMR results and quantum chemical molecular orbital calculations. Geochim Cosmochim Acta 2006;70:4275–86. doi:10.1016/j.gca.2006.06.1550.

CHAPTER 2

Computational Methods

Molecular Dynamics, Density Functional Theory calculations, simulation of NMR spectra

2.1. Generation of glass structural models

2.1.1 State of the art of glass structural modelling

There are two possible approaches for the generation of glass models: Molecular Dynamics (MD) and Monte Carlo (MC) simulations.

MC is a stochastic molecular simulation, based on the principles of statistical mechanics independent from time. Therefore, no dynamical information can be obtained from MC simulations. The generation of the final structural model is guided, by the application of different algorithms, by the Boltzman weight of the system configuration in the chosen thermodynamic macroscopic conditions. Another option, is to guide the modelling by adjusting it until modelled quantities/characteristics (like atomic positions) provide the best consistence with reference experimental data. This is the Reverse Monte Carlo approach (RMC). More details are available in refs [1, 2].

MD simulations consist of the numerical solution of the classical equation of motions for atoms and molecules to obtain the time evolution of the system. It allows time-dependent phenomena to be followed. At each iteration, forces are calculated by positions accordingly to the potential energy surface (PES). Then motions are calculated from forces acting between atoms/molecules. The integration of equations of motion can be carried out by different algorithms, and the timestep is a crucial parameter to obtain sound structural

models. For a given system, the most appropriate timestep varies depending on the MD approach chosen to generate the model.

The PES can be calculated from a classical treatment of the system and usually coincides to the ground state: this is the case of Classical MD. Otherwise, for a more accurate description, the PES is built by taking into account electrons degree of freedom, thus involving a quantum mechanical formalism and *ab initio* calculations.

Of course, *ab initio* MD is ways more accurate than Classical MD, but also extremely more expensive in terms of computational time and resources. In the present work, we generated glass structural models via classical MD, adopting the core-shell model for an explicit treatment of oxide ions polarizability.

The *core-shell* model is not the only way to treat the polarizability of highly electronegative ions: the Polarizable Ion Model (PIM) [3, 4] and the Aspherical Ion Model (AIM) [5, 6] are also reliable methods, but they usually have higher computational costs.

2.1.2 Core-shell classical molecular dynamics

In the core-shell model, the more polarizable ions (oxygen in our case) are divided in a core bearing the major part of the mass (m_c) and a charge Y, and a shell bearing the remaining mass (m_s = atomic mass – m_c) and a charge X. The sum of X+Y usually gives the formal charge of the polarizable ion (i.e. -2 for O^{2-}, -1 for F^-, etc…). All other atoms are treated as points bearing formal charge (Si^{4+}, Al^{3+}, etc…) and cores and shells are coupled by a harmonic

spring potential that models charge migration in response to external electrostatic forces:

$$U(r_{c-s}) = \frac{k_{c-s}}{2}(r_{c-s})^2 \quad (2.1)$$

$k_{c\text{-}s}$ is the core–shell spring constant and $r_{c\text{-}s}$ is the distance between the core and the shell.

Oxygen shells (O_s) and Si, Al, Ca and Na cations are treated accordingly to the Born model, which assumes that two bodies, *i* and *j*, interact via long-range and short-range forces. In this work, they are calculated accordingly to Coulomb and Buckingham potentials, respectively. The Coulomb forces act between all species within a certain cut-off, whereas the Buckingham function models the Si–O_s, Al–O_s, O_s–O_s, Ca–O_s, Na–O_s short range interactions:

$$U(r_{ij}) = k\frac{q_i q_j}{r_{ij}} + A_{ij}e^{-\left(\frac{r_{ij}}{\rho_{ij}}\right)} - \frac{C_{ij}}{r_{ij}^6} \quad (2.2)$$

A_{ij}, ρ_{ij} and C_{ij} are the parameters of the Buckingham potential, q_i and q_j are the charges, k is $1/4\pi\varepsilon_0$ (where ε_0 is the dielectric constant) and r_{ij} is the distance between atoms *i* and *j*.

Finally, three-body screened harmonic potential is necessary to control the O_s–Si–O_s and O_s–Al–O_s angles and guide tetrahedral coordination:

$$U(\theta_{ijk}) = \frac{k_b}{2}(\theta_{ijk} - \theta_{ijk}^0)^2 \cdot e^{\left(-\frac{r_{ij}}{\rho}-\frac{r_{ik}}{\rho}\right)} \quad (2.3)$$

k_b is the three-body force constant, θ_{ijk} is the angle between atoms *i*, *j* and *k* and θ_{ijk}^0 is the reference angle between atoms *i*, *j* and *k* (109°). r_{ij} is the distance between *i* and *j*, r_{ik} is the distance between *i* and *k*, and ρ is a parameter.

Table 2.1. Shell model interatomic potential: analytic functions and parameters.

	Buckingham potential		
	A (eV)	ρ (Å)	C (eV Å^6)
O_s-O_s	22764.30	0.1490	27.88
Si-O_s	1283.91	0.32052	10.661580
Ca-O_s	2152.3566	0.309227	0.09944
Al-O_s	1460.3000	0.29912	0.0000000
	Three-body potential		
	k_b (eV rad^{-2})	θ_0 (deg)	ρ (Å)
O-Si-O	100.0	109.47	1.0
O-Al-O	100.0	109.47	1.0
	Core-shell harmonic potential		
	k_s (eV Å^{-2})	Y(e)	
O_c-O_s	74.92	-2.8482	

Table 2.1 reports all the parameters for the pairs and three-body terms which were developed in previous works. [7–13]

For each glass composition (**Table 1.1**), 3 structural models containing about 250 atoms each were generated. Models were created by cubic boxes treated with Periodic Boundary Conditions (PBC), which side were assessed accordingly to experimental densities, [14] available for all glasses except for CASN, or to density calculated by the Priven method [15], implemented in the SciGlass package [16] (CASN). Initial configurations were created by placing atoms in random positions in cubic boxes, by imposing the only constraint of a minimum distance between point charges of 2 Å.

Table 2.2. Glass densities.

Glass	CAS	NAS	CASN	CS	CN	CSN
Density [g·cm^{-3}]	2.624	2.369	2.641	2.901	2.418	2.657

The MD simulations were performed by DL_POLY package [17] and equations of motion were integrated by the leap-frog algorithm every 0.2 fs. This timestep is small enough to control the high frequency motion of the core-shell spring during MD simulations. [18] The trajectories were carried out in the NVT ensemble, applying the Berendsen thermostat [19]. Systems were heated and held at 3200 K for 100 ps, ensuring a suitable melting of the samples. Liquids were then cooled to 300 K at a nominal cooling rate of -5 K/ps, which is several orders of magnitude greater than rates achievable during synthesis procedures. Actually, nowadays available computational power does not allow to achieve experimental quench rate during *in silico* glass generation. Although it is well known that quench rate affects framework ordering, the literature reports several works where the adoption of this cooling rate provide sound final structures. [20–23] Resulting glass structures were subjected to a final equilibration run of 200 ps.

The presented force field and MD protocol allow to simulate sound MD-derived structural models both on the short- and medium-range order, as demonstrated by previous works. [8, 10–12, 24–28]

However, NMR properties are extremely sensitive to short-range structural features, like bond distances and valence angles, requiring models to be very accurate. To this, NMR parameters calculations was preceded by a finer structural optimization of MD outputs. All simulation boxes (3 per composition) underwent a 0 Kelvin isobaric structural relaxation at the DFT *ab initio* level of theory.

2.2. DFT Geometry Optimization of Structural Models and NMR parameter calculations

Computational techniques aimed to compute NMR parameters must take into account electrons and their interaction with forces internal and external to the system under study, i.e.: electron motion, electron correlation and applied external magnetic field.

The level of theory that must be referred to when dealing with NMR computational spectroscopy is the *quantum mechanics*. The accurate description of electronic-related properties for large and complex systems became possible with the advent of the Density Functional Theory (DFT). Its computational costs are relatively low when compared to post Hartree-Fock methods.

Nowadays, the DFT formalism has been implemented in all computational codes dedicated to NMR calculations.

2.2.1 DFT calculations performed with CASTEP

DFT calculations were carried out by the CASTEP code, [29] which exploits plane waves basis sets and manages periodic systems under periodic boundary conditions.

The computational efficiency of the code is guaranteed by the employment of pseudopotentials and the Projector Augmented Wave (PAW) formalism. In particular, NMR parameters calculation requires a PAW version that allows the reconstruction of the all electrons wave function in the presence of a magnetic field: the Gauge Including PAW (GIPAW). [30] Pseudopotentials

reduce computational costs as they allow core electron to be treated as a "frozen core" and only valence electron to be treated explicitly. For a given atom, many pseudopotentials can be developed by modifying the number of electron to be considered *core* and *valence*, and by shifting the energy level of *valence* orbitals.

DFT calculations were carried out adopting the generalized gradient approximation (GGA) PBE [31] functional, and the core-valence interactions were described by ultrasoft on-the-fly pseudopotentials generated by the CASTEP code. [32] For ^{17}O, the 2s and 2p orbitals were considered as valence states with a core radius of 1.3 Å; for ^{29}Si and ^{27}Al, a core radius of 1.8 Å was used with 3s and 3p valence orbitals; for ^{43}Ca, a core radius of 2.0 Å was used with 3s, 3p and 4s valence states, while ^{23}Na was treated with a core radius of 1.3 Å and 2s, 2p, 3s as valence orbitals.

For the PAW and GIPAW calculations we used two projectors in each *s* and *p* angular momentum channel for O, and in the *s*, *p* and *d* channel for Si, Al and Ca.

It is well known that in the PBE approximation, the energy of Ca 3d orbital is too low and the hybridization with O 2p orbitals is overestimated. [33] As a consequence, the ^{17}O chemical shifts computed with PBE are affected by very large errors (up to 124 ppm) for O sites close to Ca atoms. To overcome this problem a modified Ca pseudopotential with shifted 3d orbitals of 3.2 eV has been used as proposed by Profeta et al. [33] Details on pseudopotentials are summarized in **Table 2.3**.

Wave functions were expanded within the kinetic energy cut-off of 700 eV. This has been demonstrated to be long enough to reach energy and NMR parameters converged values. [34,35]

Constant pressure geometry optimisations of the MD-derived models were performed at the Γ point [36] and enabled only short-range relaxations at the *ab initio* level, whereas the information on medium-range structure, such as the connectivity of the glass-forming sites, is unvaried respect to the configuration obtained by classical MD.

Table 1.3 Pseudopotential details.

Atom	Valence configurations	Core radii [a.u.]	local channel projectors
^{29}Si	$3s^2\ 3p^2$	1.8	s, p and d
^{27}Al	$3s^2\ 3p^1$	1.8	s, p and d
^{17}O	$2s^2\ 2p^4$	1.3	s and p
^{43}Ca (*)	$3s^2\ 3p^6\ 4s^2$	2.0	s, p and d
^{23}Na	$2s^2\ 2p^6\ 3s^1$	1.3	s

(*) 3d level shifted as suggested by Profeta et Al.[33]

2.2.2 Details for NMR parameter calculations

The shielding tensor ($\overleftrightarrow{\sigma}$) is defined as the proportionality factor between the induced and the externally applied magnetic fields at the positions of the nuclei:

$$\overleftrightarrow{\sigma}(R) = -\vec{\mathrm{B}}^{ind}(R)/\vec{\mathrm{B}} \tag{2.4}$$

Where $\vec{\mathrm{B}}^{ind}(R)$ is the inomogeneous magnetic field induced by the external field $\vec{\mathrm{B}}$ and it is calculated according to the Biot-Savart law:

$$\vec{B}^{ind}(\vec{r}) = \frac{\mu_0}{4\pi}\int d^3\vec{r}\,' \frac{\vec{r}\,' - \vec{r}}{|\vec{r}\,' - \vec{r}|^3} \times \vec{\mathrm{j}}(\vec{r}\,') \tag{2.5}$$

Where the induced current, $\vec{\mathrm{j}}(\vec{r}\,')$, can be obtained from the first order perturbation theory. [37]

The isotropic chemical shift, δ_{iso}, is then obtained from the isotropic chemical shielding, σ_{iso}:

$$\sigma_{iso} = {}^{1}/_{3}\, Tr\{\overleftrightarrow{\sigma}\} \tag{2.6}$$

$$\delta_{iso} = -(\sigma_{iso} - \sigma_{ref}) \tag{2.7}$$

Where σ_{ref} is a reference isotropic shielding and is determined as the intercept of the trend line resulting from linear fit of σ_{iso} calculated on reference crystalline structure versus their experimental counterparts, δ_{iso}. In this work we adopted the σ_{ref} that were already available in the literature (**Table 2.4**): 322.1 ppm [27] for ^{29}Si, 555.2 ppm [34] for ^{27}Al, 260.5 for ^{17}O, 1134.1 ppm [35] for ^{43}Ca and 554.05 ppm [38] for ^{23}Na.

Quadrupolar nuclei (nuclear spin, I > ½) have quadrupolar parameters related to the traceless electric field gradient tensor, $V_{\alpha\beta}(\vec{r})$:

$$V_{\alpha\beta}(\vec{r}) = \frac{\partial E_{\alpha}(\vec{r})}{\partial r_{\beta}} - \frac{1}{3}\delta_{\alpha\beta}\sum_{\gamma}\frac{\partial E_{\gamma}(\vec{r})}{\partial r_{\gamma}} \tag{2.8}$$

where α, β and γ denote the Cartesian coordinates x, y, z and $E_{\alpha}(\vec{r})$ is the local electric field at the position $\vec{r}$. If the eigenvalues of the EFG tensor are labeled V_{xx}, V_{yy}, V_{zz} so that $|V_{zz}| > |V_{yy}| > |V_{xx}|$, then one can define the quadrupolar coupling constant,

$$C_Q = \frac{eQV_{zz}^{PAF}}{h} \tag{2.9}$$

where eQ is the quadrupole moment of the nucleus and h is the Plank's constant. The EFG tensor eigenvalues also provide the asymmetry parameter,

$$\eta_Q = \frac{V_{xx} - V_{yy}}{V_{zz}} \tag{2.10}$$

The quadrupole moment values, *eQ*, adopted for the calculation of C_Q were those determined by Pyykkö in 2008 via sophisticated post-Hatree-Fock calculations of the EFG: [39] 25.58 mB for ^{17}O, 40.9 mB for ^{43}Ca and 104 mB for ^{23}Na nuclei. Differently, eQ for ^{27}Al was calculated by scaling the *eQ* provided by Pyykkö, 146.6 mB, [39] by a factor of 0.956, thus obtaining 140.4 mB. In fact, Pyykkö's value was found to give slightly overestimated C_Q values respect to experimental counterparts [40] on crystalline samples (anorthite, andalusite, sillimanite, kyanite and α-alumina). The scaling factor was calculated as the slope of the linear fitting trend line of the comparison between the experimental [40] and theoretical ^{27}Al C_Q values, as explained in detail in ref. [24].

Table 2.4 Reference isotropic shieldings, σ_{ref} [ppm], and quadruole moments, *eQ* [mB] and respective bibliographic references.

Nucleus	σ_{ref} [ppm]	refs	*eQ* [mB]	refs
^{29}Si	332.1	[27]	---	---
^{27}Al	555.2	[34]	104.4	[24]
^{17}O	260.5	[27]	25.58	[39]
^{43}Ca (*)	1134.1	[35]	40.9	[39]
^{23}Na	554.05	[38]	104	[39]

2.3. Generation of NMR spectra

NMR spectra of the MD-derived structural models described in the following pages will be named hereafter as *theoretical* to distinguish them to those generated by using NMR parameters extracted from experimental measurements which are usually referred to as *experimental* spectra. For

each composition under study, theoretical spectra were obtained by *merging* the 3 DFT outputs coming from respective MD-derived models. Computational protocol, both at classical and ab initio levels, is summarized in **Figure 2.1**.

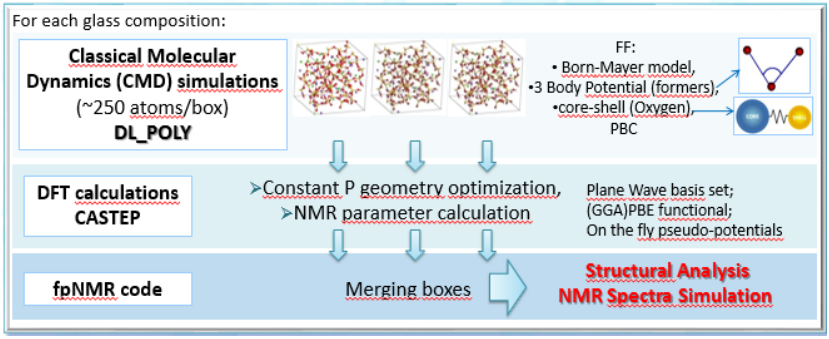

Figure 2.1. Summarized scheme of the computational protocol.

The simulation of the solid state MAS and 3QMAS NMR spectra from CASTEP outputs was carried out by means of the software fpNMR, developed by Thibault Charpentier. [35,41] For each atomic site, *i*, the NMR spectrum of interest, say $I_i(\vec{v})$, is calculated and then co-added to yield the final NMR spectra, $I(\vec{v}) = \sum_i I_i(\vec{v})$. However, in some cases, spectra simulation may require a more refined method to better account for NMR parameter distribution, like Kernel Density Estimation (KDE) [35,42]. KDE is also implemented in the fpNMR code and was exploited to simulate spectra starting from small nuclei populations, like ^{43}Ca 3QMAS spectra. The software allows the summation to be restricted to a given chemical speciation of the considered atom (Si(Q^3), Non-Bridging Oxygen, Al bonded to Tri-cluster Oxygen, etc…) and to merge the spectra of several structural models to increase the statistical data.

Moreover, the code performs statistical analysis of NMR data and their correlation with local structural features (bond length, bond angles, coordination number, etc…).

2.3.1 Background of computer simulations of solid state MAS NMR spectra

The simulation of MAS spectra of glass sample is quite demanding because computational techniques must account for time-dependent modulation (sample spinning) and the summation of signals from a large number of molecular orientation (*powder averaging*). Nowadays, codes running on personal computers can provide theoretical spectra in few seconds or minutes, even taking into account all relevant interactions of the spin systems. [35, 43–46]. This paragraph provides a concise summary of the theory of solid state NMR spectra simulation; more details can be found in the valuable series of reviews written by Mattias Edén on this topic. [47–49]
Simulation programs calculate time- or frequency-domain signal stepping through 3 main parts:

1) Initialization: provision of input data on experimental conditions and spin system characteristics;
2) spin dynamic calculations: evolution in time, during the NMR experiment, of the spin density operator, which describes the state of an ensemble of spin systems;
3) post-processing: calculated NMR signals are further processed (ex.: peak broadening) to provide the *theoretical* NMR spectra.

The core, and most time-consuming part, of the simulation is the second step. The evolution of spin systems experiencing anisotropic interactions in a rotating frame is described by the Irreducible Spherical Tensor (IST) [50–52] formalism.

Basically, within the IST formalism, the values of the individual components of tensors change, but the number of components is fixed, which means that the rank, *l*, of an IST in conserved upon rotation.

In fact, all NMR interactions can be reconstructed in terms of IST:

- NMR interactions depending on molecule properties, like the orientation relative to the direction of the static magnetic field, **B**, are given by a *spatial* tensor, $\overleftrightarrow{\mathbf{A}}^{(l)}_{\mathrm{NMR}}$.
- NMR interactions depending on spin angular momentum are represented by a *spin* tensor, which elements are spin operators represented by matrices, $\overleftrightarrow{\hat{\mathbf{T}}}^{(l)}_{\mathrm{NMR}}$.

As well known, interactions can be isotropic (orientation independent, 0th rank IST) or anisotropic (orientation dependent, 2nd rank IST).

Spectra simulation codes generally reconstruct the Hamiltonian representing the NMR interaction, by scalar product of IST, where each scalar product involves a scalar and a spin tensor:

$$\mathbf{H}_{\mathrm{NMR}} = \mathrm{C} \sum_{\mathrm{i}=0,2} \left[\overleftrightarrow{\mathbf{A}}^{(l)}_{\mathrm{NMR}}\right]^{\mathrm{L}} \left[\overleftrightarrow{\hat{\mathbf{T}}}^{(l)}_{\mathrm{NMR}}\right]^{\mathrm{L}} \tag{2.11}$$

The capital letter, L, means “laboratory reference frame”, where the *z* axis coincides with the direction of the applied magnetic field, **B**.

Once the Hamiltonian for the spin system is reconstructed, the density operator carries the information about the state of an ensemble of nuclear

spin systems. The Hamiltonian will cause the density operator to change throughout the NMR experiment.

The Schrödinger equation dictates how the spin density operator, and hence the nuclear spins, evolves in time and must be solved by employing an operator called the propagator. In practice, the propagator is estimated numerically and may then be used to calculate the spin density operator at any time point during the NMR experiment. The time-domain signal at a given time point is calculated as the trace of the product of an observable operator and the density operator at that given time point.

The procedure is repeated for a series of time points so that the time-domain signal, s(t), can be obtained and, subsequently, the corresponding NMR spectrum is calculated by Fourier transformation. It is worth noticing that the summarized procedure presented is referred to the generations of single molecular orientation signals in a static and rotating sample.

The reader who might be interested in the procedure for implementing the abovementioned formalism, for static and rotating samples, in C/C++ computer language should refer to [48].

Glass samples for solid-state NMR spectroscopy are usually powders. Then, NMR simulation codes dedicated to glass systems must be able to simulate spectra of powders comprising a large number of microscopically small crystals, through a procedure called powder averaging. In fact it is well known that the NMR time-domain signal and frequency-domain spectrum depend on the orientation of the molecule with respect to the static magnetic field direction.

There are many fundamental equations for calculating powder averages, and reference [49] explains in details how they may be implemented on a

computer, and which formalisms can be adopted to speed up the calculation (i.e.: carousel symmetry).

The fpNMR code was written by Thibault Charpentier and is still constantly improved (write to thibault.charpentier@cea.fr for an updated version). The basis of the formalism underlying the code was introduced and described in some previous papers [35, 41, 53], however the principal concepts are presented hereafter.

Starting from absolute shielding and electric field gradient tensors, given as Cartesian matrix representation with respect to the crystallographic axis, the chemical shift tensor and quadrupolar interaction tensors are obtained.

The diagonalization of the matrix representation of a given interaction, say **A**, provides 3 eigenvector which define the Principle Axis System (PAS) of the interaction. These eigenvalues are called principal-values and are denoted as $A_{\alpha\alpha}$ (α = x, y, z) and labelled according to the Haeberlen convention [54]$|A_{ZZ} - A_{iso}| \geq |A_{XX} - A_{iso}| \geq |A_{YY} - A_{iso}|$ where $A_{iso} = \frac{1}{3}\mathrm{Tr}\{\mathbf{A}\}$ is the isotropic component. However, the code deals with a different, more convenient notation, which uses 1 parameter: $\Delta_A = (A_{ZZ} - A_{iso})$ and $\eta_A = (A_{YY} - A_{XX})/\Delta_A$. The representation of **A** in PAS is then transformed as:

$$\begin{aligned} \boldsymbol{A}_{PAS} &= \begin{bmatrix} A_{xx} & & \\ & A_{yy} & \\ & & A_{zz} \end{bmatrix} \\ &= A_{iso} \\ &+ \Delta_A \begin{bmatrix} -\frac{1}{2(1+\eta_A)} & & \\ & -\frac{1}{2(1-\eta_A)} & \\ & & 1 \end{bmatrix} \end{aligned} \tag{2.12}$$

The contribution of each atomic site to the NMR frequency of the transition of interest, say $\nu(\alpha,\beta)$, can then be obtained in terms of the isotropic chemical shift, δ_{iso}, chemical shift anisotropy and asymmetry parameter, η_{CSA}, quadrupolar coupling constant, C_Q, and asymmetry parameter, η_Q, and the orientation (α,β) of the crystal with respect to the laboratory frame (*i.e.* the magnetic field frame), as well as the relative orientation of the two tensors.

The three Euler angles $(\alpha_A,\beta_A,\gamma_A)$ relate the PAS to the crystallographic axes frame.

The general formula of a 1D-NMR spectrum, $I(\nu(\alpha,\beta))$ (for a single site) is the following:

$$I(\nu) = \int d\alpha\, d\beta\, sin\beta \cdot \int dt\, e^{-2i\pi\nu t}\, e^{2i\nu(\alpha,\beta)t} \qquad (2.13)$$

$$= \int d\alpha\, d\beta\, sin\beta \cdot \delta\{\nu - \nu(\alpha,\beta)\}$$

To perform the powder averaging (i.e. the integration over (α,β)), the method of Alderman et al. [50] is used. This method combines an efficient partitioning of the (α,β) space into a triangular mesh.

In the case of sample rotation, as during magic angle spinning experiments, the NMR frequency becomes time-dependent and is Fourier expanded. In case of time-dependent experiments, three Euler angles $(\alpha_R,\beta_R,\gamma_R)$, which define the orientation of the PAS with respect to the rotor frame, are introduced. The powder averaging over the third Euler angle is at the origin of the positive intensity in MAS spectra [55]. However, the powder averaging is then performed as for a static sample (*i.e.* non spinning) as follows.

In fact, for the powder averaging, the same method as for 1D spectra is applied but using now a 2D *unit spectrum* $f^{(q)}(\nu_1,\nu_2)$. This gives an efficient general algorithm to compute a 2D-NMR spectrum.

In the case of a broad NMR parameter distribution, as a consequence of the small number of sites that can be considered using *ab initio* NMR calculations, simulated NMR spectra, especially 2D, can exhibit strong spurious spectral features (discretization noise). Generally, as done in many other spectroscopies (IR, RAMAN,…), a convolution with a Gaussian (or other distribution) in the frequency space (ν_1,ν_2) is employed to smooth the simulated spectrum.

Specific input files allow to specify experimental condition to be reproduced, like the applied magnetic field, the Larmor frequency, the quadrupole moment, the spinning rate of samples.

The present chapter introduced our method and all computational details needed for its reproduction. The following chapters will present results. Each chapter is focused on single-nucleus NMR spectroscopy and will discuss about the insight on glass structure and on NMR-structural parameters relationships that were achieved by exploiting structural models and by coupling theoretical and experimental counterparts.

Bibliography

[1] Frenkel D, Smit B. Understanding molecular simulation from algorithms to applications. San Diego: Academic Press; 2002.

[2] Landau DP. A guide to Monte Carlo simulations in statistical physics. 3rd ed. Cambridge ; New York: Cambridge University Press; 2009.

[3] Ainsworth RI, Di Tommaso D, Christie JK, de Leeuw NH. Polarizable force field development and molecular dynamics study of phosphate-based glasses. J Chem Phys 2012;137:234502. doi:10.1063/1.4770295.

[4] Maltz C. Polarizable-ion model for vibrationally excited alkali halides. Chem Phys Lett 1969;3:707–10. doi:10.1016/0009-2614(69)87016-8.

[5] Rowley AJ, Jemmer P, Wilson M, Madden PA. Evaluation of the many-body contributions to the interionic interactions in MgO. J Chem Phys 1998;108:10209. doi:10.1063/1.476481.

[6] Aguado A, Bernasconi L, Jahn S, Madden PA. Multipoles and interaction potentials in ionic materials from planewave-DFT calculations. Faraday Discuss 2003;124:171. doi:10.1039/b300319c.

[7] Malavasi G, Pedone A, Menziani MC. Study of the Structural Role of Gallium and Aluminum in 45S5 Bioactive Glasses by Molecular Dynamics Simulations. J Phys Chem B 2013;117:4142–50. doi:10.1021/jp400721g.
[8] Tilocca A, de Leeuw N, Cormack A. Shell-model molecular dynamics calculations of modified silicate glasses. Phys Rev B 2006;73. doi:10.1103/PhysRevB.73.104209.
[9] Di Tommaso D, Ainsworth RI, Tang E, de Leeuw NH. Modelling the structural evolution of ternary phosphate glasses from melts to solid amorphous materials. J Mater Chem B 2013;1:5054. doi:10.1039/c3tb20662a.
[10] Pedone A, Gambuzzi E, Menziani MC. Unambiguous Description of the Oxygen Environment in Multicomponent Aluminosilicate Glasses from ^{17}O Solid State NMR Computational Spectroscopy. J Phys Chem C 2012;116:14599–609. doi:10.1021/jp304802y.
[11] Tilocca A, Cormack AN, de Leeuw NH. The Structure of Bioactive Silicate Glasses: New Insight from Molecular Dynamics Simulations. Chem Mater 2007;19:95–103. doi:10.1021/cm061631g.
[12] Pedone A, Malavasi G, Menziani MC. Computational Insight into the Effect of CaO/MgO Substitution on the Structural Properties of Phospho-Silicate Bioactive Glasses. J Phys Chem C 2009;113:15723–30. doi:10.1021/jp904131t.
[13] Malik J, Tilocca A. Hydration Effects on the Structural and Vibrational Properties of Yttrium Aluminosilicate Glasses for in Situ Radiotherapy. J Phys Chem B 2013;117:14518–28. doi:10.1021/jp4073203.
[14] Bansal NP, Doremus RH. Handbook of glass properties. Orlando: Academic Press; 1986.
[15] Priven AI. General method for calculating the properties of oxide glasses and glass forming melts from their composition and temperature. Glass Technol 2004;45:244–54.
[16] Mazurin OV, Streltsina MV, Shvaiko-Shvaikovskaya TP, Leko TP, Priven AI. SciGlassTM. n.d.
[17] Smith W, Forester TR. DL_POLY_2.0: A general-purpose parallel molecular dynamics simulation package. J Mol Graph 1996;14:136–41. doi:10.1016/S0263-7855(96)00043-4.
[18] Tilocca A. Short- and medium-range structure of multicomponent bioactive glasses and melts: An assessment of the performances of shell-model and rigid-ion potentials. J Chem Phys 2008;129:084504. doi:10.1063/1.2972146.
[19] Berendsen HJC, Postma JPM, van Gunsteren WF, DiNola A, Haak JR. Molecular dynamics with coupling to an external bath. J Chem Phys 1984;81:3684. doi:10.1063/1.448118.
[20] Štich I, Car R, Parrinello M. Amorphous silicon studied by ab initio molecular dynamics: Preparation, structure, and properties. Phys Rev B 1991;44:11092–104. doi:10.1103/PhysRevB.44.11092.
[21] Vollmayr K, Kob W, Binder K. Cooling-rate effects in amorphous silica: A computer-simulation study. Phys Rev B 1996;54:15808–27. doi:10.1103/PhysRevB.54.15808.
[22] Cormack AN, Park B, Yuan X, Helebrant A, Maryska M. 5th ESG Conf., Prague: Czech Glass Society; 1999, p. B4–15.
[23] Corrales LR, Du J. Thermal kinetics of glass simulations. Phys Chem Glas 2005;46:420–4.
[24] Gambuzzi E, Pedone A, Menziani MC, Angeli F, Caurant D, Charpentier T. Probing silicon and aluminium chemical environments in silicate and aluminosilicate glasses by

solid state NMR spectroscopy and accurate first-principles calculations. Geochim Cosmochim Acta 2014;125:170–85. doi:10.1016/j.gca.2013.10.025.
[25] Pedone A, Gambuzzi E, Malavasi G, Menziani MC. First-principles simulations of the 27Al and 17O solid-state NMR spectra of the CaAl2Si3O10 glass. Theor Chem Acc 2012;131. doi:10.1007/s00214-012-1147-5.
[26] Gambuzzi E, Charpentier T, Menziani MC, Pedone A. Computational interpretation of 23Na MQMAS NMR spectra: A comprehensive investigation of the Na environment in silicate glasses. Chem Phys Lett 2014;612:56–61. doi:10.1016/j.cplett.2014.08.004.
[27] Pedone A, Charpentier T, Malavasi G, Menziani MC. New Insights into the Atomic Structure of 45S5 Bioglass by Means of Solid-State NMR Spectroscopy and Accurate First-Principles Simulations. Chem Mater 2010;22:5644–52. doi:10.1021/cm102089c.
[28] Pedone A. Properties Calculations of Silica-Based Glasses by Atomistic Simulations Techniques: A Review. J Phys Chem C 2009;113:20773–84. doi:10.1021/jp9071263.
[29] Segall MD, Lindan PJD, Probert MJ, Pickard CJ, Hasnip PJ, Clark SJ, et al. First-principles simulation: ideas, illustrations and the CASTEP code. J Phys Condens Matter 2002;14:2717–44. doi:10.1088/0953-8984/14/11/301.
[30] Pickard C, Mauri F. All-electron magnetic response with pseudopotentials: NMR chemical shifts. Phys Rev B 2001;63. doi:10.1103/PhysRevB.63.245101.
[31] Perdew JP, Burke K, Ernzerhof M. Generalized Gradient Approximation Made Simple. Phys Rev Lett 1996;77:3865–8. doi:10.1103/PhysRevLett.77.3865.
[32] Yates J, Pickard C, Mauri F. Calculation of NMR chemical shifts for extended systems using ultrasoft pseudopotentials. Phys Rev B 2007;76. doi:10.1103/PhysRevB.76.024401.
[33] Profeta M, Benoit M, Mauri F, Pickard CJ. First-Principles Calculation of the ^{17}O NMR Parameters in Ca Oxide and Ca Aluminosilicates: the Partially Covalent Nature of the Ca−O Bond, a Challenge for Density Functional Theory. J Am Chem Soc 2004;126:12628–35. doi:10.1021/ja0490830.
[34] Choi M, Matsunaga K, Oba F, Tanaka I. 27Al NMR Chemical Shifts in Oxide Crystals: A First-Principles Study. J Phys Chem C 2009;113:3869–73. doi:10.1021/jp810484j.
[35] Pedone A, Charpentier T, Menziani MC. Multinuclear NMR of CaSiO3 glass: simulation from first-principles. Phys Chem Chem Phys 2010;12:6054–66. doi:10.1039/b924489a.
[36] Monkhorst HJ, Pack JD. Special points for Brillouin-zone integrations. Phys Rev B 1976;13:5188–92. doi:10.1103/PhysRevB.13.5188.
[37] Günther H. NMR spectroscopy: basic principles, concepts, and applications in chemistry. 2nd ed. Chichester ; New York: Wiley; 1995.
[38] Pedone A, Charpentier T, Menziani MC. The structure of fluoride-containing bioactive glasses: new insights from first-principles calculations and solid state NMR spectroscopy. J Mater Chem 2012;22:12599. doi:10.1039/c2jm30890h.
[39] Pyykkö P. Year-2008 nuclear quadrupole moments. Mol Phys 2008;106:1965–74. doi:10.1080/00268970802018367.
[40] Larsen FH, Farnan I. Site Populations and Short Range Order in Aluminosilicates Investigated by ^{27}Al Solid-State NMR. J Phys Chem B 2004;108:9764–71. doi:10.1021/jp049603d.
[41] Charpentier T, Kroll P, Mauri F. First-Principles Nuclear Magnetic Resonance Structural Analysis of Vitreous Silica. J Phys Chem C 2009;113:7917–29. doi:10.1021/jp900297r.

[42] Scott DW, Wiley InterScience (Online service). Multivariate density estimation theory, practice, and visualization. New York: Wiley; 1992.
[43] Charpentier T, Fermon C, Virlet J. Efficient Time Propagation Technique for MAS NMR Simulation: Application to Quadrupolar Nuclei. J Magn Reson 1998;132:181–90. doi:10.1006/jmre.1998.1415.
[44] Levitt MH, EdéN M. Numerical simulation of periodic nuclear magnetic resonance problems: fast calculation of carousel averages. Mol Phys 1998;95:879–90. doi:10.1080/002689798166503.
[45] Hohwy M, Bildsøe H, Jakobsen HJ, Nielsen NC. Efficient Spectral Simulations in NMR of Rotating Solids. The γ-COMPUTE Algorithm. J Magn Reson 1999;136:6–14. doi:10.1006/jmre.1998.1593.
[46] Bak M, Rasmussen JT, Nielsen NC. SIMPSON: A General Simulation Program for Solid-State NMR Spectroscopy. J Magn Reson 2000;147:296–330. doi:10.1006/jmre.2000.2179.
[47] Edén M. Computer simulations in solid-state NMR. I. Spin dynamics theory. Concepts Magn Reson 2003;17A:117–54. doi:10.1002/cmr.a.10061.
[48] Edén M. Computer simulations in solid-state NMR. II. Implementations for static and rotating samples. Concepts Magn Reson 2003;18A:1–23. doi:10.1002/cmr.a.10064.
[49] Edén M. Computer simulations in solid-state NMR. III. Powder averaging. Concepts Magn Reson 2003;18A:24–55. doi:10.1002/cmr.a.10065.
[50] Alderman DW, Sherwood MH, Grant DM. Comparing, Modeling, and Assigning Chemical-Shift Tensors in the Cartesian, Irreducible Spherical, and Icosahedral Representations. J Magn Reson A 1993;101:188–97. doi:10.1006/jmra.1993.1029.
[51] Mehring M, Weberruss VA. Object-oriented magnetic resonance classes and objects, calculations and computations. San Diego, Calif.: Academic Press; 2001.
[52] McBrierty VJ. Nuclear magnetic resonance in solid polymers. Digitally printed 1st pbk. version. Cambridge ; New York: Cambridge University Press; 2006.
[53] Charpentier T, Ispas S, Profeta M, Mauri F, Pickard CJ. First-Principles Calculation of ^{17}O, ^{29}Si, and ^{23}Na NMR Spectra of Sodium Silicate Crystals and Glasses. J Phys Chem B 2004;108:4147–61. doi:10.1021/jp0367225.
[54] Haeberlen U. High resolution NMR in solids selective averaging. New York: Academic Press; 1976.
[55] Charpentier T, Fermon C, Virlet J. Numerical and theoretical analysis of multiquantum magic-angle spinning experiments. J Chem Phys 1998;109:3116. doi:10.1063/1.476903.

CHAPTER 3

^{29}Si NMR spectroscopy: silicon environment in silicate and aluminosilcate glasses

^{29}Si MAS investigations regarded four compositions: one silicate, CSN ($60SiO_2 \cdot 20Na_2O \cdot 20CaO$) and three aluminosilicate: CAS ($60SiO_2 \cdot 20Al_2O_3 \cdot 20CaO$), NAS ($78SiO_2 \cdot 11Al_2O_3 \cdot 11Na_2O$) and CASN ($60SiO_2 \cdot 10Al_2O_3 \cdot 10Na_2O \cdot 20CaO$).

It is worth noticing that NAS samples was enriched in Silicon-29 isotope, while the others contained ^{29}Si in natural abundance.

The results presented in this chapter were published on Geochimica et Cosmochimica Acta journal. [1]

3.1. Experiments of Silicon-29 NMR spectroscopy: information and challenges

Silicon-29 is the only stable NMR-active Si isotope and its natural abundance is 4.67%. Its nuclear spin is I = ½, meaning that it is not a quadrupolar nucleus. Its gyromagnetic ratio, γ = -8.465 MHz·T^{-1}, allows the collection of high-quality spectra at low-medium magnetic fields (< 10 T).

^{29}Si MAS NMR spectra were collected on a Bruker 300WB spectrometer at a magnetic field, **B**, of 7.02 T and a Larmor frequency $\omega_L = \gamma \cdot \mathbf{B}$ = 59.4 MHz. The sample was spun in a 4mm (outer diameter) MAS NMR probe at a spinning rate of 12.5 kHz. A CPMG pulse sequence [2], with ~16-32 echoes, was employed with a recycle delay of 200 s and typically 128-256 scans.

The experimental-computational approach allowed to interpret the variability of Silicon-29 NMR parameters in terms of chemical and topological disorder of its surroundings. This last knowledge is valuable for the exploitation of the '*structural NMR inversion*' approach, which allows transformation of NMR data into a distribution of structural parameters.

3.2. Comparison between experimental and theoretical ^{29}Si MAS spectra

The theoretical and experimental ^{29}Si MAS NMR spectra are compared in **Figure 3.1**. Whereas the experimental peaks show almost Gaussian shapes, the theoretical ones exhibit more accentuated asymmetries, which might be due to the limited number of silicon atoms that we have been forced to use. In fact, *ab initio* calculations have huge computational costs and, in order to keep acceptable calculation time, it is necessary to perform DFT calculations on systems which are not more extended than a few hundreds of atoms. Nonetheless, a good agreement in the peak shapes is observed. The MD-generated structures are mainly characterized by four-coordinated silicon. The very small amount of fivefold coordinated silicon (1 site in CASN at δ_{iso}= -134 ppm and 1 site in CSN glasses at δ_{iso}= -133.2 ppm) may be ascribed to the excessively high pressure and rapid cooling rate experienced by the atoms in the simulation boxes during the MD generation of glasses at a constant volume. Anyway, exiguous populations of fivefold Si atoms (about 0.05%) were characterized by Stebbins et al. in silica-based glasses cooled both at high and 1 bar pressure.[3]

The theoretical populations of four coordinated Si(Q^n) species present in the simulated structures are reported in **Table 3.1**. NAS glass exhibits the more polymerized network, where almost all (98.3 %) silicon atoms belongs to Q^4 units, whereas the remaining 1.7 % are in Q^3 units. In the CAS glass Si atoms are organized in Q^4, Q^3 and Q^2 units in the respective percentages of 95.7%, 2.1% and 1.4%. Although NAS and CAS glasses have tectosilicate compositions (i.e.: $[M^{z+}_{(x/z)}O_x]/[Al_2O_3] = 1$), their Al atoms are not fully charge compensated by modifier cations and a small fraction of tri-cluster Oxygen atoms (TBOs) is present. This results in a not completely polymerized network.

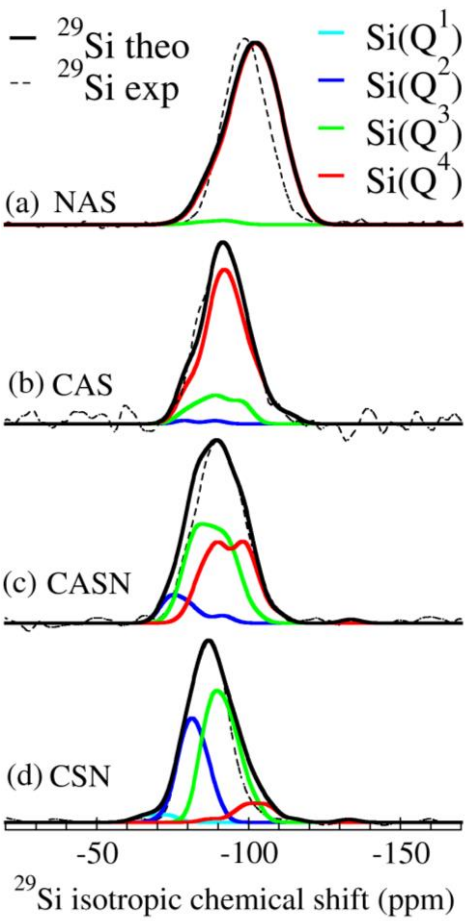

Figure 3.1. Comparison between experimental (black dashed lines) and theoretical (black solid lines) ^{29}Si MAS NMR spectra (normalized to the same maximum height) of NAS (a), CAS (b) and CASN (c) and CSN (d) glasses. Simulated individual contribution of Q^n species to the total theoretical spectra are reported in colored solid lines.

Table 3.1. Theoretical and experimental ^{29}Si NMR parameters in SiO_4 units for NAS, CAS, CASN and CSN glasses. (*) δ_{ca}^{exp} is the center of gravity of the experimental ^{29}Si spectrum and is here assumed to be the experimental counterpart of δ_{diso}^{exp}.

Q^n	*connectivity speciation*	Pop %		δ_{iso}(ppm)		Si(Q^n)-O-T
		MD	Exp.	Th.	δ_{cg}^{exp}(*)	Th.
				NAS		
Si		100.0	100.0	-101.1(8.0)	-98.7	142.5(6.9)
	4BO	97.2		-101.4 (7.9)		
Q^4	*3BO:1TBO*	1.1	89.9	-92.9 (10)	-99.6 (6.6)	142.8(6.7)
Q^3	*3BO:1NBO*	1.7	10.1	-89.8 (5.4)	-90.9 (5.6)	130.7(5.0)
				CAS		
Si		100.0	100.0	-92.5(7.6)	-91.9	137.1(7.6)
	4BO	71.6		-93.8 (7.5)		
	3BO:1TBO	9.2	93.6%	-89.2 (7.5)	-92.2 (8.0)	137.7(12.7)
Q^4	*2BO:2TBO*	14.9		-81.3		
Q^3	*3BO:1NBO*	0.7	4.9%	-90.4 (6.7)	-89.8 (3.9)	135.3(13.2)
	2NBO:1TBO:1NBO	1.4		-84.2 (9.8)		
Q^2	*2BO:2NBO*	1.4	1.5%	-84.1 (7.1)	-83.1 (1.0	143.2(13.6)
				CASN		
Si		100.0	100.0	-89.9(8.3)	-91.2	137.0(6.9)
Q^4	*4BO*	42.0	44.7%	-93.9 (7.2)	-96.6 (6.4)	137.7(12.7)
Q^3	*3BO:1NBO*	47.3	44.7%	-88.0 (6.4)	-87.1 (5.9)	137.3(13.5)
Q^2	*2BO:2NBO*	10.0	53.7%	-79.1 (6.4)	-82.7 (1.7)	132.8(11.7)
				CSN		
Si		100.0	100.0	-88.7(9.0)	-87.1	138.8(6.4)
Q^4	*4BO*	8.6	4.0%	-102.2 (6.8)	-102.2 (5.9)	141.5(13.0)
Q^3	*3BO:1NBO*	52.5	46.0%	-91.5 (4.9)	-90.4 (4.6)	138.6(12.1)
Q^2	*2BO:2NBO*	35.2	50.0%	-82.0 (3.9)	-77.3 (5.0)	138.5(11.9)
Q^1	*1BO:3NBO*	3.1	0.0%	-69.7 (4.7)	---	128.8(3.2)

Table 3.1 also reports populations and NMR parameter details of SiO_4 units speciation as a function of BO, NBO and TBO connectivity. It emerges how TBO connectivity shields tetrahedral silicon, in a way that Si atoms bonded to TBO are not detectable on a MAS spectra. This predicted structural arrangement is in agreement with experimental evidences that deny the validity of Compensated Continuous Random Network for tectosilicate glasses[4,5]. However, in one of our previous works we recognized that the adopted MD-protocols overestimates the presence of TBOs.[6] Networks of CASN and CSN are less polymerized: in the former, the majority of silicon atoms are present as Q^4 (42.0%) and Q^3 (47.3%) species, and Q^2 units constitute the remaining 10%, while in the latter also Q^1 species are present (3.1 %) in addition to Q^4 (8.6%), Q^3 (52.5%) and Q^2 (35.2%) ones.

The computed NMR parameters (**Table 3.1)** have been used to fit the experimental spectra and to quantify Si(Q^n) species populations in the samples. For CAS and CASN glasses, MD and fitted Q^n populations are in good agreement, while CSN and NAS populations differ up to 14.8 %, which might be considered an acceptable value in the case of ^{29}Si MAS spectra. Theoretical and fitted δ_{iso} ranges from about -100 ppm to -70 ppm, consistently with previous experimental observations on glasses and crystals [7–9] and increases from Q^4 to Q^1 with an increment between 3 and 10 ppm.

Another important structural parameter is the average Si-O-T (T = Si or Al) bond angle of the Q^n species, reported in **Table 3.1**. A decrease of 0.1° to 9.7° in the <Si-O-T> angle is observed in all structural models, whether the n index of the Q^n species increases of 1 unit, i.e.: the number of NBOs connected to silicon increases. The Q^2 structural unit of the CAS glass presents an exception to this rule: the <Si-O-T> angle increases from 135.3°

for Q^3 to 143.2° for Q^2. In this case, the poor representativeness of the Q^2 population (1.4 % of total Si atoms) might be invoked. Also Q^3 species in NAS glass have a very scant population (1.6 %) and are not considered for this discussion. A general explanation for this behavior is found in the number of NBOs on a Q^n unit; the NBOs species attract in their surrounding modifier cations (Na^+, Ca^{2+}) which induce a compression of the inter-tetrahedral angles. The compression is proportional to the field strength of the cation modifier[10]. Summarizing, moving from Q^4 to Q^1 both an increase in isotropic chemical shift values and a decrease in <Si-O-T> angles is observed. This behavior is coherent with very well-known correlations between <Si-O-Si> angle and ^{29}Si δ_{iso}, found in many silicate and aluminosilicate glasses.[11–14]

3.3. Silicon second coordination sphere: framework disorder

The quantification of Q^n species in silicate, phosphosilicate or aluminosilicate glass samples have often been obtained, as in this work (**Table 3.1**), by assuming that each Q^n species contributes with a Gaussian distribution to the total spectra of ^{29}Si [8,15,16]. However, this assumption was debated [17] and a new approach that uses 2D techniques was developed [18–20]. In fact, because of the deshielding effect of Al on Si that is discussed further below, a single Gaussian function cannot reproduce the band shape of a Si(Q^n) species (see **Figure 3.1**). The interpretation of ^{29}Si NMR spectrum in terms of Si(Q^4)[*m*Al] species, where $m = 0 \div 4$ is the number of Al bonded to Si through a BO, has already been elaborated in the past after experimental studies on crystalline aluminosilicate [21], and then extended to geopolymeric [22] and glassy phases [23–25]. Recently, Hiet et al. [24] succeeded in quantifying the

network chemical disorder of a CAS-type glass ($25\%CaO{\cdot}25\%Al_2O_8{\cdot}50\%SiO_2$) with the help of very promising advanced NMR techniques. The population of the various Si(Q^4)[*m*Al] species they determined are nevertheless different from those predicted by our structural model for CAS, as listed in **Table 3.2**. However, their δ_{iso} values are within 6 ppm, which is the standard deviation associated to our theoretical values.

Our MD-GIPAW data offer the opportunity to theoretically investigate network former intermixing in glasses and to provide a glass-tailored investigation on NMR parameters, also for Q^3 structural units. Q^2 and Q^1 species are omitted from the investigation because of their small populations in the structural models. **Figure 3.2** shows computed contributions of Si(Q^n)[*m*Al] to Q^n species theoretical spectra for NAS, CAS and CASN glasses. As expected, the most populated sites show signals whose shape is more similar to that of a Gaussian. A trivial justification for the deviation from the Gaussian-shapes of the computed contribution with respect to the one reputedly obtained by a real sample is the small amount of species considered in the calculation. For example, Si(Q^4)[2Al] species in CAS glass counts barely 42 atoms, and the most populated species among the three aluminosilicate glasses, Si(Q^4)[1Al] in NAS glass, counts 88 atoms.

Focusing on the more populated Si(Q^n)[*m*Al] species (at least 5% of total Si atoms), the NMR parameters listed in **Table 3.2**, δ_{iso} and chemical shift anisotropy expressed in absolute values, $|\Delta_{CS}|$, show interesting trends.

They both increases with the number of aluminium cations in the silicon second coordination sphere. The extent of increase of δ_{iso} varies from + 2.9 to + 6.6 ppm per aluminium, and from +1.3 to + 8.8 ppm in the case of $|\Delta_{CS}|$.

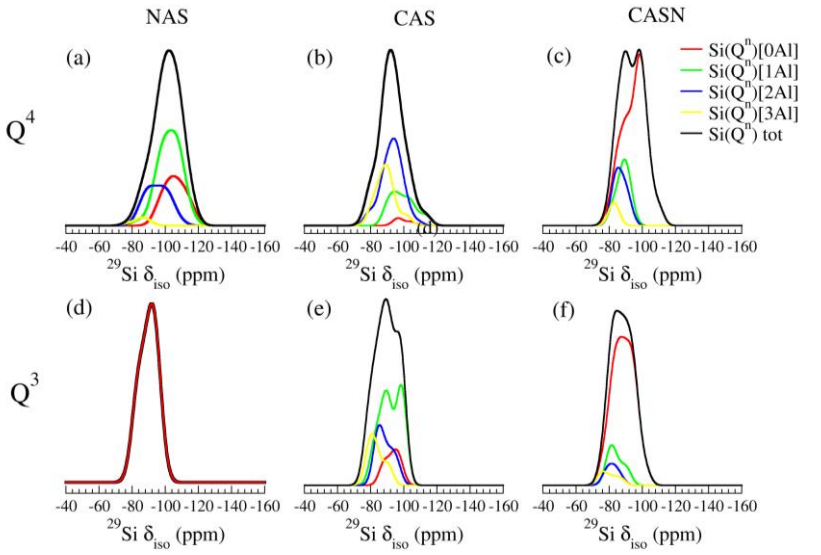

Figure 3.2. Computed contribution of Si(Q^n)[*m*Al] (with *n*=3,4; *m*=0÷3) to Q^n species theoretical spectra for all aluminosilicate glasses: NAS (a and d) CAS (b and e) and CASN (c and f); Q^2 species are not considered because of non-representative populations.

The results obtained are in agreement with empirical assumptions proposed in previous experimental works [21,23,25], where ^{29}Si δ_{iso} increases almost constantly of +5 ppm per Al added to Si coordination sphere. Our results also reveal a certain sensibility of $|\Delta_{CS}|$ to network chemical disorder and give a further instrument for accurately quantifying network chemical disorder. Indeed, a deconvolution of NMR spectra using specific constraints, like those provided in **Table 3.2**, will help to quantify these species, which actually represent network disorder.

This has been done for the NAS glass. Actually its experimental spectra was characterized by a very high S/N ratio, and the relatively high populations of Si(Q^n)[*m*Al] species in MD-derived models provide reliable theoretical constraints.

Table 3.2. NMR parameters of Si(Q^n)[mAl] species, where n = 3, 4, surrounded by m (m = 0 ÷ 4) aluminium atoms in the second coordination sphere; standard deviations in parenthesis. Si bonded to TBO (2 sites in NAS, 15 sites in CAS) and fivefold coordinated Si (1 site in CASN) have been neglected from the analysis.

m	Q^4 Pop%[(a)]	Q^4 $\bar{\delta}_{iso}$(ppm)	Q^4 $\lvert\Delta_{CS}\rvert$(ppm)	Q^3 Pop%	Q^3 $\bar{\delta}_{iso}$(ppm)	Q^3 $\lvert\Delta_{CS}\rvert$ (ppm)
			NAS			
0	23.5	-105.8(6.2)	14.9(8.0)	1.6	-89.8(5.4)	86.3(11.2)
1	48.1	-102.7(6.6)	36.0(10.0)	0.0	---	---
2	22.4	-95.3(6.8)	40.0(10.4)	0.0	---	---
3	2.2	-84.9(4.5)	35.5(6.2)	0.0	---	---
4	0.0	---	---	0.0	---	---
			CAS			
0	2.1	-99.3(4.6)	18.5(2.1)	2.1	-93.1(4.6)	66.9(5.7)
1	17.7	-99.6(7.6)	30.8(10.4)	7.8	-92.4(6.7)	66.6(16.1)
2	33.3	-93.2(6.5)	25.0(14.7)	3.5	-88.7(5.0)	58.2(15.5)
3	17.7	-89.1(4.8)	28.5(11.3)	1.4	-79.9(1.3)	31.2(3.4)
4	0.8	79.2	22.4	0.0	---	---
			CASN			
0	5.3	-100,4(7.0)	19.4(5.8)	13.3	-93.3(5.6)	64.2(15.8)
1	15.3	-95.9(6.9)	27.8(9.9)	22.0	-88.3(5.1)	58.6(15.3)
2	18.0	-92.0(5.7)	38.5(9.8)	10.0	-82.7(2.6)	52.7(14.6)
3	3.3	-84.7(3.4)	28.9(12.8)	2.0	-76.9(1.8)	43.6(23.4)
4	0.0	---	---	0.0	---	---

Table 3.3 reports the relative populations and isotropic chemical shifts extracted from the fitting of ^{29}Si MAS spectra. To fit Silicon-29 MAS experimental spectra (**Fig.1.a**), the theoretical δ_{iso} values for Si(Q^3)[2Al] and Si(Q^4)[0/1/2/3Al] (**Table 3.2**) were used as constraints. In this case, the error is 0.27% and is lower with respect to that (0.37%) obtained by fitting the spectra considering Q^4 and Q^3 without decomposing the Q^n sites in the different Si(Q^n)[*m*Al] species.

Table 3.3. Quantification of chemical disorder of NAS network: fitting experimental spectra with Si(Q^n)[mAl] (n = 3,4; m = 0÷3) species constraints.

Species	Pop %, $_{EXP}$[(a)]	$\overline{\delta_{iso,\ EXP}}$[(a)] (ppm)
Si	100.0	103.0(5.9)
Si(Q^4)[0Al]	68.8	-105.6(5.9)
Si(Q^4)[1Al]	21.3	-102.8(5.9)
Si(Q^4)[2Al]	0.0	-95.4(5.9)
Si(Q^4)[3Al]	9.9	-85.8(5.9)
Si(Q^3)[0Al]	0.0	-89.7(5.0)

[(a)] Error associated to fitting procedure: 0.27 %.

The obtained isotropic chemical shifts, $\overline{\delta_{iso,\ EXP}}$, are in excellent agreement with those computed at the MD-GIPAW level reported in **Table 3.2**, whereas the very high percentage (Pop %,$_{EXP}$) of Si(Q^4)[0Al] species (68.8%) and the low amount of Si(Q^4)[2Al] and Si(Q^4)[3Al] demonstrate that the MD structural models overestimates the clusterization of Aluminium around silicon. Finally, the sum of Si(Q^4)[*m*Al] experimental populations give a 100% Q^4 speciation and a 0% Q^3 speciation of silicon; this quantification is much more reasonable than the populations (**Table 3.2**) obtained by fitting the spectra with only the 2 constraints of theoretical ^{29}Si(Q^3) and Si(Q^4) δ_{iso}.

Another interesting point on network cation intermixing is to verify whether there is a particular Si(Q^n) unit that exhibits a preference to build Si-O-Al bridges. To shed light on this, for each Q^n species, we counted the number of Si(Q^n)-O-Al bridges. The number has been divided for the total number of Si(Q^n)-O-T bridges and then normalized with respect to CAS Al/Si ratio, i.e.: multiplied for the $(Al/Si)_{glass}/(Al/Si)_{CAS}$ ratio. The results of the normalized Si(Q^n)-O-T bridges are reported in **Table 3.4**. Here, a preference for Al atoms to form Si-O-Al bridges with Si(Q^4) species is observed.

Table 3.4. Ratio of Si(Q^n)-O-Al (n = 2, 3, 4) bridges respect to total Si(Q^n)-O-T bridges and normalized Al/Si ratio in CAS glass.

$\frac{Si(Q^n)-O-Al}{\mathrm{Si(Q^n)-O-T}} \cdot \frac{Al/Si_{glass}}{Al/Si_{CAS}}$	NAS	CAS	CASN
Si(Q^2)	---(*)	---	0.449
Si(Q^3)	0.000	0.486	0.632
Si(Q^4)	0. 594	0.701	0.683

(*) The respective Si(Q^n) species is not present in the structural model of the considered glass (NAS) or its population is not significant, i.e.: less than 5% of total Si atoms (CAS).

3.4. Silicon second coordination sphere: non-framework disorder

Further precious information about the systems under study can be obtained analyzing the presence of calcium and/or sodium in the second coordination sphere of Si, and then evaluating their effect on ^{29}Si NMR parameters. From the MD-derived models, the Si coordination number with respect to each modifier, M that is Ca or Na (CN_{Si}^{M}), was calculated within a cut-off of 5 Å. The overall preference for Ca or Na coordination was gathered from the ratio of CN_{Si}^{Ca} and CN_{Si}^{Na}, normalized with respect to the Ca/Na ratio in the models, $\mathrm{R_{Si}^{Ca/Na}}$:

$$\mathrm{R_{Si}^{Ca/Na}} = \frac{CN_{Si}^{Ca}}{CN_{Si}^{Na}} \cdot \frac{n°Na}{n°Ca} \qquad \text{(Eq. 3.1)}$$

Values of the aforementioned quantities are reported in **Table 3.5**. Here, we see that calcium and sodium concentration around silicon varies with Q^n speciation: CN_{Si}^{Ca} decreases by ~1.2-1.3 units in CAS and CASN and by ~1.0 in CSN when increasing the number of BO in the ($SiO_{4/2}$) unit. Whereas CN_{Si}^{Na} decrease of ~0.9 units in CASN glass and of ~1.8 units in NAS glass. On the

other hand CN_{Si}^{Na} in CSN glass has an almost constant value of about 3.8 – 4.

Table 3.5. Average coordination number, CN_{Si}^{M}, of silicon atoms and Q^n species, referred to modifier cations, M, in the second coordination sphere (M = Ca and/or Na), $R_{Si}^{Ca/Na}$.

	CN_{Si}^{Ca}			CN_{Si}^{Na}			$R_{Si}^{Ca/Na}$	
Glass	CAS	CASN	CSN	NAS	CASN	CSN	CASN	CSN
Si total	1.77	1.93	1.90	1.61	1.91	3.92	1.01	0.97
Si(Q^4)	1.54	1.08	0.46	1.58	1.79	4.07	0.60	0.23
Si(Q^3)	2.71	2.28	1.51	3.38	1.97	3.82	1.16	0.79
Si(Q^2)	4.00	3.40	2.56	---	2.06	3.98	1.65	1.29
Si(Q^1)	---(*)	---	3.80	---	---	4.40	---	1.73

(*)The respective Si(Q^n) species is not present in the structural model of the considered glass.

In both CASN and CSN glasses, total silicon exhibits no preference for Ca or Na, as $R_{Si}^{Ca/Na} \sim 1$, while an in-depth examination on Q^n species reveals that Ca cations are mainly allocated in Q^1 and Q^2 surroundings, and Na is more localized around Q^3 and Q^4 units. These outcomes can be explained by considering that Ca, whose high field strength is higher than that of Na, prefers "electron-rich" environments, while Na lies close to most polymerized region of the network.

The effect of the presence of modifier cations (Ca and/or Na) around silicon atoms on ^{29}Si NMR parameters has been investigated for all glasses. The second coordination shell of silicon expressed in terms of modifiers defines the Si[*k*M] and Si(Q^n)[*k*M] species, where *k* is the total amount of modifier cations (n°Ca + n°Na) and M is indistinguishably Ca and/or Na. Contrary to chemical shift anisotropy, Δ_{CSA}, and asymmetry parameter, η_{CSA}, the computed isotropic chemical shift, δ_{iso}, parameter shows interesting trends

that are reported in **Figure 3.3** for total Si and its more populated (> 5.0 %) Si(Q^n) species.

In aluminosilicate glasses NAS (**Fig. 3.3.a**), CAS (**Fig. 3.3.b**) and CASN (**Fig. 3.3.c**) it is possible to observe the deshielding effect of calcium and/or sodium on silicon-29 nuclei for total silicon and Si(Q^n) species [9]. Nevertheless, the Q^n species in the CSN glass do not follow the trend (**Fig. 3.3.d**); therefore the deshielding effect on total silicon is only apparent. It is actually ascribable to the fact that, although each Q^n(*k*M) unit does not exhibit a dependence on *k*, they differently populate Si(Q^n) site. The deshielding effect of Ca and Na modifier is then an "apparent effect", related to the second coordination shell intended in terms of aluminium, rather than in terms of modifier cations.

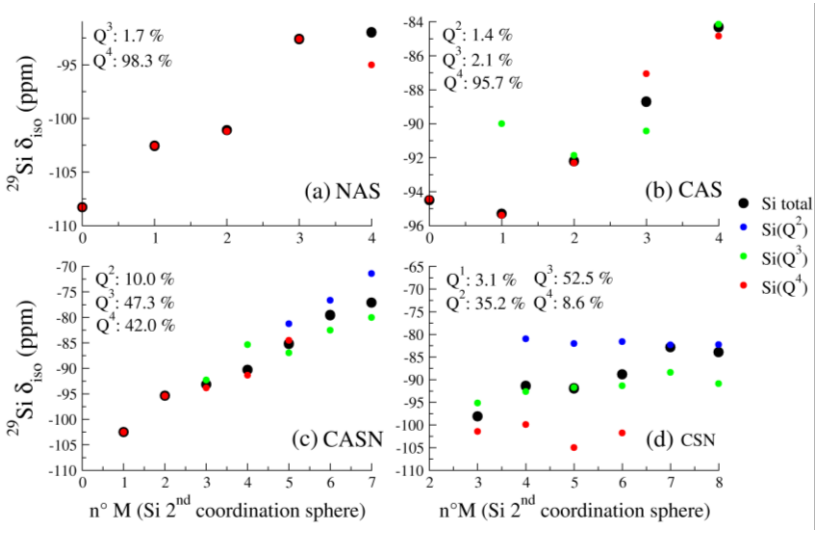

Figure 3.3. Correlations between the isotropic chemical shift, δ_{iso}, and the amount of modifier cations, n°M = (n°Ca + n°Na), in the silicon second coordination sphere for the glasses studied (black circles). The correlations obtained by means of the contribution of modifier cations, in the second coordination sphere of each Si(Q^n) species are also reported (colored dots). The population of Q^n species in the MD-derived structural models is reported in each panel.

3.5. Relationships between ^{29}Si δ_{iso} and Si–O–T angles.

Accurate relationships between NMR parameters and structural features are extremely useful for the interpretation of experimental data, as they make a reverse approach possible[13,14,26–28]. In this way, structural features of a glass sample could, in principle, be directly obtained from the experimental data distribution. With the aim to quantify network topological disorder, scientists' attention has been focused on the correlation between ^{29}Si δ_{iso} and Si-O-T intertetrahedral angles [13,21,26,29]. **Figure 3.4** display the plot of ^{29}Si δ_{iso} vs <Si-O-T>. At first glance, the goodness of linear correlations seems to vary depending on glass composition. But when Si connectivity to different oxygen species (BOs, NBOs, TBOs), i.e. Q^n species, is taken into account, then reasonable correlation coefficients can be found. More in detail, slope and intercept do not depend on chemical composition of the glasses, but on oxygen connectivity only. It is worth noticing that those glasses containing calcium, i.e.: CAS, CASN and CSN, show the poorest correlations, as previously observed experimentally [19] and theoretically [15] on $CaO\text{-}SiO_2$ phases. As stated in paragraph **3.3**, Ca^{2+} in mixed Ca-Na glasses, like CASN and CSN, is not uniformly allocated around the different $Si(Q^n)$ species, but its concentration is maximum around $Si(Q^2)$ and minimum around $Si(Q^4)$. It is then reasonable to expect that $^{29}Si(Q^n)$ δ_{iso} differently correlates with <Si-O-T> depending on $Si(Q^n)$.

Coefficients of determination (R^2) reported in **Figure 3.4** reveal a decrease in the linear correlations with *n*: from 0.72, for $Si(Q^4)$, to 0.60, for $Si(Q^3)$, in CASN glass (**Fig. 3.4.b**) and from 0.96, for $Si(Q^4)$, to 0.52, for $Si(Q^2)$, in CSN glass (**Fig. 3.4.c**). Analogous behavior was also observed by Pedone et al. in

bioglasses [15]. It is also worth noticing that coefficients of determination in CASN glass are lower than those in CSN glass, suggesting that aluminium, analogously to calcium, may contribute to weaken the correlation between ^{29}Si δ_{iso} and <Si–O–T> inter-tetrahedral angles.

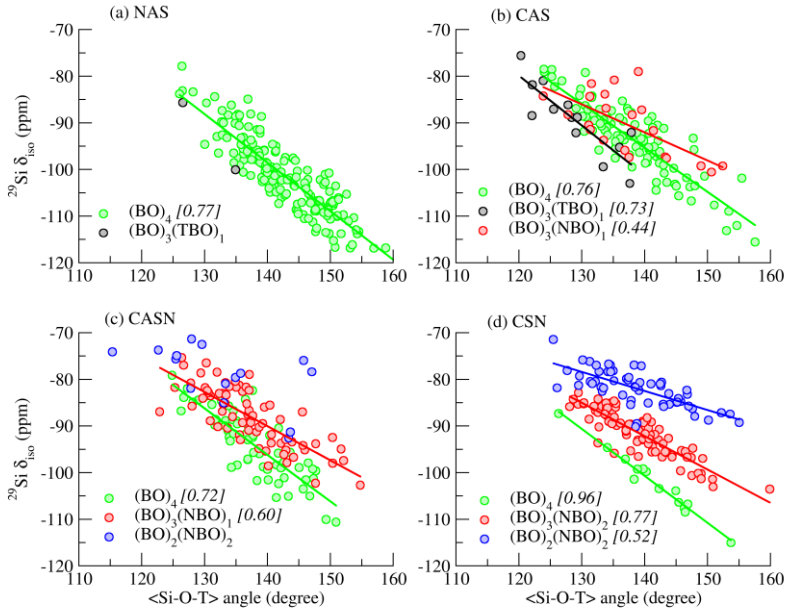

Figure 3.4. Plot of ^{29}Si δ_{iso} vs <Si-O-T> reported for different connectivity environments of Si in NAS, CAS, CASN and CSN. $Si(BO)_4$ are green dots, $Si(BO)_3(NBO)_1$ are red dots, $Si(BO)_2(NBO)_2$ are blue dots and $Si(BO)_3(TBO)_1$ are black circles. Linear regression fitting lines are also reported with coherent colors and coefficients of determination of linear regression, R^2, are listed in brackets.

3.6. Final remarks

In **paragraph 3.2** we showed the agreement between computed and experimental ^{29}Si parameters and MAS spectra, thus demonstrating the

soundness of our structural models and, in turn, the reliability of the computational method.

^{29}Si δ_{iso} values are affected by the nature of Si second coordination sphere expressed in terms of former cations, but not in terms of the modifier cations Ca^{2+} and Na^{+}. In general, aluminium atoms in Si second coordination sphere deshield ^{29}Si nuclei. This effect was taken into account when fitting NMR spectra with the aim to quantify network chemical disorder and Si(Q^n) species. Indeed, we fitted ^{29}Si MAS spectra of NAS spectra by using theoretical δ_{iso} range values obtained from sufficiently populated Si(Q^n)[*m*Al] species. We obtained a lower fitting error with respect to the fitting with Si(Q^n) constraints. Beyond a lower fitting error, Si(Q^n) populations intended as the sum of Si(Q^n)[*m*Al] having the same *n*, presented values more coherent with network polymerization expected for NAS composition.

Simple and effective correlations between ^{29}Si δ_{iso} and inter-tetrahedral angles can be found for these multicomponent systems only if the connectivity of Si to different oxygen species (BOs, NBOs, TBOs) is properly taken into account. Nonetheless, it is recognized that the presence of calcium cations tends to critically compromise the correlations. This effect is evident for different compositions with different percentages of CaO, but also for Si(Q^n) species surrounded by different numbers of Ca^{2+}.

Then, in order to obtain very accurate correlations between <Si-O-T> angles and ^{29}Si δ_{iso}, it would be appropriate to elaborate multivariate correlations that include, beyond the inter-tetrahedral angle, structural features concerning the nature of Si second coordination shell in terms of Ca and Al.

Bibliography

[1] Gambuzzi E, Pedone A, Menziani MC, Angeli F, Caurant D, Charpentier T. Probing silicon and aluminium chemical environments in silicate and aluminosilicate glasses by solid state NMR spectroscopy and accurate first-principles calculations. Geochim Cosmochim Acta 2014;125:170–85. doi:10.1016/j.gca.2013.10.025.

[2] Larsen FH, Farnan I. 29Si and 17O (Q)CPMG-MAS solid-state NMR experiments as an optimum approach for half-integer nuclei having long T1 relaxation times. Chem Phys Lett 2002;357:403–8. doi:10.1016/S0009-2614(02)00520-1.

[3] Stebbins JF, Farnan I, Xue X. The structure and dynamics of alkali silicate liquids: A view from NMR spectroscopy. Chem Geol 1992;96:371–85. doi:10.1016/0009-2541(92)90066-E.

[4] Stebbins JF, Xu Z. NMR evidence for excess non-bridging oxygen in an aluminosilicate glass. Nature 1997;390:60–2.

[5] Toplis MJ, Dingwell, Donald B., Hess K-W, Lenci T. Viscosity, fragility, and configurational entropy of melts along the join SiO2-NaAlSiO4. Am Min 1997;82:979–90.

[6] Pedone A, Gambuzzi E, Malavasi G, Menziani MC. First-principles simulations of the 27Al and 17O solid-state NMR spectra of the CaAl2Si3O10 glass. Theor Chem Acc 2012;131. doi:10.1007/s00214-012-1147-5.

[7] Murdoch JB, Stebbins JF, Carmichael ISE. High-resolution 29Si NMR study of silicate and aluminosilicate glasses: the effect of network-modifying cations. Am Min 1985;70:332–43.

[8] Maekawa H, Maekawa T, Kawamura K, Yokokawa T. The structural groups of alkali silicate glasses determined from 29Si MAS-NMR. J Non-Cryst Solids 1991;127:53–64. doi:10.1016/0022-3093(91)90400-Z.

[9] Jones A., Winter R, Greaves G., Smith I. MAS NMR study of soda-lime–silicate glasses with variable degree of polymerisation. J Non-Cryst Solids 2001;293-295:87–92. doi:10.1016/S0022-3093(01)00656-1.

[10] Cormier L, Ghaleb D, Neuville DR, Delaye J-M, Calas G. Chemical dependence of network topology of calcium aluminosilicate glasses: a computer simulation study. J Non-Cryst Solids 2003;332:255–70. doi:10.1016/j.jnoncrysol.2003.09.012.

[11] Lippmaa E, Samoson A, Magi M. High-resolution aluminum-27 NMR of aluminosilicates. J Am Chem Soc 1986;108:1730–5. doi:10.1021/ja00268a002.

[12] Phillips BL, Kirkpatrick RJ. Short-range Si-Al order in leucite and analcime: determination of the configurational entropy from 27Al and variable-temperature 29Si NMR spectroscopy of leucite, its Cs- and Rb-exchanged derivatives, and analcime. Am Min 1994;79:1025–31.

[13] Mauri F, Pasquarello A, Pfrommer B, Yoon Y-G, Louie S. Si-O-Si bond-angle distribution in vitreous silica from first-principles 29Si NMR analysis. Phys Rev B 2000;62:R4786–9. doi:10.1103/PhysRevB.62.R4786.

[14] Angeli F, Villain O, Schuller S, Ispas S, Charpentier T. Insight into sodium silicate glass structural organization by multinuclear NMR combined with first-principles calculations. Geochim Cosmochim Acta 2011;75:2453–69. doi:10.1016/j.gca.2011.02.003.

[15] Pedone A, Charpentier T, Malavasi G, Menziani MC. New Insights into the Atomic Structure of 45S5 Bioglass by Means of Solid-State NMR Spectroscopy and Accurate First-Principles Simulations. Chem Mater 2010;22:5644–52. doi:10.1021/cm102089c.

[16] Merzbacher CI, Sherriff BL, Hartman JS, White WB. A high-resolution 29Si and 27Al NMR study of alkaline earth aluminosilicate glasses. J Non-Cryst Solids 1990;124:194–206. doi:10.1016/0022-3093(90)90263-L.
[17] Mahler J, Sebald A. Deconvolution of 29Si magic-angle spinning nuclear magnetic resonance spectra of silicate glasses revisited — some critical comments. Solid State Nucl Magn Reson 1995;5:63–78. doi:10.1016/0926-2040(95)00027-N.
[18] Zhang P, Dunlap C, Florian P, Grandinetti PJ, Farnan I, Stebbins JF. Silicon site distributions in an alkali silicate glass derived by two-dimensional 29Si nuclear magnetic resonance. J Non-Cryst Solids 1996;204:294–300. doi:10.1016/S0022-3093(96)00601-1.
[19] Florian P, Fayon F, Massiot D. ^{2}J Si−O−Si Scalar Spin−Spin Coupling in the Solid State: Crystalline and Glassy Wollastonite $CaSiO_3$. J Phys Chem C 2009;113:2562–72. doi:10.1021/jp8078309.
[20] Davis DC, Kaseman SM, Parvani SM, Sanders KJ, Grandinetti PJ, Massiot D, et al. Q(n) species distribution in K2O·2SiO2 glass by 29Si magic angle flipping NMR. J Phys Chem A 2010;114:5503–8.
[21] Engelhardt G. High-resolution solid-state NMR of silicates and zeolites. Chichester [West Sussex] ; New York: Wiley; 1987.
[22] Duxson P, Provis JL, Lukey GC, Separovic F, van Deventer JSJ. ^{29} Si NMR Study of Structural Ordering in Aluminosilicate Geopolymer Gels. Langmuir 2005;21:3028–36. doi:10.1021/la047336x.
[23] Lee SK, Stebbins JF. The degree of aluminium avoindance in aluminosilicate glasses. Am Min 1999;84:937–45.
[24] Hiet J, Deschamps M, Pellerin N, Fayon F, Massiot D. Probing chemical disorder in glasses using silicon-29 NMR spectral editing. Phys Chem Chem Phys 2009;11:6935. doi:10.1039/b906399d.
[25] Moesgaard M, Keding R, Skibsted J, Yue Y. Evidence of Intermediate-Range Order Heterogeneity in Calcium Aluminosilicate Glasses. Chem Mater 2010;22:4471–83. doi:10.1021/cm1011795.
[26] Charpentier T, Kroll P, Mauri F. First-Principles Nuclear Magnetic Resonance Structural Analysis of Vitreous Silica. J Phys Chem C 2009;113:7917–29. doi:10.1021/jp900297r.
[27] Clark T, Grandinetti P, Florian P, Stebbins J. Correlated structural distributions in silica glass. Phys Rev B 2004;70. doi:10.1103/PhysRevB.70.064202.
[28] Soleilhavoup A, Delaye J-M, Angeli F, Caurant D, Charpentier T. Contribution of first-principles calculations to multinuclear NMR analysis of borosilicate glasses. Magn Reson Chem 2010;48:S159–70. doi:10.1002/mrc.2673.
[29] MacKenzie KJD, Smith ME. Multinuclear Solid-State Nuclear Magnetic Resonance of Inorganic Materials. Burlington: Elsevier; 2002.

CHAPTER 4

^{27}Al NMR spectroscopy: aluminium environment in aluminosilicate glasses

^{27}Al MAS and MQMAS investigations were carried out on three compositions: CAS ($60SiO_2 \cdot 20Al_2O_3 \cdot 20CaO$), NAS ($78SiO_2 \cdot 11Al_2O_3 \cdot 11Na_2O$) and CASN ($60SiO_2 \cdot 10Al_2O_3 \cdot 10Na_2O \cdot 20CaO$).

Experimental ^{27}Al spectra of CAS and CASN glasses were taken from the literature, in a work dated 2007 [1], while NAS glass was synthesized and characterized on purpose for the Ph. D. research activity by Daniel Caurant (see **Paragraph 1.7**) Experimental details about its synthesis are reported in reference [2], while NMR data acquisition for NAS glass are reported below.

All the topics presented in this chapter were published on two international journals. [2,3]

4.1. Aluminium-27 NMR spectroscopy: experimental details and challenges

Aluminium-27 is the only stable isotope of Al element and is also an NMR-active quadrupolar nucleus, having nuclear spin I = 5/2. Its very high natural abundance (> 99.9 %) and its relatively low gyromagnetic ratio, γ = 11.103 $MHz \cdot T^{-1}$, allow to collect high-quality data (i.e.: high signal/noise ratio) at easily achievable experimental conditions. For instance, no isotopic enrichment of samples is needed and medium intensity applied magnetic field are sufficient.

In the present work, ^{27}Al MAS spectra of NAS glass were collected at the Larmor frequency $\omega_L = \gamma \cdot \mathbf{B}$ = 103.4 MHz on a Bruker Avance II 500WB spectrometer operating at a magnetic field, **B**, of 11.72 T. Sample was spun in a 4 mm (outer diameter) zirconia rotors at a frequency of 12.5 kHz.

The sensitivity of ^{27}Al NMR parameters to Al chemical and structural environment has been exploited to shed light on (i) Al-O connectivity, (ii) the extent of network chemical disorder and (ii) the effect of non-framework cations on ^{27}Al NMR parameters.

4.2. Comparison of experimental and theoretical data

Figure 4.1 reports theoretical and experimental ^{27}Al MAS NMR spectra of CAS, NAS and CASN glasses. The peak maximum at about 60 ppm of the experimental spectra, typical of four-coordinated aluminium atoms, are very well reproduced by our DFT calculations. In fact, all Al atoms present in our structural models are in Al(Q^4) tetrahedral units, except for CAS models which contain 5.32 % of five-fold Al (^{V}Al) and 2.66 % of

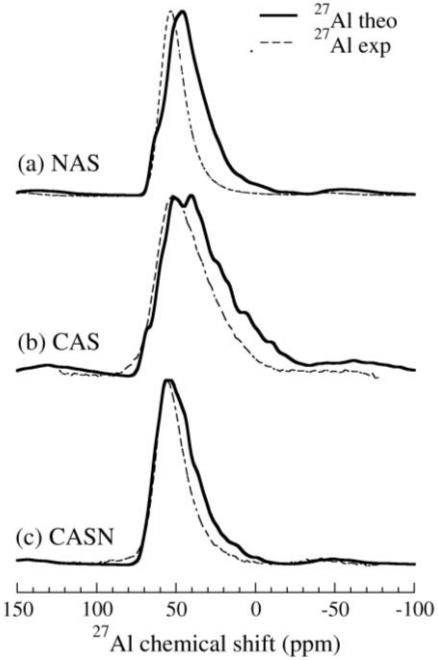

Figure 4.1. Comparison between normalized experimental spectra (collected at a magnetic field of 11.7 T, dashed lines) and computed (black solid lines) ^{27}Al MAS NMR spectra of NAS (a), CAS (b) and CASN (c) aluminosilicate glasses.

Al(Q^3) species. The presence of ^{V}Al in a glass is dependent on pressure and temperature of the sample preparation during the cooling phase. [4] If ^{V}Al atoms are present in the glass, they can be easily distinguished from the dominant Al(Q^4) units in a MAS spectrum. In fact, ^{V}Al δ_{iso} and C_Q provided by our calculations lie at around 20 ppm and 11.7 MHz, respectively. Conversely, Al(Q^3) species are not well distinguishable from Al(Q^4) units by a ^{27}Al MAS spectra. However, Al(Q^3) can be easily detect in a ^{17}O MAS spectra, being NBO(-Al) at least 20 ppm more deshielded than NBO(-Si) and BOs, as recently demonstrated in both experimental [5] and computational [3] investigations. Some of the aluminium atoms were found to be bonded up to 2 three-bridging oxigens (TBOs) but, as it will be better discussed below, their NMR parameters are not so much affected by this connectivity. This can explain why TBOs are difficult to detect by ^{27}Al NMR experiments.

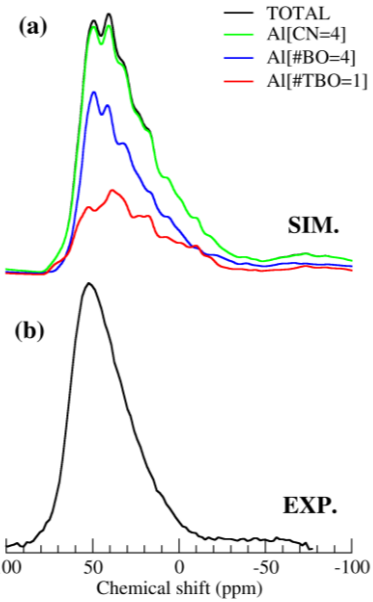

Figure 4.2. (a) Simulated and (b) experimental ^{27}Al MAS spectra of the CAS glass. Contribution of different Al species is presented in (a): green line represents 4-fold Al; blue line represents Al connected to 4 BOs; red line represents Al connected to 1 TBO and 3 BOs.

Regarding ^{27}Al spectra line shapes, experimental and theoretical spectra are quite similar for NAS (**Fig. 4.1.a**), fairly similar for CAS (**Fig. 4.1.b**) and very similar for CASN glass (**Fig. 4.1.c**). The theoretical line shape of the NAS glass

is broader than the experimental counterpart, denoting that the quadrupolar interactions are slightly overestimated in our DFT calculations.

Part of the overestimation can be ascribed to narrow inter-tetrahedra Al-O-T angles (where T= Al, Si) [6,7] due to the presence of small rings (three-membered). The observed spectra dissimilarity found in CAS glass (**Fig. 4.1.b**) is due to a shoulder at lower chemical shifts. This was found to be the spectroscopic fingerprint of aluminium atoms directly bonded to TBOs, which distort AlO_4 units, as evidenced in **Figure 4.2**. Actually, **Figure 4.3** shows that narrower Al-O-T angles, usually associated to Al-TBO bonds, determine lower ^{27}Al chemical shift (MD-GIPAW data). In support of our considerations, Al(Q^4) bonded to TBO were found to be more shielded than Al(Q^4)-BO by Iuga et al.[8], who characterized a CAS-type glass with heteronuclear multiple quantum correlation (HMQC) experiments. We conclude that the presence of aluminium atoms connected to TBOs seems to be overestimated in CAS model.

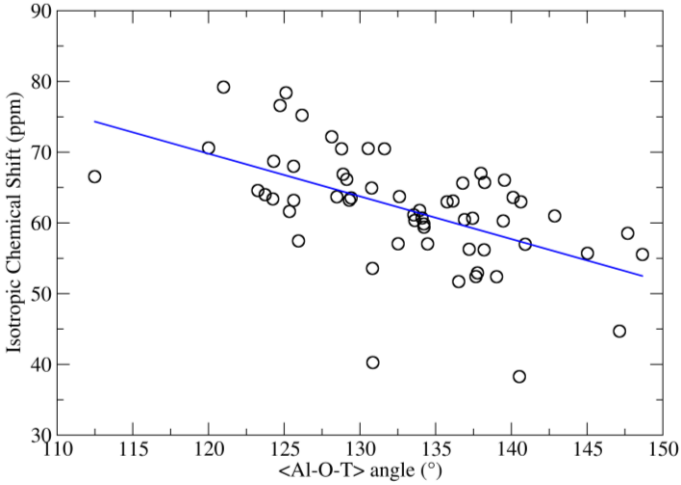

Figure 4.3. Simulated ^{27}Al isotropic chemical shift as a function of the mean <Al–O–T> angle.

Table 4.1. Theoretical and experimental values of ^{27}Al NMR parameters of 4-fold Al in NAS, CAS and CASN glasses (NBO: non-bridging oxygen; BO: bridging oxygen; TBO: tri-cluster oxygen). [(a)] δ_{iso}^{exp} are given for ^{27}Al. [(b)] CAS glasses contain AlO_6 (4NBO:2TBO δ_{iso}=14.7 ppm, C_Q=6.5 MHz, η_Q =0.5) and AlO_5 (2BO:3TBO δ_{iso}=22.5 ppm, C_Q=14.8 MHz η_Q =0.4 and 4BO:1TBO (pop=2) δ_{iso}=43.2 (1.4) ppm, C_Q=12.0 (2.7) MHz, η_Q =0.7 (0.2)) units. [(c)] Standard deviation not available: 1 site only in MD-GIPAW.

Al (Q^4) units	MD Pop.%	δ_{iso} (ppm)		C_Q (MHz)		η	
		Th.	Exp.	Th.	Exp.	Th.	Exp
NAS							
4BO	86.2	58.8 *(6.2)*	60.1 *(4.8)*	6.4 *(2.2)*	5.0 *(1.6)*	0.6 *(0.3)*	0.6 *(0.3)*
3BO:1TBO	13.8	61.4 *(5.3)*		10.1 *(3.5)*		0.7 *(0.2)*	
CAS[(b)]							
4BO	52.2	62.4 *(6.6)*		8.6 *(2.8)*		0.6 *(0.2)*	
3BO:1TBO	35.6	63.5 *(7.5)*		9.4 *(2.5)*		0.6 *(0.2)*	
2BO:2TBO	5.6	59.5 *(10.4)*	62.8 *(7.0)*	13.1 *(2.8)*	8.1 *(2.6)*	0.6 *(0.2)*	0.6 *(0.3)*
2BO:1TBO:1NBO	1.1	68.2[(c)]		23.7[(b)]		0.1[(b)]	
3BO:1NBO	1.1	65.9[(b)]		7.0[(b)]		0.8[(b)]	
CASN							
4BO	100.0	69.3 *(5.9)*	62.3 *(5.4)*	6.8 *(1.8)*	6.5 *(1.8)*	0.6 *(0.2)*	0.6 *(0.3)*

The comparison of theoretical and experimental values of the NMR parameters (η_Q, δ_{iso} and C_Q) is reported in **Table 4.1**. The experimental values have been obtained by fitting the ^{27}Al 3QMAS spectra, displayed in **Figure 4.4**, as described in reference [1]. To present the ^{27}Al NMR parameters, the AlO_4 units have also been classified with respect to the speciation of the four coordinating oxygen atoms (NBO, BO, TBO), in order to investigate the effects of the TBO-connectivity on the ^{27}Al NMR parameters, reported in **Table 4.1**. The theoretical δ_{iso} are in good agreement with the experimental value, especially for the $Al(BO)_4$ units, which are only slightly affected by the

increasing number of bonded TBOs. This is not the case for C_Q: a significant increase is found when TBOs coordinate Al. The similarity of δ_{iso} will make it difficult to observe Al sites connected to TBOs, where peaks are hidden in the dominant $Al(BO)_4$ line, which is broadened by the CaO content. In summary, our calculations suggest that TBOs are rather difficult to detect by ^{27}Al NMR spectroscopy.

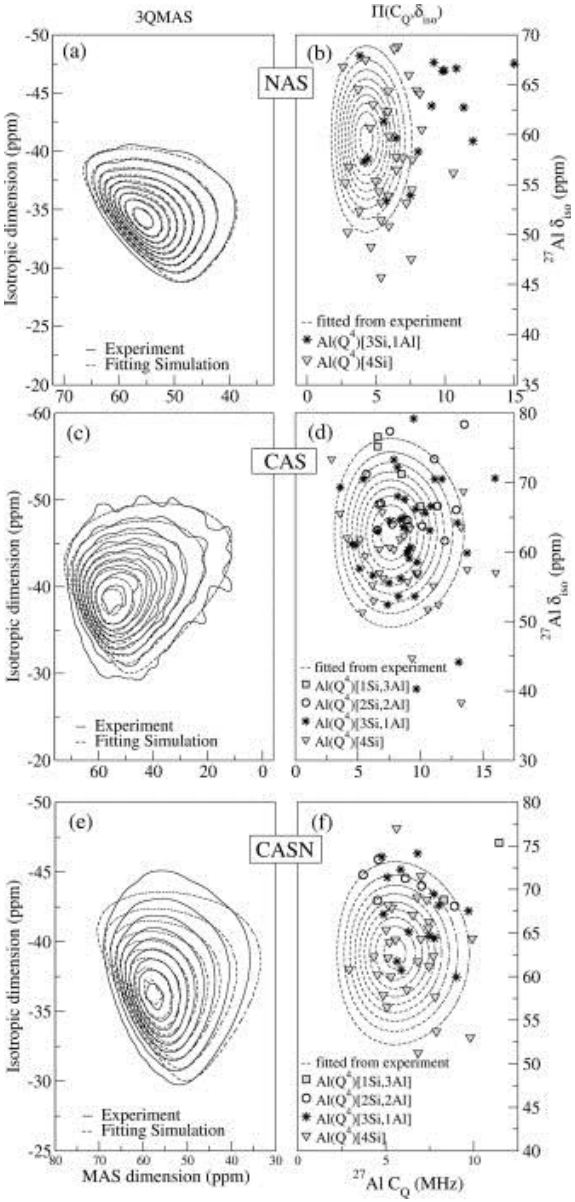

Figure 4.4. 3QMAS experimental spectra of NAS (a), CAS (c) and CASN (e) glasses (solid lines) and simulated spectra via fitting procedure (dashed lines); Π(CQ,δiso) distribution of NAS (b), CAS (d) and CASN (f) glasses: fitted from experiment (dashed lines) and theoretical counterparts derived from DFT calculations on MD derived models (symbols). Different symbols represent different $Al(Q^4)$ sites, and refer to the speciation of $Al(Q^4)$ in $Al(Q^4)[j\text{Si},4-j\text{Al}]$ species.

4.3. Aluminium second coordination sphere: framework disorder

Figure 4.4 shows ^{27}Al experimental 3QMAS spectra for all glasses, together with the comparison between computed NMR parameter distribution, $\Pi(C_Q,\delta_{iso})$, which are represented by symbols, and the experimentally determined distribution, represented by lines: NAS **(Fig 4.4.b)**, CAS **(Fig 4.4.d)** and CASN **(Fig 4.4.f)**. The figure shows that the agreement of C_Q distribution is satisfactory for both CAS and CASN glasses, whereas large discrepancy is observed for NAS glass. This is expected because of the overestimated presence of TBOs that are characterized by lower values of δ_{iso}. The overestimation of ^{27}Al C_Q in the case of NAS glass will be satisfactorily discussed later. Different symbols shown in **Figure 4.4** represent the speciation of Al(Q^4) surrounded by *j* Si and (*4-j*) Al atoms. These are named Al(Q^4)[*j*Si,(4-*j*)Al]. The relative distribution of the different Al(Q^4)[*j*Si,(4-*j*)Al] species on the $\Pi(C_Q,\delta_{iso})$ plot is not uniform neither on the C_Q, nor on δ_{iso} dimension; to the contrary, they tend to occupy different, even though quite overlapped regions, thus revealing a certain sensitivity of ^{27}Al NMR parameters to network chemical disorder. It is interesting to note that in NAS glass, the most of the overestimation of mean C_Q value is due to Al(Q^4)[3Si,1Al] species. This suggests that our structural model overestimates the presence of Al-O-Al bridges, which in fact are characterized by narrower averaged intertetrahedral angles. This, together with the vicinity of charge compensating Na, contributes to increase the average ^{27}Al C_Q value. The presence of these Al-O-Al linkages explains the observed discrepancy between the simulated and experimental ^{27}Al MAS NMR spectra (**Figure 4.1.a**).

The theoretical mean values of C_Q and δ_{iso} NMR parameters for Al(Q^4)[*j*Si,(4-*j*)Al] species are reported in **Table 4.2**. In all investigated glasses ^{27}Al δ_{iso} decreases by about 5 ppm for each ($SiO_{4/2}$) tetrahedra linked to $(AlO_{4/2})^-$. It ranges from 61.6 ppm, for Al(Q^4)[3Si,1Al], to 57.7 ppm, for Al(Q^4)[4Si], in the NAS model, from 70.4 ppm, for Al(Q^4)[2Si,2Al], to 58.7 ppm, for Al(Q^4)[4Si], in the CAS model, and from 72.0 ppm, for Al(Q^4)[1Si,3Al], to 62.9 ppm, Al(Q^4)[4Si], in CASN model. This trends nicely agrees with recent measurements and GIPAW computations in crystalline gehlenite, $Ca_2Al_2SiO_7$ [9]. In contrast, ^{27}Al C_Q decreases with the number of Si atoms in Al second coordination sphere.

Table 4.2. Isotropic chemical shift. δ_{iso}. and quadrupolar coupling constant. C_Q. for Al(Q^4) species surrounded by *j* silicon atoms and 4-*j* aluminium atoms in the second coordination sphere. Al(Q^4)[*j*Si.(4-*j*)Al]. MD-derived model and random percentage populations are also reported. [(a)] Population sum is not 100% because Al connected to TBO have been neglected from the analysis and only Al(Q^4) corresponding to $AlBO_4$ have been considered.

J	Pop% MD	δ_{iso} (ppm)	C_Q (MHz)	η_Q (MHz)	Pop% Random
			NAS[(a)]		
0	0.0	---	---	---	0.2
1	0.0	---	---	---	3.3
2	0.0	---	---	---	17.7
3	23.5	61.7(4.5)	7.5(2.5)	0.7	53.5
4	62.7	57.8(6.5)	6.0(1.9)	0.6	37.0
			CAS[(a)]		
0	0.0	---	---	---	2.6
1	0.0	---	---	---	15.3
2	7.8	70.5(5.3)	9.7(3.4)	0.7	34.5
3	23.3	63.5(5.0)	8.7(2.7)	0.7	34.5
4	21.1	58.8(5.7)	7.8(2.8)	0.6	13.0
			CASN		
0	0.0	---	---	---	0.4
1	3.9	72.0(4.6)	10.3(2.3)	0.7	4.7
2	11.8	70.6(2.0)	6.1(2.0)	0.6	21.1
3	27.4	67.2(4.7)	7.2(1.6)	0.7	42.2
4	56.9	62.9(5.7)	6.6(1.6)	0.6	31.6

Even though the values of NMR parameters provided in **Table 4.2** clearly show that different Al(Q^4)[*j*Si,4-*j*Al] species exhibit particular spectral fingerprints, and give a clear picture of the presence or absence of trends depending on structural features, they cannot be taken into account as constraints in fitting procedures of experimental spectra. In fact, the population of aluminium atoms in our merged models (90 in CAS, 51 in CASN, 51 in NAS) cannot be considered as statistically representative of aluminium population in real glass samples.

Table 4.2 also reports random population of Al(Q^4)[*j*Si,4-*j*Al] species. These coincide with the population of Al(Q^4)[*j*Si,4-*j*Al] obtained by randomly distributing network former cations around aluminium tetrahedra. The procedure for calculating random populations is provided in **Appendix A**. In all MD-derived models, the presence of species associated to Al clustering (and the formation of Al-O-Al bridges), like Al(Q^4)[4Al], Al(Q^4)[1Si,3Al] and Al(Q^4)[2Si,2Al], is generally underestimated with respect to a randomly calculated population. MD-derived populations of $(AlO_{4/2})^-$ tetrahedra linked to 3 or 4 ($SiO_{4/2}$) units are lower than random populations in CAS and NAS models, and higher than populations in CASN model. It is then possible to deduce that, for aluminosilicate glasses, Al clustering is lower than that expected for a random network chemical disorder. Nonetheless, species associated to Al-O-Al bridges were found in amorphous aluminosilicate, as demonstrated in several previous experimental work [10–15]. Moreover, the presence of Ca with respect to Na, which has lower field strength, favors the presence of Al-O-Al bonds.

4.4. Aluminium second coordination sphere: non-framework disorder

The investigation of the second coordination sphere of Al can be also developed in terms of neighboring modifier cations, with the aim to shed light on the role of Ca and Na when they are both present, like in CASN glass. This aspect can be quantified by the MD-derived ratio between the Al(Q^4)-Ca coordination number (CN_{Al}^{Ca}) and the Al(Q^4)-Na coordination number (CN_{Al}^{Na}), normalized with respect to the ratio of number of Ca (N_{Ca}) and Na (N_{Na}) in the model [16,17]:

$$\mathrm{R}_{\mathrm{Al}}^{\mathrm{Ca/Na}} = \frac{CN_{Al}^{Ca}}{CN_{Al}^{Na}} \cdot \frac{N_{Na}}{N_{Ca}} \qquad \text{(eq. 4.1)}$$

If $\mathrm{R}_{\mathrm{Al}}^{\mathrm{Ca/Na}}$ is greater than 1, this indicates that Ca is preferably located around Al(Q^4) with respect to Na; if it is smaller than 1, the preferential charge compensator is then Na. The obtained value of 0.74 demonstrates that Na tends to occupy Al surroundings in Ca-Na aluminosilicate glasses, thus it preferably behaves as the charge compensator of tetrahedral $(AlO_{4/2})^-$.

4.5. Relationships between ^{27}Al δ_{iso} and inter-tetrahedral angles

In **Chapter 3** we discussed about the importance of having accurate relationships between NMR parameters and structural features, as they make a reverse approach possible. In 1986 Lippmaa et al. [6] found that the average Al-O-Si angle (<Al-O-Si>) in crystalline samples linearly correlates with ^{27}Al δ_{iso} accordingly to this equation:

$$^{27}\mathrm{Al}\ \delta_{\mathrm{iso}} = -0.50 < \mathrm{Al-O-Si} > +132\ \mathrm{ppm} \qquad \text{(Eq. 4.2)}$$

In 2000, Angeli et al.[7] adopted this correlation to estimate the distribution <Al-O-Si> angles in a glass, starting from an experimental set of ^{27}Al δ_{iso} obtained by fitting a ^{27}Al MQMAS spectra.

In this work we employed sets of computed ^{27}Al δ_{iso} and <Al-O-Si> to check the validity of the linear correlation proposed by Lippmaa et al. [6] in the case of the amorphous phases under study. **Figure 4.5** displays the plot for NAS (**Fig. 4.5.a**), CAS (**Fig. 4.5.b**) and CASN (**Fig. 4.5.c**).

Analogously to what observed for silicon (**Paragraph 3.5**), the distribution of ^{27}Al δ_{iso} values does not correlate very well with the <Al–O–T> angle, and the goodness-of-fit of the linear correlations seems to vary as a function of glass composition: better for CASN glass, worse for CAS and NAS. Nonetheless, when Al connectivity to different oxygen species (BOs, NBOs, TBOs) is taken into account, then linear correlations are more evident and slope and intercept values are rather independent on chemical composition.

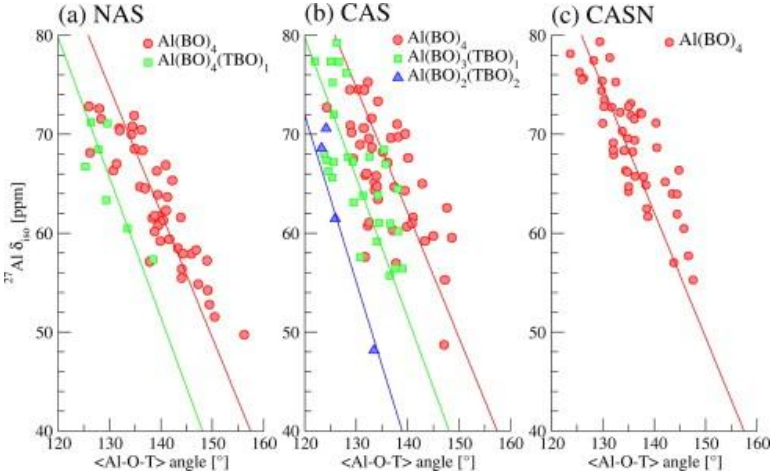

Figure 4.5. Plot of ^{27}Al δ_{iso} vs <Al-O-T> reported for different connectivity environments of Al in NAS, CAS and CASN. $Al(BO)_4$ are red circles, $Al(BO)_3(TBO)_1$ are green squares and $Al(BO)_2(TBO)_2$ are blue triangles. Linear regression fitting lines are also reported with coherent colors.

However, it seems evident from Al(BO_4) sites that the correlation is weaker for CAS and better for CASN and NAS. As explained in **Paragraph 4.4**, in CAS glass the charge compensator role is played by Ca. This fact brings us to state that the presence of Ca around ^{27}Al nuclei tends to weaken the (δ_{iso};T-O-T) correlation, in analogy to what we observed for Si, as discussed in **Paragraph 3.5**.

By comparing computed and experimental data, we realized that glass samples contain only negligible amounts of Al-TBO and Al-NBO bonds: the vast majority of Al atoms are four-folded Al(Q^4) sites, thus characterized by an Al$(BO)_4$-type connectivity. We then assume that ^{27}Al δ_{iso} values extracted from an experimental spectra are generated by one kind of Al site, and that, for the compositions under study, the correlation with Al-O-T angles is as good as the one showed by the CASN model (**Fig. 4.5.c**). The inversion procedure of a ^{27}Al MAS spectra with a simple linear function like the one introduced by Lippmaa et al. [6] is then a reliable path to get to the estimation of Al-O-T angles in the glass samples.

4.6. Final remarks

The soundness of the models was proved by investigating the agreement between theoretical and experimental ^{27}Al MAS spectra and $\Pi(C_Q,\delta_{iso})$, distributions. The observed discrepancies were mainly ascribed to the overestimation of TBOs and Al-O-Al bridges, in CAS and NAS models respectively. Although the excessive presence of these structural feature, the interpretation ability of the MD-GIPAW data was not undermined.

Indeed, we found that, for aluminosilicate glasses, Al clustering in the network is lower than that expected for a random network chemical disorder. We also found that ^{27}Al δ_{iso} decreases by about 5 ppm for each ($SiO_{4/2}$) tetrahedra linked to $(AlO_{4/2})^-$, and that ^{27}Al C_Q tends to decrease with the number of Si atoms in Al second coordination sphere.

The investigation of non-framework cation arrangement around Al leads to the conclusion that, when Ca and Na are both present, Na tends to occupy Al surroundings in Ca-Na aluminosilicate glasses, thus it preferably behaves as the charge compensator of tetrahedral $(AlO_{4/2})^-$.

Finally, we studied the correlation between ^{27}Al δ_{iso} and Al-O-T angles, finding that Al-O connectivity affects it. However, simple univariate linear correlations can be employed to "inverse" a ^{27}Al spectra of aluminosilicate glasses with the presented compositions because, in general, only one kind of Al-O connectivity, the $Al(BO)_4$, is expected.

Bibliography

[1] Angeli F, Gaillard M, Jollivet P, Charpentier T. Contribution of 43Ca MAS NMR for probing the structural configuration of calcium in glass. Chem Phys Lett 2007;440:324–8. doi:10.1016/j.cplett.2007.04.036.

[2] Gambuzzi E, Pedone A, Menziani MC, Angeli F, Caurant D, Charpentier T. Probing silicon and aluminium chemical environments in silicate and aluminosilicate glasses by solid state NMR spectroscopy and accurate first-principles calculations. Geochim Cosmochim Acta 2014;125:170–85. doi:10.1016/j.gca.2013.10.025.

[3] Pedone A, Gambuzzi E, Malavasi G, Menziani MC. First-principles simulations of the 27Al and 17O solid-state NMR spectra of the CaAl2Si3O10 glass. Theor Chem Acc 2012;131. doi:10.1007/s00214-012-1147-5.

[4] Li D, Secco RA, Bancroft GM, Fleet ME. Pressure induced coordination change of Al in silicate melts from Al K edge XANES of high pressure $NaAlSi_2O_6$ -$NaAlSi_3O_8$ glasses. Geophys Res Lett 1995;22:3111–4. doi:10.1029/95GL03175.

[5] Allwardt JR, Lee SK, Stebbins JF. Bonding preferences of non-bridging O atoms: Evidence from 17O MAS and 3QMAS NMR on calcium aluminate and low-silica Ca-aluminosilicate glasses. Am Min 2003;88:949–54.

[6] Lippmaa E, Samoson A, Magi M. High-resolution aluminum-27 NMR of aluminosilicates. J Am Chem Soc 1986;108:1730–5. doi:10.1021/ja00268a002.

[7] Angeli F, Delaye J-M, Charpentier T, Petit J-C, Ghaleb D, Faucon P. Investigation of Al–O–Si bond angle in glass by 3Q-MAS NMR and molecular dynamics. Chem Phys Lett 2000;320:681–7. doi:10.1016/S0009-2614(00)00277-3.
[8] Iuga D, Morais C, Gan Z, Neuville DR, Cormier L, Massiot D. NMR Heteronuclear Correlation between Quadrupolar Nuclei in Solids. J Am Chem Soc 2005;127:11540–1. doi:10.1021/ja052452n.
[9] Florian P, Veron E, Green TFG, Yates JR, Massiot D. Elucidation of the Al/Si Ordering in Gehlenite $Ca_2Al_2SiO_7$ by Combined ^{29}Si and ^{27}Al NMR Spectroscopy/Quantum Chemical Calculations. Chem Mater 2012;24:4068–79. doi:10.1021/cm3016935.
[10] McMillan P, Piriou B, Navrotsky A. A Raman spectroscopic study of glasses along the joins silica-calcium aluminate, silica-sodium aluminate, and silica-potassium aluminate. Geochim Cosmochim Acta 1982;46:2021–37. doi:10.1016/0016-7037(82)90182-X.
[11] Murdoch JB, Stebbins JF, Carmichael ISE. High-resolution 29Si NMR study of silicate and aluminosilicate glasses: the effect of network-modifying cations. Am Min 1985;70:332–43.
[12] Tossell JA, Sághi-Szabó G. Aluminosilicate and borosilicate single 4-rings: Effects of counterions and water on structure, stability, and spectra. Geochim Cosmochim Acta 1997;61:1171–9. doi:10.1016/S0016-7037(96)00397-3.
[13] Lee SK, Stebbins JF. The degree of aluminium avoindance in aluminosilicate glasses. Am Min 1999;84:937–45.
[14] Lee SK, Stebbins JF. Al–O–Al and Si–O–Si sites in framework aluminosilicate glasses with Si/Al=1: quantification of framework disorder. J Non-Cryst Solids 2000;270:260–4. doi:10.1016/S0022-3093(00)00089-2.
[15] Stebbins JF, Lee SK, Oglesby V. Al-O-Al oxygen sites in crystalline aluminates and aluminosilicate glasses; high-resolution oxygen-17 NMR results. Am Min n.d.;84:983–6.
[16] Pedone A. Properties Calculations of Silica-Based Glasses by Atomistic Simulations Techniques: A Review. J Phys Chem C 2009;113:20773–84. doi:10.1021/jp9071263.
[17] Tilocca A, Cormack AN, de Leeuw NH. The Structure of Bioactive Silicate Glasses: New Insight from Molecular Dynamics Simulations. Chem Mater 2007;19:95–103. doi:10.1021/cm061631g.

CHAPTER 5

^{17}O NMR spectroscopy: oxygen environment in silicate and aluminosilicate glasses

^{17}O MAS and MQMAS spectra are probably the most powerful instruments for the characterization of a glass overall structure. In fact, O is the *linking* atom of the network, and coordinates also non-framework cations. Hence, the information provided by NMR response of ^{17}O nuclei could acknowledge for structural and chemical arrangements of both network and extra-framework domains.

In this chapter, we interpret MD-derived models to get to an unambiguous view of the local structure around oxygen atoms in all the 6 compositions introduced in **Paragraph 1.6**. Three silicate glasses: a calcium (CS: $40CaO{\cdot}60SiO_2$), a sodium (NS: $40Na_2O{\cdot}60SiO_2$), and a calcium–sodium silicate glass (CSN: $20CaO{\cdot}20Na_2O{\cdot}60SiO_2$); and three aluminosilicate glasses: calcium (CAS: $20CaO{\cdot}20Al_2O_3{\cdot}60SiO_2$), sodium (NAS: $11Na_2O{\cdot}11Al_2O_3{\cdot}78SiO_2$) and calcium–sodium aluminosilicate glass (CNAS: $20CaO{\cdot}10Na_2O{\cdot}10Al_2O_3{\cdot}60SiO_2$).

Experimental spectra, where available, are used to validate the models. Theoretical ^{17}O MAS and 3QMAS spectra are simulated for specific O sites, in order to highlight spectroscopic fingerprints that are characteristic of particular structural features (Al-O-Al bridges, Si-O-Na coordinations, etc…).

The collection of experimental spectra was not performed by us, but ^{17}O MAS spectra of glasses having compositions similar to the glasses under study were taken from the literature:

- ^{17}O MAS spectra of $75SiO_2{\cdot}25Na_2O$ [1] as experimental reference for NS;

- ^{17}O MAS spectra of $61.5SiO_2 \cdot 38.5CaO$ [2] as experimental reference for CS;
- ^{17}O MAS spectra of $12.5Na_2O \cdot 12.5Al_2O_3 \cdot 75SiO_2$ [3] as experimental reference for NAS;
- ^{17}O MAS spectra of $25CaO \cdot 25Al_2O_3 \cdot 50SiO_2$ [4] as experimental reference for CAS.

The reader is invited to refer to the listed references for experimental details. The dissertation presented here after was published on the Journal of Physical Chemistry C [5].

5.1. Cation Distribution around Oxygen Atoms in Na–Ca Silicate Glasses

Figure 5.1 reports the ^{17}O MAS and 3QMAS spectra simulated at 14.1 T of the silicate glasses, CS, NS and CSN, together with the available experimental counterparts. The excellent agreement between the theoretical ^{17}O MAS NMR and experimental spectra validates the structural models obtained by MD simulations, allowing the inference of relationships between structural data and NMR response.

The theoretical ^{17}O MAS and 3QMAS spectra for the different oxygen speciation present in the MD simulations show that the oxygen atoms at the Si–O–Na sites are more shielded (peak about 25 ppm, **Figure 5.1.a**) than the ones at the Si–O–Ca site (peak maximum about 100 ppm, **Figure 5.1.c**). Thus, the signals of the Si–O–Na and Si–O–Si sites are overlapped in a MAS spectra, while the signals of the Si–O–Ca and Si–O–Si ones lie in different zones. Differently, Si-O-Ca, Si-O-Si and Si-O-Na peaks in NS and CS glasses

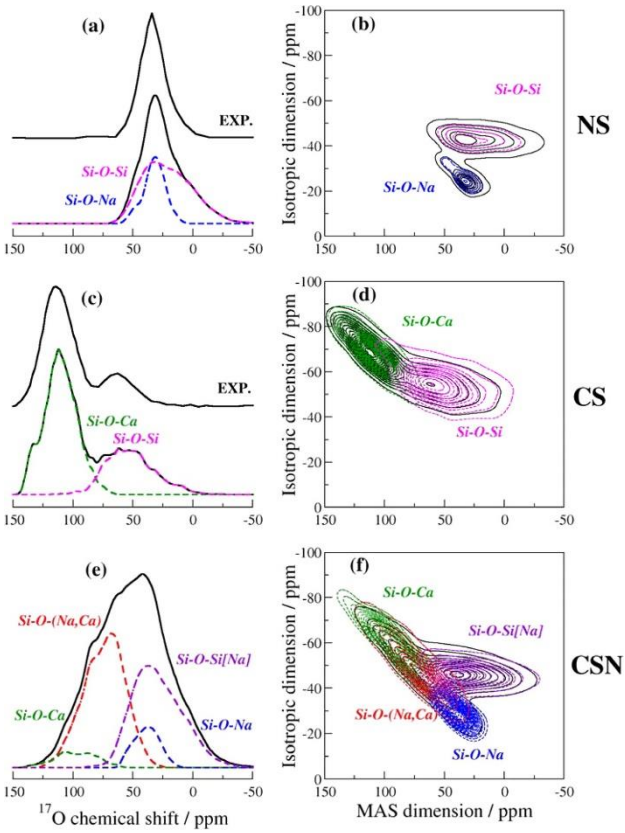

Figure 5.1. Computed 17O MAS and MQMAS spectra of NS, CS and CSN glasses. Contribution of different O sites are highlighted in color. Experimental 17O MAS are taken from the literature (ref. [1] for NS and ref. [2] for CS). Modifier cations surrounding BOs are labeled in square brakets, while those surrounding NBOs in parentheses.

are well resolved in the theoretical 3QMAS spectra and their detection is straightforward.

Both the MAS and 3QMAS spectra show that the spread of the chemical shift distribution of NBO in the NS glass is smaller than that of the NBO in the CS glass, indicating that Ca is found around oxygen in a more disordered arrangement with respect to the Na atoms. Moreover, a wide distribution of chemical shifts of NBOs belonging to the Si–O–Na and Si–O–Ca sites is observed in the CSN glass, since the peak positions of the mixed Si–O–(Na,Ca) sites move toward higher chemical shifts as the Ca content around

oxygen increases. For the CSN glass, the simulated ^{17}O 3QMAS spectrum reported in **Figure 5.1.f** shows that the Si–O–(Na,Ca) signals completely overlap with the Si–O–Ca and Si–O–Na ones; therefore, a direct fitting of the experimental spectrum without the help of constraints derived from NMR calculations is more difficult. [6]

The computed mean NMR parameters (δ_{iso}, C_Q, η_Q) and the population of the NBO and BO sites present in the CSN MD-generated glass model are reported in Tables **5.1** and **5.2** respectively. Analogous data for CASN glass can be found in ref. [5]. The MD oxygen site populations are compared to those calculated for a random distribution of Na and Ca around oxygen atoms. Formulae to calculate random distributions are reported in **Appendix B**.

As already highlighted, the isotropic chemical shift of NBO atoms decreases with the number of Na cations around the oxygens, whereas it increases with the amount of Ca cations. **Table 5.1** also shows that, on average, the structural models investigated contain a majority of NBO coordinated to Ca and Na in a mixed state.

The total amount of Si–NBO(Na,Ca) sites is 37.9%, while the NBOs coordinated to only Na or Ca species amount to 7.2 and 4.6%, respectively, of the total oxygen atoms. The amount of Si–NBO(Ca,Na) sites is higher than that predicted by employing a random distribution of cations around NBO (30.7%), whereas the amount of Si–NBO(Na) sites is lower than that predicted by a random distribution (15.5%), and the amount of Si–NBO(Ca) sites is higher than that predicted by a random distribution (2.4%).

Therefore, these results clearly indicate that there is extensive mixing of Ca and Na around NBO in soda-lime silicate glasses.

Table 5.1. Computed NMR parameters and population of the NBO speciation in the CSN glass obtained from MD simulations and random distribution of Na and Ca cations around oxygen. Standard deviations are given in parentheses.

NBO species	δ_{iso} [ppm]	C_Q [MHz]	η_Q	MD site population	Random Site population
Si-NBO(Na)	**47.4(8.5)**	**2.57(0.27)**	**0.38(0.18)**	**7.2**	**15.5**
Si-NBO(1Na)	-	-	-	-	0.1
Si-NBO(2Na)	54.1(7.0)	2.78(0.13)	0.25(0.15)	0.9	4.0
Si-NBO(3Na)	47.7(7.4)	2.57(0.23)	0.43(0.17)	4.2	9.8
Si-NBO(4Na)	43.7(9.9)	2.67(0.31)	0.31(0.20)	2.1	1.6
Si-NBO(Ca)	**107.6(16.0)**	**2.73(0.28)**	**0.39(0.21)**	**4.6**	**2.4**
Si-NBO(1Ca)	89.7	2.62	0.35	0.2	0.1
Si-NBO(2Ca)	105.4(18.5)	2.75(0.31)	0.43(0.24)	2.8	1.0
Si-NBO(3Ca)	113.9(8.7)	2.69(0.27)	0.35(0.19)	1.6	1.3
Si-NBO(Ca,Na)	**83.8(16.7)**	**2.74(0.31)**	**0.32(0.17)**	**37.9**	**30.7**
Si-NBO(1Ca,1Na)	85.0(14.3)	2.70(0.24)	0.33(0.20)	5.1	3.8
Si-NBO(1Ca,2Na)	75.6(10.3)	2.71(0.29)	0.31(0.14)	15.7	13.4
Si-NBO(1Ca,3Na)	70.1(15.3)	2.66(0.31)	0.44(0.19)	4.6	3.2
Si-NBO(1Ca,4Na)	83.3(8.6)	2.37(0.72)	0.36(0.07)	0.2	0.0
Si-NBO(2Ca,1Na)	100.5(12.3)	2.85(0.33)	0.28(0.16)	11.1	7.2
Si-NBO(2Ca,2Na)	83.4(8.9)	2.65(0.29)	0.33(0.18)	1.0	2.3
Si-NBO(3Ca,1Na)	114.2(18.0)	2.91(0.02)	0.26(0.20)	0.2	0.8

The strong tendency for the formation of dissimilar cation pairs observed for the CSN glass is probably due to the very similar ionic radii of Ca and Na. In fact, previous studies on Ba–Mg [7] and K–Li [8] silicate glasses have shown that larger differences in ionic radii increase the site mismatch energy, thus contributing to the marked ordering around NBO. However, the achievement of a homogeneous distribution of charges in the glass can also play an

important role in the formation of dissimilar pairs. The non-random distribution of Ca and Na ions in silicate glasses affects the dynamics of Na^+ and the related transport properties. [9,10] Conversely, a detailed characterization of the environment of the BO sites, in MD three-dimensional structural models within a cutoff of 3.2 Å, whose different populations are reported in **Table 5.2**, shows that the population of BOs surrounded by sodium (Si–BO–Si[Na]) is 35.7%, whereas those of the Si–BO–Si[Ca,Na] and Si–BO–Si[Ca] sites are 4.4 and 5.2%, respectively. Therefore, BOs prefer to be surrounded by sodium ions rather than by calcium.

Table 5.2. Computed NMR parameters and population of the BO speciation in CSN glass obtained from MD simulations and random distribution of Na and Ca cations around oxygen. Standard deviations are given in parentheses. Formulae to calculate random population in Appendix B.

BO species	δ_{iso} [ppm]	C_Q [MHz]	η_Q	MD site population	Random Site population
Si-BO-Si(Na)	**63.7(7.7)**	**5.05(0,45)**	**0.37(0.18)**	**35.7**	**25.9**
Si-BO-Si(1Na)	62.6(7.5)	5.09(0.45)	0.37(0.18)	20.4	17.4
Si-BO-Si(2Na)	64.6(7.3)	5.03(0.43)	0.37(0.18)	14.1	7.8
Si-BO-Si(3Na)	69.0(10.3)	4.74(0.60)	0.38(0.22)	1.2	0.6
Si-BO-Si(Ca)	**72.8(10.1)**	**5.02(0.49)**	**0.46(0.22)**	**5.6**	**10.6**
Si-BO-Si(1Ca)	72.8(10.1)	5.02(0.49)	0.46(0.22)	5.6	8.6
Si-BO-Si(2Ca)	-	-	-	-	1.9
Si-BO-Si(Ca,Na)	**72.2(8.4)**	**4.65(0.42)**	**0.50(0.19)**	**4.4**	**9.1**
Si-BO-Si(1Ca,1Na)	72.4(9.5)	4.70(0.45)	0.50(0.19)	3.2	7.6
Si-BO-Si(1Ca,2Na)	72.5(4.4)	4.39(0.29)	0.51(0.30)	0.7	0.9
Si-BO-Si(1Ca,3Na)	65.8	4.93	0.41	0.2	0.1
Si-BO-Si(2Ca,1Na)	74.8	4.36	0.49	0.2	0.5
Si-BO-Si	**59.8(10.7)**	**5.27(0.49)**	**0.27(0.15)**	**4.6**	**4.6**

The results reported in **Table 5.2** also highlights that, as a consequence of the interaction between the network-modifying cations and the bridging oxygen network, the isotropic chemical shift of BOs increases with the number of Na or Ca ions within the first coordination sphere of the oxygens. The most common environments around NBO and BO, that is Si–NBO(1Ca,2Na) 15.7%, Si–NBO(2Ca,1Na) 11.1%, Si–BO–Si[1Na] 20.4%, and Si–BO–Si[2Na] 14.1% sites, are shown in **Figure 5.2**.

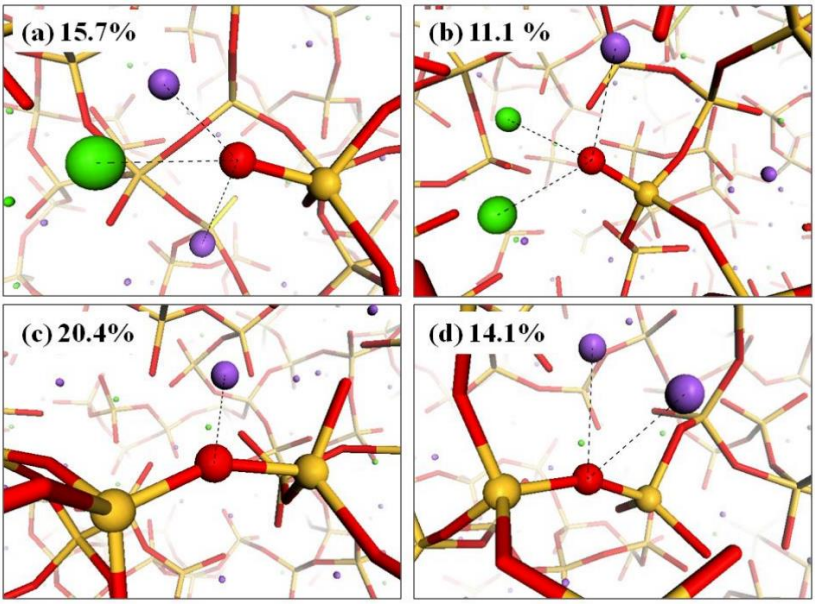

Figure 5.2. The most common oxygen environments in the CSN glass: (a) Si-NBO(1Ca,2Na), (b) Si-NBO(2Ca,1Na), (c) Si-BO(1Na)-Si and (d) Si-BO(2Na)-Si sites. Oxygens, sodium and calcium atoms are represented as red, violet and green spheres. Silicon atoms are represented as yellow sticks.

5.2. Cation Distribution around Oxygen Atoms in Na–Ca Aluminosilicate Glasses

Figure 5.3 reports the theoretical ^{17}O MAS NMR spectra of the three aluminosilicate glasses studied, together with the contributions of the different oxygen speciation found in the MD-derived structural models. The overall shape of the spectra well reproduces the experimental ones available in the literature and reported for validation purposes.

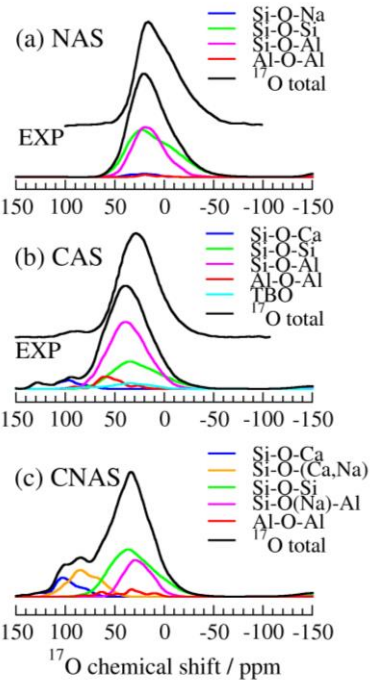

Figure 5.3. Theoretical ^{17}O MAS NMR spectra at 14.1T for NAS, CAS and CNAS glasses. The spectra of the different O sites are highlighted in color. The experimental ^{17}O MAS spectra taken from literature are also reported for the NAS [3] and CAS [4] glasses.

Both the CAS and NAS glasses have a tectosilicate composition, in which the $[CaO]/[Al_2O_3]$ and $[Na_2O]/[Al_2O_3]$ ratios are equal to 1. Therefore, in accordance with the *compensated continuous random network model* of aluminosilicate glasses, these systems should reach maximum polymerization, and no NBO and three bridging oxygen (TBO) species should be detected. However, MD simulations show an incomplete polymerization of both glasses and the presence of NBOs in the system. At the same time, to preserve the total number of Al–O and Si–O bonds, the presence of NBO is compensated by TBO species, in agreement with previous high

resolution 3QMAS NMR [4] and viscosity measurements [11] carried out on similar compositions. A detailed analysis of the relative amount of such tricluster sites shows that CAS and NAS glasses contain 4.9 and 1.7% TBO, respectively. Thus, higher field strength cations promote the formation of NBO and TBO because of the competition for low-coordinate environments with respect to lower field strength cations. In fact, Ca prefers to be coordinated by NBO than by BO in its first coordination shell [12]. Interestingly, in agreement with experimental evidence [13,14], all the NBOs are associated with Si atoms rather than Al ones. This is observed also for the CNAS glass, whose composition allows NBOs to be present in the structure. However, in this case no TBOs have been found in the MD-derived structural models. The characterization of the TBOs in terms of ^{17}O NMR parameters will be discussed in **Paragraph 5.3**.

Figure 5.3.c shows that the large peak between 110 and 60 ppm in the ^{17}O MAS spectra of the CNAS glass stems from different types of NBOs (Si–NBO–Ca and Si–NBO–(Ca,Na)).

Regarding the BO sites, **Figure 5.3** also shows that there is a significant overlap among the Si–O–Si, Si–O–Al, and Al–O–Al peaks in the ^{17}O MAS spectra, a fact that makes it difficult to quantify the fractions of oxygen sites and explore the effect of composition on the topological disorder in the Si–O–Al sites from experiments alone.

The ^{17}O 3QMAS spectra, reported in **Figure 5.4**, show better resolved multiple oxygen sites. In particular, the ^{17}O 3QMAS spectra of the NAS and CNAS glasses show that the contributions provided by the Si–O–Si, Si–O–Al and Al–O–Al sites are well separated, while the Si–O–Al spectrum is overlapped with those of Si–O–Si and Al–O–Al for the CAS glass. The ordering of framework

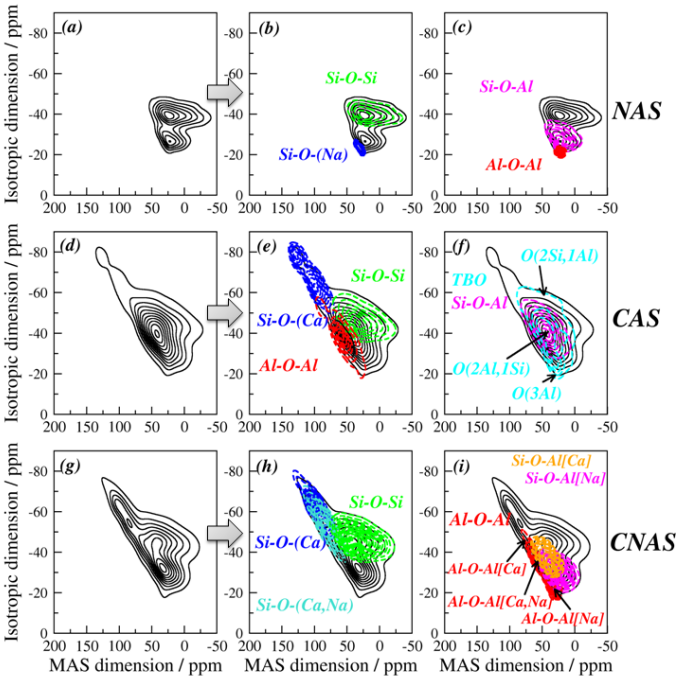

Figure 5.4. Theoretical ^{17}O 3QMAS NMR spectra at 14.1T for CAS, CNAS and NAS glasses. The spectra of the different O sites are highlighted in color.

Si and Al cations in aluminosilicate glasses can be deduced by comparing the number of T–O–T bridges (T = Al/Si) obtained by MD simulations and the site populations provided by a random distribution of Al and Si around BOs (see **Table 5.3**), recalling that when the ratio is equal to 1 the network framework cations are randomly distributed. Formulae adopted to calculate random populations are reported in **Appendix C**.

Table 5.3. BO site populations of the CAS, CNAS and NAS glasses derived from MD simulations and a random distribution of Al and Si connected to the central oxygen. In the latter calculation, it has been assumed that Al and Si cations are 4-coordinated and that the total amount of BO is that given by the glass compositions.

Sites	CAS		CNAS		NAS	
	MD	Random	MD	Random	MD	Random
Si-O-Si	0.28	0.36	0.36	0.44	0.57	0.61
Si-O-Al	0.54	0.48	0.38	0.29	0.38	0.34
Al-O-Al	0.06	0.16	0.04	0.05	0.01	0.05

In glasses where the number of Si–O–Al sites is lower and the number of Si–O–Si sites is higher than that obtained for a random distribution, the tendency toward clustering among framework units is more pronounced and phase separation can occur. However, this is not the case for the glasses studied here because the amount of Si–O–Al sites is always higher than the random one, thus denoting an extensive mixing of these framework units which has important implications for the macroscopic properties of magmas.

However, this is not the case for the glasses studied here because the amount of Si–O–Al sites is always higher than the random one, thus denoting an extensive mixing of these framework units which has important implications for the macroscopic properties of magmas.

The results of this study also show that the ratio between Al–O–Al sites derived by means of the MD simulations and a random distribution is higher for CAS (0.38) than NAS (0.20) glasses, denoting that higher field cations (Ca vs Na) tend to promote disorder.

In the ^{17}O 3QMAS spectra of the CNAS glass reported in **Figure 5.4**, the contributions of the BO[Na], BO[Ca,Na], and BO[Ca] sites are highlighted. These are located in slightly different regions of the whole spectrum because of the increase of the isotropic chemical shift with the number of Ca atoms in the first coordination sphere of O.

The NMR parameters of the NBO and BO sites found in the CNAS glass and the relative populations of the different sites are reported in **Tables 5.4** and **5.5**, respectively. The corresponding data values for CAS and NAS glasses are reported in the Supporting Information of ref. [5].

Table 5.4. NBO Site populations obtained from MD simulations and computed NMR parameters of the CNAS glass. Standard deviations are given in parentheses.

NBO species	Site Pop.	δ_{iso} [ppm]	C_Q [MHz]	η_Q
Si-NBO [all]	**22.2**	**97.5(18.7)**	**2.74(0.30)**	**0.35(0.19)**
Si-NBO(Na)	**0.4**	**65.7(15.1)**	**2.25(0.22)**	**0.41(0.19)**
Si-NBO(2Na)	0.2	76.3	2.09	0.28
Si-NBO(3Na)	0.2	55.0	2.41	0.55
Si-NBO(Ca)	**8.1**	**110.8(16.7)**	**2.77(0.28)**	**0.34(0.16)**
Si-NBO(1Ca)	0.4	100.6(12.0)	2.68(0.18)	0.46(0.23)
Si-NBO(2Ca)	5.7	111.3(17.9)	2.78(0.26)	0.35(0.17)
Si-NBO(3Ca)	2.0	111.9(14.3)	2.75(0.38)	0.30(0.14)
Si-NBO(Ca,Na)	**13.7**	**90.6(14.7)**	**2.75(0.31)**	**0.36(0.20)**
Si-NBO(1Ca,1Na)	5.7	86.6(12.0)	2.78(0.28)	0.32(0.18)
Si-NBO(1Ca,2Na)	2.9	81.6(10.7)	2.71(0.38)	0.33(0.14)
Si-NBO(2Ca,1Na)	5.1	100.3(14.5)	2.73(0.30)	0.41(0.24)

The analysis of the data listed in **Tables 5.4** and **5.5** also reveals that for both NBO and BO species the isotropic chemical shift decreases with the number of Na cations and increases with the number of Ca ones. The quadrupolar coupling constant C_Q is about 2.8 MHz for NBOs, 5 MHz for Si–BO–Si sites, 3.6 MHz for Si–BO–Al sites, and 2.1 MHz for Al–BO–Al sites. In the case of BOs, the C_Q value of BO sites surrounded by only Na cations is higher than the one of BOs surrounded by only Ca cations, which in turn is higher than that of BOs coordinated in a mixed Na–Ca state.

Table 5.5. BO Site populations obtained from MD simulations and computed NMR parameters of the CNAS glass. Standard deviations are given in parentheses.

BO species	Site Pop.	δ_{iso} [ppm]	C_Q [MHz]	η_Q
Si-BO-Si [all]	**36.3**	**65.1(12.3)**	**5.00(0.56)**	**0.43(0.23)**
Si-BO-Si(Na)	**16.0**	**63.2(10.8)**	**5.01(0.53)**	**0.42(0.21)**
Si-BO-Si(1Na)	13.6	63.3(10.3)	5.02(0.57)	0.44(0.21)
Si-BO-Si(2Na)	2.4	62.8(14.0)	5.01(0.26)	0.33(0.18)
Si-BO-Si(Ca)	**8.4**	**74.9(11.9)**	**4.66(0.43)**	**0.60(0.22)**
Si-BO-Si(1Ca)	8.2	74.6(12.0)	4.68(0.42)	0.59(0.22)
Si-BO-Si(2Ca)	0.2	84.4	3.94	0.62
Si-BO-Si(Ca,Na)	**1.5**	**75.6(4.6)**	**4.36(0,61)**	**0.65(0.18)**
Si-BO-Si(1Ca,1Na)	1.5	75.6(4.6)	4.36(0.61)	0.65(0.18)
Si-BO-Si(n.c.)	**10.4**	**58,6(9.6)**	**5.35(0.41)**	**0.27(0.16)**
Si-O-Al [all]	**38.0**	**50.0(11.3)**	**3.64(0.47)**	**0.48(0.24)**
Si-BO-Al(Na)	**17.1**	**44.9(7.3)**	**3.69(0.41)**	**0.43(0.21)**
Si-BO-Al(1Na)	13.8	45.2(7.4)	3.69(0.44)	0.44(0.21)
Si-BO-Al(2Na)	3.3	43.8(7.2)	3.70(0.31)	0.38(0.20)
Si-BO-Al(Ca)	**10.8**	**58.8(9.0)**	**3.45(0.45)**	**0.62(0.22)**
Si-BO-Al(1Ca)	10.4	58.3(8.8)	3.45(0.45)	0.63(0.21)
Si-BO-Al(2Ca)	0.4	69.8(5.7)	3.44(0.33)	0.41(0.37)
Si-BO-Al(Ca.Na)	**3.3**	**60.5(9.2)**	**3.37(0.44)**	**0.61(0.21)**
Si-BO-Al(1Ca.1Na)	3.3	60.48(9.21)	3.37(0.44)	0.61(0.21)
Si-BO-Al	**6.8**	**43.9(11.5)**	**3.95(0.46)**	**0.31(0.20)**
Al-O-Al [all]	**3.5**	**45.4(21.4)**	**2.06(0.38)**	**0.59(0.21)**
Al-BO-Al(Na)	**1.8**	**30.7(11.8)**	**2.13(0.57)**	**0.53(0.26)**
Al-BO-Al(1Na)	0.9	35.3(14.8)	2.18(0.31)	0.43(0.25)
Al-BO-Al(2Na)	0.9	26.1(7.2)	2.09(0.82)	0.62(0.25)
Al-BO-Al(Ca)	**1.3**	**65.8(17.7)**	**2.04(0.36)**	**0.63(0.15)**
Al-BO-Al(1Ca)	1.1	65.8(19.8)	2.11(0.34)	0.64(0.16)
Al-BO-Al(2Ca)	0.2	66.3	1.67	0.56
Al-BO-Al(Ca.Na)	**0.4**	**43.1(7.6)**	**1.84(0.40)**	**0.71(0.06)**
Al-BO-Al(1Ca.1Na)	0.4	43.1(7.6)	1.84(0.40)	0.71(0.06)

Therefore, these different types of O sites occupy well-defined regions of the (C_Q,δ) space and are distinguishable in the 3QMAS spectra as demonstrated

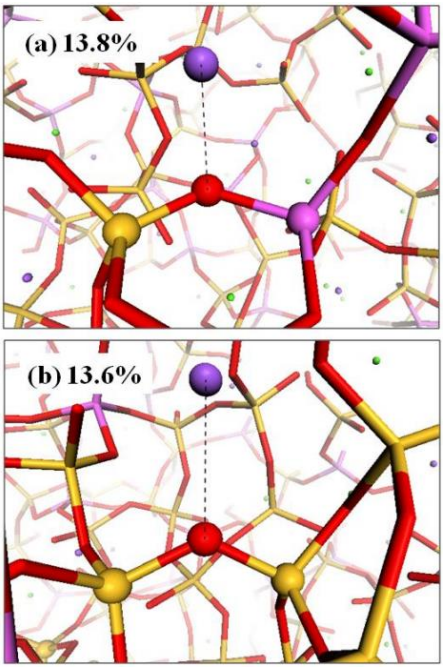

Figure 5.5. The most common bridging oxygen environments in the CNAS glass: (a) Si-BO(1Na)-Si and (b) Si-BO(1Na)-Si sites. Oxygen, sodium and calcium atoms are represented as red, violet and green spheres. Silicon and aluminum atoms are represented as yellow and magenta sticks.

in **Figure 5.4**. Moreover, since the 3QMAS efficiency decreases at lower magnetic fields where the larger C_Q sites (i.e., 5 MHz) are largely suppressed, experiments at low magnetic fields can selectively emphasize the NBO and Al–BO–Al sites with C_Q values of about 2 MHz.

A detailed analysis of the CNAS structural models reveals that, similarly to soda-lime silicate glasses, there is a considerable extent of mixing between Ca and Na around NBOs (13.7% Si–NBO(Ca,Na)). However, in general, the NBOs are not coordinated by Na ions, which instead prefer to compensate the negative charge excess of the Si–O–Al sites (17.1%) or surround Si–BO–Si sites (16%). The geometric configurations of the most populated oxygen sites are depicted in **Figure 5.5**.

5.3. ^{17}O NMR fingerprints of TBOs

TBOs are defined as O atoms bonded to three former cations, T, each of them in a quaternary coordination. They appear in the glass structure when an

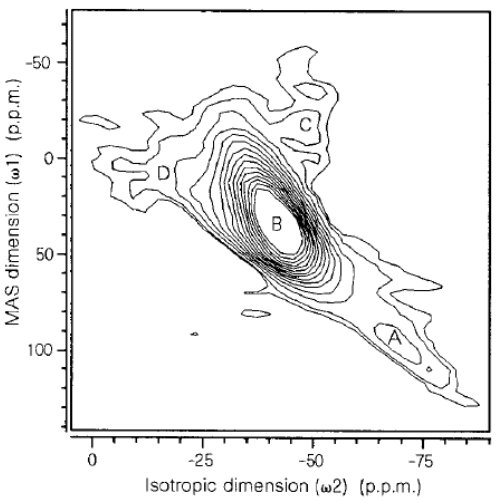

Figure 5.6. ^{17}O MQMAS spectrum of the $25CaO{\cdot}25Al_2O_3{\cdot}50SiO_2$ glass collected by Stebbins and Xu.

excess of NBO with respect to the composition, induces the system to generate TBOs in order to preserve the total amount of T-O bonds. The CAS MD-derived model presents a significant amount of TBOs (4.9 % of total O atoms), so that we considered the relative MD-GIPAW data could be employed for a study of TBOs spectroscopic fingerprints.

In a pioneering experimental work, Stebbins and Xue [4] found that the ^{17}O 3QMAS spectrum of the $25CaO{\cdot}25Al_2O_3{\cdot}50SiO_2$ tectosilicate glass was composed essentially by four peaks denoted as A, B, C and D (**Fig. 5.6**). Peak A was associated to NBO atoms whose δ_{iso} and C_Q were assessed to be 113 ± 2 ppm and 2.9 ± 0.2 MHz, respectively. Peak B, assigned to Si-O-Al bonds, was the main one with δ_{iso}= 61 ppm and C_Q = 3.5 MHz. Peak C (50 ppm, 5.5 MHz) was associated to Si-O-Si bonds. Finally, they detected a small peak, called D, with δ_{iso}= 20 ppm and C_Q = 2.3 MHz that was supposed to be the signal arising from OAl_3 or OAl_2Si TBOs, in which Al remains in four-coordination. To help in the interpretation of the experimental spectrum the simulated ^{17}O 3QMAS NMR spectrum of all the oxygens and of OAl_2Si (1.1%), $OAlSi_2$ (0.6%) and OAl_3 (1.9%) tricluster oxygens is reported in **Figure 5.6**.

(a) (b)

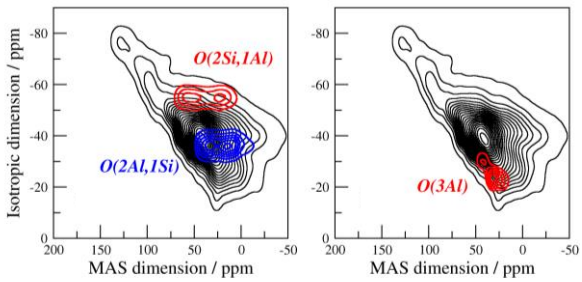

Figure 5.7. Simulated ^{17}O 3QMAS NMR spectrum at 11.75 T of the CAS glass. The Signal of the different TBOs oxygen speciation are superimposed in panels from (a) to (b).

Comparing **Figures 5.6** and **5.7**, we noticed differences between our and Stebbins and Xu's spectrum which are probably due to differences in site populations (Al-O-Al, Si-O-Al, etc…) as a consequence of slightly different compositions.

The comparison of **Figure 5.7.a** and **5.4**, clearly reveal that the NMR parameters of the OAl_2Si (50.1 ppm, 4.66 MHz) and $OAlSi_2$ (77.4 ppm, 5.53 MHz) are in the same range covered by the Si-O-Si and Si-O-Al sites and since these triclusters are present in the glass in very small quantities, it is very unlikely that 3QMAS NMR could detect them. This agrees with previous Car-Parrinello molecular dynamics simulations of calcium aluminosilicate glasses with similar compositions [15]. Conversely, the NMR parameters of the OAl_3 triclusters are close to the edge of the main Si-O-Al peak and their position (**Fig. 5.7.b**) is in nice agreement with the peak D observed by Stebbins and Xu [4].

In the simulated glass structure, the OAl_3 sites are found to be present in five structural motifs. Two of them are depicted in **Figure 5.8**. OAl_3 sites where two of the Al atoms form a 2 membered Al_2O_2 ring (**fig. 5.8.b**) shows the small value of C_Q = 2.4 MHz consistent with the experimental observations of Stebbins and Xue [4]. Therefore, the results obtained seem to support the experimentalist' assignments of the D peak in the 3QMAS spectra to O

triclusters with a local geometry similar to that depicted in **figure 5.8.b,** although it must be noted that the calculated isotropic chemical shift of 40 ppm is much greater than that proposed by Stebbins and Xue [4].

5.4. Correlations between ^{17}O NMR Parameters and Local Geometry

Another interesting feature of NMR computational spectroscopy is the possibility of correlating the computed parameters with the local environment, that is, bond length, angles, and coordination numbers. The finding of accurate and simple quantitative structure–NMR parameter relationships would be immensely useful from both the experimental and computational points of view. In the former case, new insights into the atomic structure of multicomponent glasses could be gained from the extraction of the NMR parameter distributions [16] while, in the latter case, the NMR spectra of different glass structural models containing thousands of atoms could be straightforwardly calculated by skipping time-consuming ab initio calculations. For these reasons, several structural–NMR parameter correlations have been proposed and attempted in the past. The dependence of ^{17}O NMR parameters upon the Si–O–Si bond angle and Si–O bond distance has been extensively studied with ab initio calculations on clusters [17–19] and periodic [20–23] silicate models.

From these papers, a linear correlation between the Si–BO average bond length and the ^{17}O δ_{iso} of BO and a linear correlation between the M–NBO (where M stands for modifier) average bond length and the isotropic chemical

shift of NBOs were obtained, while no correlation was found between the isotropic chemical shift of NBO and the Si–NBO bond lengths [20,22].

Moreover, several relationships have been proposed in order to describe the dependence of the BO quadrupolar coupling constant C_Q and asymmetry parameter η_Q upon the Si–O–Si angle. Commonly used relationships are:

$$C_Q(\theta) = A\left(\frac{1}{2} + \frac{cos\theta}{cos\theta - 1}\right)^{\alpha} + \Delta C_Q \qquad \text{(Eq. 5.1)}$$

$$\eta_Q(\theta) = B\left(\frac{1}{2} + \frac{cos\theta}{cos\theta - 1}\right)^{\beta} + \Delta \eta_Q \qquad \text{(Eq. 5.2)}$$

where θ = <Si–O–Si>. Other analytical forms such as cos θ and θ polynomials were also investigated but did not yield any significant improvement for predicting the NMR parameters. All these correlations have been obtained in vitreous silica and binary silicate glasses.

In **Figure 5.9**, the ^{17}O isotropic chemical shift of BOs and NBOs has been plotted as a function of the average Si–BO, Si–NBO, and M–NBO (M = Na and/or Ca) bond lengths for the NS, CS, and CSN glasses investigated in this work. Moreover, the ^{17}O C_Q, η_Q, and δ_{iso} of BOs plotted as a function of the Si–O–Si bond angles are presented in **Figure 5.10**.

Both figures show poorer correlations with respect to those reported for vitreous silica and binary soda silicate glasses, where a correlation coefficient *R* of about 0.7–0.8 and standard deviations of about 0.15–0.20 MHz for C_Q and 0.1 for η_Q were found [21,24]. In this work, the quadrupolar parameters (C_Q, η_Q) have been fitted by using **Eqs. 5.1** and **5.2**, also providing *R* values in the range 0.7–0.8, but the dispersion of the data is higher, with the standard deviations of about 0.2–0.3 MHz for C_Q and 0.14 for η_Q.

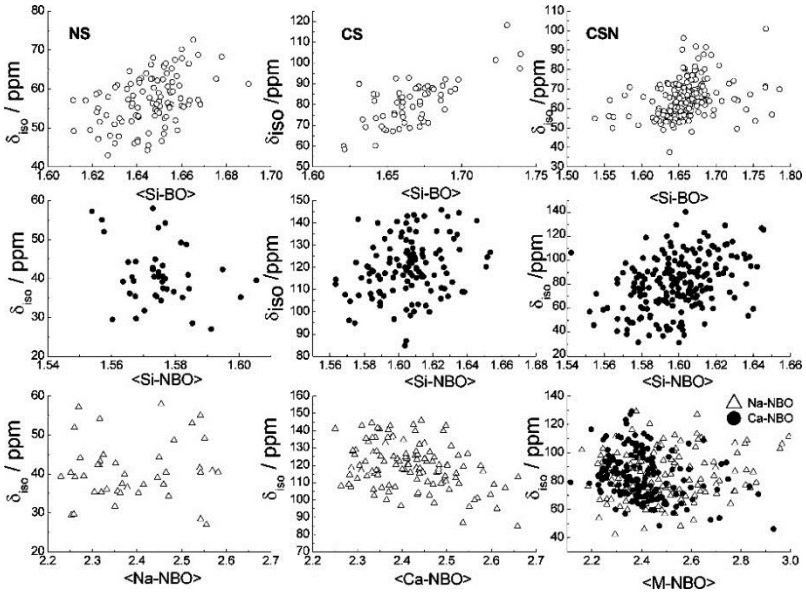

Figure 5.9. The isotropic chemical shift of BO and NBO as a function of the average Si-BO, Si-NBO and M-NBO (M=Na/Ca) for the NS, CS and CSN glasses.

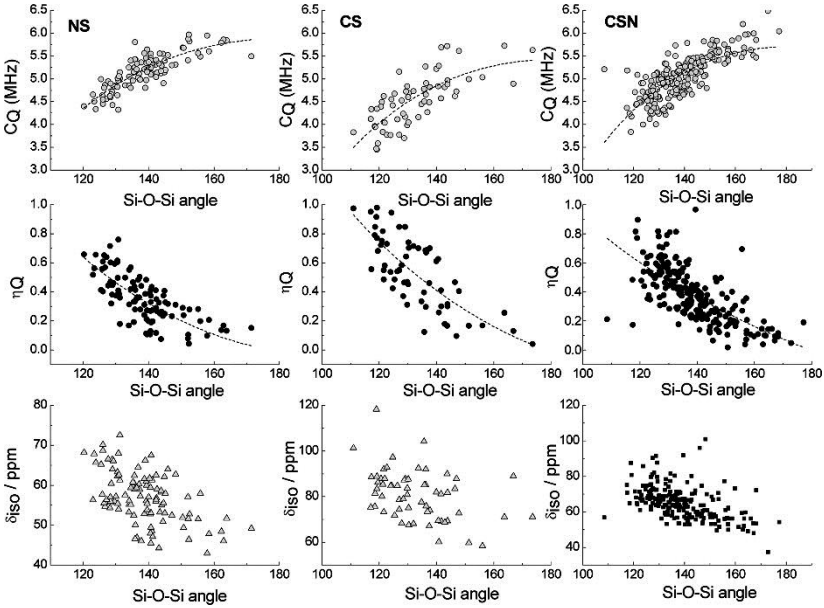

Figure 5.10. The NMR parameters of BOs as a function of the Si-O-Si for the NS, CS and CSN glasses.

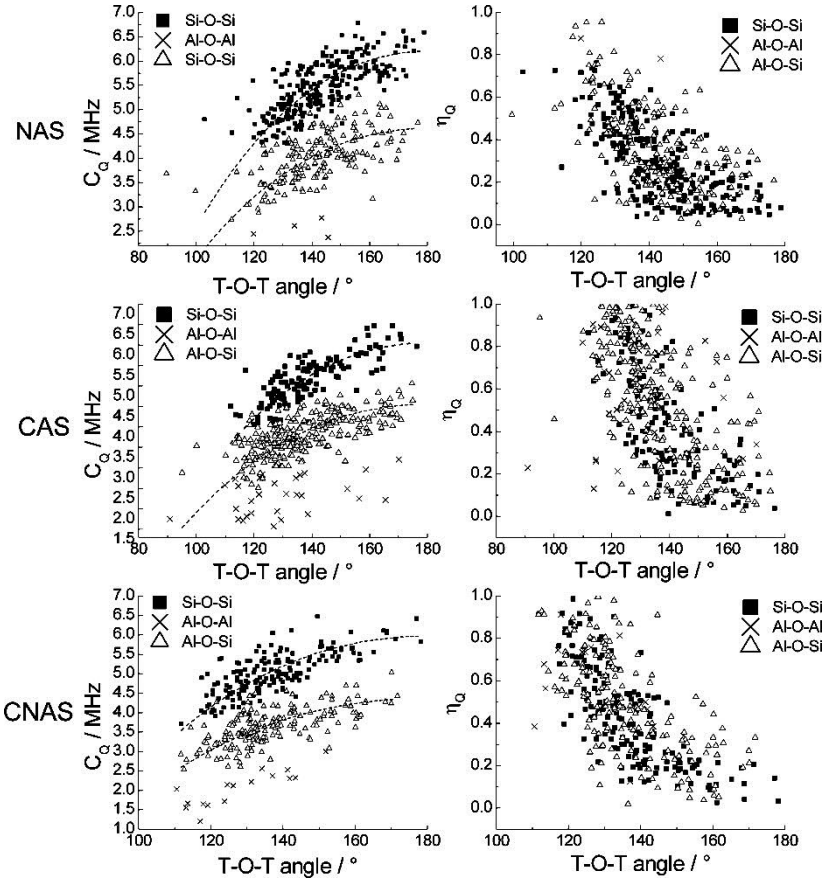

Figure 5.11. The NMR quadrupolar parameters of BO as a function of the Si-O-Si for the NAS, CAS and CNAS glasses.

The isotropic chemical shift was found to be predicted poorly using the short-range information provided by the Si–O–Si angle and Si–O distance; therefore, it seems to be sensitive to variation of structure beyond the first coordination sphere [25].

Similarly, no simple correlations could be found for the isotropic chemical shift and T–O (T = Al/Si) bond lengths of aluminosilicate glasses.

In **Figure 5.11**, the calculated quadrupolar couplings C_Q and asymmetry parameter η_Q are depicted as a function of the T–O–T angle for each O atom. In both cases, it is difficult to extract a clear dependence of quadrupolar parameters on the T–O–T angle even if a rough trend can be detected. The C_Q values tend to increase as a function of the angles and to be larger for the Si–O–Si sites than for the Si–O–Al ones.

The dotted lines represent the best fit obtained by employing **Eqs. 5.1** and **5.2**. However, no correlations have been found for aluminosilicate glasses. It is worth noting that in a previous study very good correlations between the Si–O–Si angle and ^{17}O NMR parameters were obtained [17]. However, according to our results, these correlations appear to be an artifact due to the use of small clusters which are not able to represent the chemical and topological disorder present in multicomponent glasses.

5.5. Final Remarks

The excellent agreement between theoretical and experimental ^{17}O MAS spectra of the NS, CS, NAS, and CAS glasses validated the models and the computational method. This allowed the extension of the study to the analysis of the theoretically derived MAS and 3QMAS NMR spectra in terms of the nature of the non-framework disorder in soda-lime glasses and the extent of framework disorder in aluminosilicate glasses.

The results clearly indicate that there is extensive mixing of Ca and Na around NBOs in soda-lime silicate glasses. In fact, the amount of Si–NBO(Na,Ca) sites, 37.8% of the total oxygen atoms present, is higher than that predicted by employing a random distribution of cations around NBO, whereas the

amount of NBO coordinated to only one of the Na or Ca species (7.2 and 4.6%, respectively) is lower. This peculiar cation distribution leads to an increase in the viscosity of silicate melts over that predicted from a random distribution, as found in literature[7].

TBOs appear in CAS (4.9 %) and NAS models (1.7%). We deduced that higher field strength cations (Ca^{2+} > Na^{+}) promote the formation of NBO and TBO because of the competition for low-coordination states.

Instead, all the NBOs present in the three glasses are associated with Si atoms rather than Al ones.

An investigation on TBOs spectroscopic fingerprints led to confirm that the NMR parameters of the OAl_2Si and $OAlSi_2$ sites fall in the same range covered by those of the Si–O–Si and Si–O–Al sites. Since these triclusters are present in the glass in very small quantities, it is very unlikely that ^{17}O MAS and 3QMAS NMR spectroscopies could detect them. Conversely, the NMR parameters of the OAl_3 where 2 Al are involved in a 2-membered ring fall close to the edge of the main Si–O–Al peak, and their position is found to be in nice agreement with experimental evidence.

Moreover, an extensive mixing of framework units is observed in the CNAS glass, since the amount of Si–O–Al sites is higher than that predicted by a random distribution; also, a considerable extent of mixing between Ca and Na around NBOs is found in this glass, similar to soda-lime silicate glasses.

Finally, simple and accurate relationships between NMR parameters and the local information such as Si–O distances and Si–O–T angles could not be found. Therefore, the generation of structural models of glasses and melts by means of MD simulations and the subsequent DFT/GIPAW calculations of

the ^{17}O NMR parameters remains mandatory for an unambiguous interpretation of very complex multicomponent systems such as those studied in this work.

Bibliography

[1] Lee SK, Stebbins JF. Nature of Cation Mixing and Ordering in Na-Ca Silicate Glasses and Melts. J Phys Chem B 2003;107:3141–8. doi:10.1021/jp027489y.

[2] Lee SK, Stebbins JF. Disorder and the extent of polymerization in calcium silicate and aluminosilicate glasses: O-17 NMR results and quantum chemical molecular orbital calculations. Geochim Cosmochim Acta 2006;70:4275–86. doi:10.1016/j.gca.2006.06.1550.

[3] Lee SK, Stebbins JF. The Structure of Aluminosilicate Glasses: High-Resolution ^{17}O and ^{27}Al MAS and 3QMAS NMR Study. J Phys Chem B 2000;104:4091–100. doi:10.1021/jp994273w.

[4] Stebbins JF, Xu Z. NMR evidence for excess non-bridging oxygen in an aluminosilicate glass. Nature 1997;390:60–2.

[5] Pedone A, Gambuzzi E, Menziani MC. Unambiguous Description of the Oxygen Environment in Multicomponent Aluminosilicate Glasses from ^{17}O Solid State NMR Computational Spectroscopy. J Phys Chem C 2012;116:14599–609. doi:10.1021/jp304802y.

[6] Pedone A, Charpentier T, Malavasi G, Menziani MC. New Insights into the Atomic Structure of 45S5 Bioglass by Means of Solid-State NMR Spectroscopy and Accurate First-Principles Simulations. Chem Mater 2010;22:5644–52. doi:10.1021/cm102089c.

[7] Lee SK. Microscopic origins of macroscopic properties of silicate melts and glasses at ambient and high pressure: Implications for melt generation and dynamics. Geochim Cosmochim Acta 2005;69:3695–710. doi:10.1016/j.gca.2005.03.011.

[8] Park B, Cormack A. Molecular dynamics simulations of structural changes in mixed alkali (Li–K) silicate glasses. J Non-Cryst Solids 1999;255:112–21. doi:10.1016/S0022-3093(99)00430-5.

[9] Pedone A, Malavasi G, Cormack AN, Segre U, Menziani MC. Elastic and dynamical properties of alkali-silicate glasses from computer simulations techniques. Theor Chem Acc 2008;120:557–64. doi:10.1007/s00214-008-0434-7.

[10] Pedone A, Malavasi G, Menziani MC, Segre U, Cormack AN. Role of Magnesium in Soda-Lime Glasses: Insight into Structural, Transport, and Mechanical Properties through Computer Simulations. J Phys Chem C 2008;112:11034–41. doi:10.1021/jp8016776.

[11] Toplis MJ, Dingwell, Donald B., Hess K-W, Lenci T. Viscosity, fragility, and configurational entropy of melts along the join SiO2-NaAlSiO4. Am Min 1997;82:979–90.

[12] Cormack AN, Du J. Molecular dynamics simulations of soda–lime–silicate glasses. J Non-Cryst Solids 2001;293-295:283–9. doi:10.1016/S0022-3093(01)00831-6.

[13] Allwardt JR, Lee SK, Stebbins JF. Bonding preferences of non-bridging O atoms: Evidence from 17O MAS and 3QMAS NMR on calcium aluminate and low-silica Ca-aluminosilicate glasses. Am Min 2003;88:949–54.

[14] Mysen BO, Richet P. Silicate glasses and melts properties and structure. Amsterdam; Boston: Elsevier; 2005.
[15] Tossell JA, Horbach J. O Triclusters Revisited: Classical MD and Quantum Cluster Results for Glasses of Composition (Al_2O_3)2(SiO_2). J Phys Chem B 2005;109:1794–7. doi:10.1021/jp0454873.
[16] Clark T, Grandinetti P, Florian P, Stebbins J. Correlated structural distributions in silica glass. Phys Rev B 2004;70. doi:10.1103/PhysRevB.70.064202.
[17] Xue X, Kanzaki M. Correlations between 29 Si, 17 O and 1 H NMR properties and local structures in silicates: an ab initio calculation. Phys Chem Miner 1998;26:14–30. doi:10.1007/s002690050157.
[18] Clark TM, Grandinetti PJ. Calculation of bridging oxygen quadrupolar coupling parameters in alkali silicates: A combined ab initio investigation. Solid State Nucl Magn Reson 2005;27:233–41. doi:10.1016/j.ssnmr.2005.01.002.
[19] Clark TM, Grandinetti PJ. Dependence of bridging oxygen ^{17}O quadrupolar coupling parameters on Si–O distance and Si–O–Si angle. J Phys Condens Matter 2003;15:S2387–95. doi:10.1088/0953-8984/15/31/314.
[20] Benoit M, Profeta M, Mauri F, Pickard CJ, Tuckerman ME. First-Principles Calculation of the ^{17}O NMR Parameters of a Calcium Aluminosilicate Glass. J Phys Chem B 2005;109:6052–60. doi:10.1021/jp0492570.
[21] Charpentier T, Kroll P, Mauri F. First-Principles Nuclear Magnetic Resonance Structural Analysis of Vitreous Silica. J Phys Chem C 2009;113:7917–29. doi:10.1021/jp900297r.
[22] Angeli F, Villain O, Schuller S, Ispas S, Charpentier T. Insight into sodium silicate glass structural organization by multinuclear NMR combined with first-principles calculations. Geochim Cosmochim Acta 2011;75:2453–69. doi:10.1016/j.gca.2011.02.003.
[23] Ispas S, Charpentier T, Mauri F, Neuville DR. Structural properties of lithium and sodium tetrasilicate glasses: Molecular dynamics simulations versus NMR experimental and first-principles data. Solid State Sci 2010;12:183–92. doi:10.1016/j.solidstatesciences.2009.06.033.
[24] Charpentier T, Ispas S, Profeta M, Mauri F, Pickard CJ. First-Principles Calculation of ^{17}O, ^{29}Si, and ^{23}Na NMR Spectra of Sodium Silicate Crystals and Glasses. J Phys Chem B 2004;108:4147–61. doi:10.1021/jp0367225.
[25] Pedone A, Biczysko M, Barone V. Environmental Effects in Computational Spectroscopy: Accuracy and Interpretation. ChemPhysChem 2010:NA – NA. doi:10.1002/cphc.200900976.

CHAPTER 6

^{23}Na 3QMAS NMR spectroscopy: sodium environment in silicate and aluminosilicate glasses

Sodium environment in two Na,Ca-containing glass samples, CSN ($60SiO_2 \cdot 20CaO \cdot 20Na_2O$) and CASN ($60SiO_2 \cdot 10Al_2O_3 \cdot 20CaO \cdot 10Na_2O$) was investigated. ^{23}Na 3QMAS spectra were collected and compared with NMR theoretical data obtained on MD-derived structural models. These glasses were chosen because Na plays two different role in the structure: it acts prevalently as a modifier in CASN and as a charge compensator in CSN.

The two essential aspects that can be studied with ^{23}Na NMR are: (i) the local Na first coordination sphere such as the Na–O coordination number (CN), bridging oxygens (BO) and non-bridging oxygens (NBO), and (ii) the Na second coordination sphere, i.e. the environments beyond the coordinating O atoms. For example, the ratio of BOs and NBOs coordinated to the Na^+ ions reflects its role, such as the network modifier (preferentially surrounded by NBOs) vs the charge compensator (preferentially surrounded by BOs).

In the work presented hereafter, the synergetic computational-experimental approach was exploited at its best possibilities, thanks to very reliable sets of experimental NMR parameters for both CSN and CASN compositions. Compared to the work published by Angeli at al. [1] on these same compositions, ^{23}Na 3QMAS were collected with an improved pulse sequence that gave a significantly increased signal/noise ratio. Better quality data allowed a more in-depth interpretation of Na environment, even because the

subsequent fitting procedure was improved respect to the past [1]. The results were published in ref. [2].

6.1. ^{23}Na 3QMAS spectra collection and fitting procedure

The ^{23}Na 3QMAS spectra were collected on a Bruker Avance II 500WB spectrometer at a magnetic field of 11.7 T. No isotopic enrichment was needed, as the quadrupolar NMR-active Sodium-23 isotope (nuclear spin, I = 3/2) is the only stable one among those of Na, thus having a 100% natural abundance. The sample spinning frequency of 14 kHz under the application of a radio frequency of about 160 kHz. A two-pulse MQMAS sequence [3] with optimized excitation and reconversion pulses of p_1 = 4 μs and $p_2 = \tau_{rot}/4$ μs (where τ_{rot} is the MAS rotor period) was used to acquire the MQMAS spectra. As shown in Supplementary Information of ref. [2], this pulse sequence shows a more homogeneous excitation profile with respect to the quadrupolar coupling constant, C_Q, when compared to the standard Z-filter pulse sequence [4]. More details on glass synthesis procedures, nominal and actual glass compositions are provided in ref. [1].

^{23}Na 3QMAS spectra were processed by an in-house developed code using an inversion method [5] which can be summarized as follows. For crystalline sample and under MAS, each environment is characterized by three NMR parameters: the quadrupolar coupling constant (C_Q) and asymmetry parameter (η_Q) – both characterizing the local electric field gradient (EFG) – and the isotropic chemical shift (δ_{iso}). On the other hand, disordered systems under MAS are characterized by a multiplicity of sites that result in a distribution of NMR parameters, $p(C_Q, \eta_Q, \delta_{iso})$. The aim of the inversion

method is to reconstruct this distribution. This method is based on a pure numerical procedure so that no assumptions on the NMR parameters distribution shape has to be made, thus overcoming some limitations of the fitting procedure such as the choice of analytical forms. For instance, a popular constrained approach is to use the Gaussian isotropic model (GIM) [6] for the EFG parameters distribution and a Gaussian model for the isotropic chemical shift [5,7].

In this work, the identification of different chemical environments (i.e. different coordination numbers) relies on both the capability of the NMR experiments to reveal the asymmetrical lineshape of the δ_{iso} distribution (see Supplementary Information of ref. [2]) and the data determination through the inversion method. However, since the 2D ^{23}Na MQMAS spectra reveal featureless signal (i.e. smooth lines without well-defined singularities), $p(C_Q, \eta_Q, \delta_{iso})$ – a three-dimensional distribution – they cannot be easily reconstructed numerically. As previously demonstrated with MD simulations [5,7], an analytical model (**Eq. 6.1**) can be used to determine η_Q, which in turn has a very limited effects on the extracted two-dimensional distribution $\Pi(C_Q, \delta_{iso})$. Excellent results have been obtained using the marginal distribution of the GIM model (**Eq. 6.1**) to compute the η_Q distribution, $q(\eta_Q)$:

$$q(\eta) = 3\eta\left(1-\frac{\eta^2}{9}\right)\left(1+\frac{\eta^2}{3}\right)^{-\frac{5}{2}} \qquad (6.1)$$

The $q(\eta_Q)$ distribution obtained with **Eq. 6.1** is similar to those obtained with DFT calculations, after a smoothing using the Kernel Density Estimation (KDE) approach of the CASN and CSN models, as shown in **Figure 6.1**.

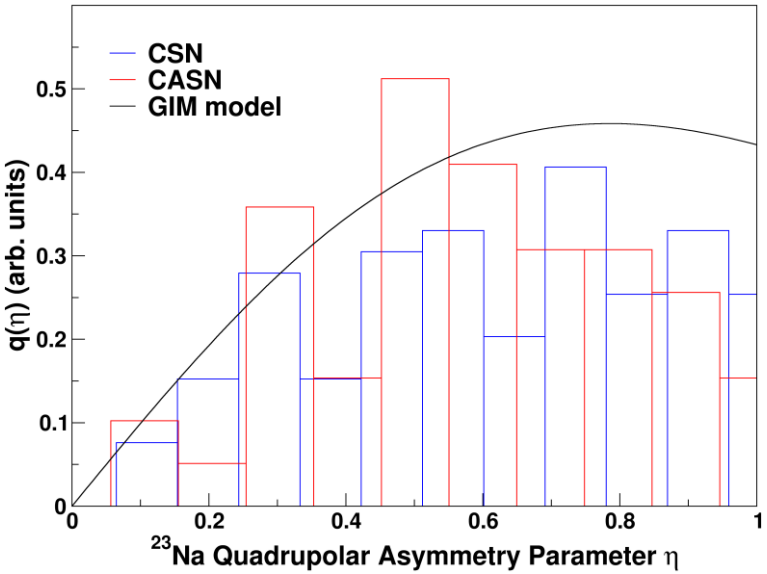

Figure 6.1. η_Q distribution calculated with the GIM model (solid line, Eq. 6.1) compared to η_Q distributions obtained with DFT-KDE calculations on CASN and CSN models (histograms).

Using **Eq. 6.1** the NMR parameter distribution, $p(C_Q, \eta_Q, \delta_{iso})$, is then given by:

$$p(C_Q, \eta, \delta_{iso}) = \Pi(C_Q, \delta_{iso}) \times q(\eta) \quad (6.2)$$

where $\Pi(C_Q, \delta_{iso})$ is reconstructed numerically using a Tikhonov regularization scheme [7] and [8], i.e. by minimizing the quantity:

$$L = \frac{1}{2}\chi^2 + \lambda \left\| D^{(1)} q \right\| \quad (6.3)$$

for a positive distribution Π; χ^2 is the sum of squared errors, and λ is a coefficient that regulates the term $D^{(1)}$ which minimizes the first-order derivative of Π and ensures its smoothness. λ is chosen manually to obtain the best agreement with the experimental data with a smooth (monomodal) distribution.

6.2. Validation of the MD-derived structural models

The validation of the MD-derived structural models for Na has been carried out by comparing the distribution of C_Q and δ_{iso} NMR parameters $\Pi(C_Q, \delta_{iso})$ extracted by the inversion method to which we will refer as *experimental* data (**Figure 6.2**, left panels), and their *theoretical* counterparts (**Figure 6.2**, right panels), i.e. calculated with DFT-GIPAW. The comparison between the experimental and theoretical $\Pi(C_Q, \delta_{iso})$ distributions for CSN and CASN is reported in **Figure 6.1.b** and **6.2.d**, respectively. It can be observed that the shape of $\Pi(C_Q, \delta_{iso})$ is well reproduced, but with the theoretical distribution (+ symbols in **Figure 6.2**) shifted by about +2 MHz with respect to the experimental one (see also **Table 6.1**).

The systematic overestimation of the ^{23}Na C_Q values by our static DFT calculations can be ascribed to the coupling between EFG of the Na^+ with its vibrational modes. This thermal averaging effect cannot be described by our static DFT calculations, as also noticed in a previous computational–experimental work [9]. Such vibrational effects appear to be negligible for network formers (i.e. Si, P and Al) and heavy modifier ions (i.e. Ca), in contrast to the highly mobile Na^+ ions. However, this systematic overestimation can be simply corrected by multiplying the theoretical C_Q^{theo} values for a scaling factor of 0.47.

The theoretical $p(C_Q, \eta_Q, \delta_{iso})$ of the CSN and CASN glasses with scaled C_Q values, reported as full circles in panels **b** and **d** of **Figure 6.2**, are in very good agreement with the experimental ones. It is worth to note that the application of a single scaling factor implies that this vibrational effect is homogeneous. The reliability of this assumption should be further

investigated by going beyond the static approach. However, for the purposes of the present investigation, the scaled C_Q^{theo} values can be employed in the fitting of experimental spectra for the quantification of the different Na sites.

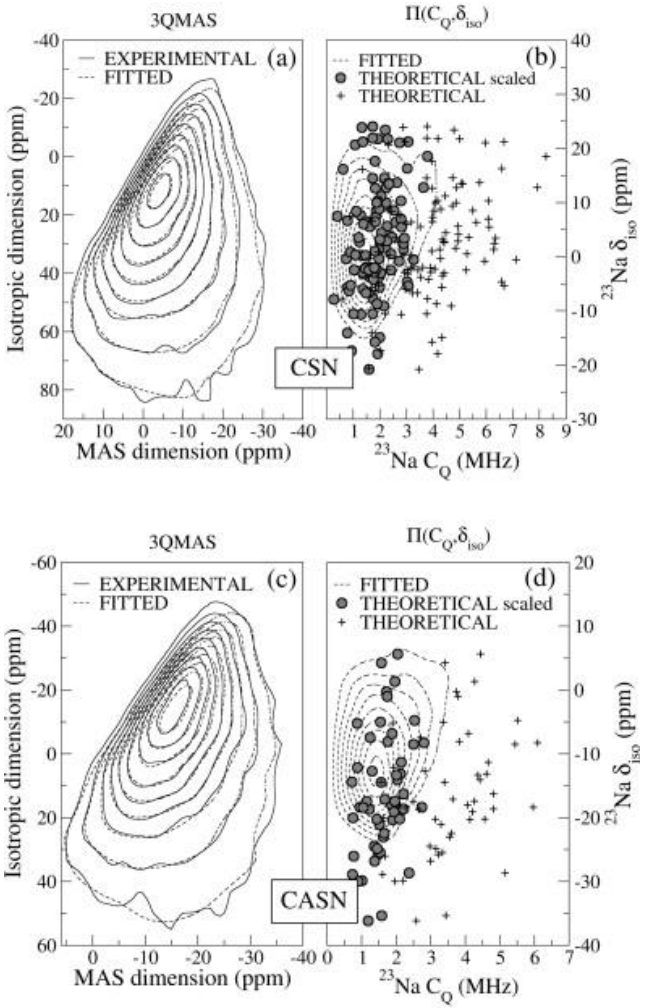

Figure 6.2 ^{23}Na 3QMAS experimental spectra of CSN (a) and CASN (c) glasses (solid lines) and simulated spectra via fitting procedure (dashed lines); $\Pi(C_Q, \delta_{iso})$ distributions of CSN (b) and CASN (d) glasses: fitted from experiment (dashed lines) and theoretical counterparts derived from DFT calculations on MD derived models (dots).

Table 6.1. Experimental (exp) and theoretical (theo) NMR δ_{iso} and C_Q parameters, and average experimental ($\overline{CN}_{EXP}$) and MD-derived coordination numbers ($\overline{CN}_{MD}$).

Glass	$\bar{\delta}_{iso}^{exp}$ (± 2 ppm)	$\bar{\delta}_{iso}^{theo}$ [ppm]	$\bar{C}_Q^{exp}$ (± 1.0 MHz)	$\bar{C}_Q^{theo}$ [MHz]	$\overline{CN}_{EXP}$ (a)	$\overline{CN}_{MD}$ (b)	<Na-O> [Å]
CSN	4.7	3.3	1.9	4.0	5.5	5.6	2.56
CASN	-6.9	-1.1	1.8	3.9	---	5.9	2.55

(a) Result of weighted average of NaO_n population outcoming from fitting 3QMAS spectra with DFT-GIPAW constraints, calculated for CSN only.

(b) Obtained from statistical analysis of MD-derived models; the Na-O cut-off is 3.2 Å.

Concerning the δ_{iso} distributions, the data values listed in **Table 6.1** show a very good agreement between theoretical and experimental counterparts for the CSN glass and an acceptable discrepancy for the CASN glass.

6.3. Relationships between ^{23}Na NMR parameters and Na^+ local environment

Table 6.2 lists the average values of the computed δ_{iso} ($\bar{\delta}_{iso}^{theo}$) and C_Q ($\bar{C}_Q^{theo}$) parameters of Na cations as a function of their coordination numbers, CNs. By considering only NaO_n sites with a relative population higher than 5%, no correlations between $\bar{\delta}_{iso}^{theo}$ and CN are observed, in agreement with the computational results obtained by Koller et al. [10] on small clusters. Correlations between ^{23}Na NMR parameters and Na CN were instead observed in several works on crystalline compounds [11–15], where it was found that both δ_{iso} and C_Q generally decrease when CN increases.

Notwithstanding a qualitative inverse trend between the $\bar{C}_Q^{theo}$ of NaO_n species and CN is showed in **Table 6.2**, the distribution of C_Q as a function of the CN plotted in **Figure 6.3.a** discourages the employment of a regression

equation to estimate the average CN of Na starting from experimental C_Q values in amorphous systems.

Table 6.2. Coordination numbers (CNs), NMR parameters and average <Na-O> distances.

	CSN					CASN			
CN	Pop,MD %	Pop,EXP %	$\bar{\delta}_{iso}^{theo}$ [ppm]	$\bar{C}_Q^{theo}$ [MHz]	<Na-O> [Å]	Pop,MD %	$\bar{\delta}_{iso}^{theo}$ [ppm]	$\bar{C}_Q^{theo}$ [MHz]	<Na-O> [Å]
3	0.0%	---	---	---	---	2.0	-9.0	5.2	2.35
4	7.4%	---	3.5	4.8	2.40	5.9	0.2	5.3	2.42
5	34.3%	60.3	6.9	4.5	2.49	37.3	0.1	4.2	2.51
6	33.3%	30.4	2.7	3.7	2.58	35.3	0.7	4.1	2.56
7	20.4%	9.3	0.0	3.5	2.65	13.7	-4.5	3.3	2.65
8	4.6%	---	-7.4	4.0	2.76	5.9	-10.4	3.0	2.68

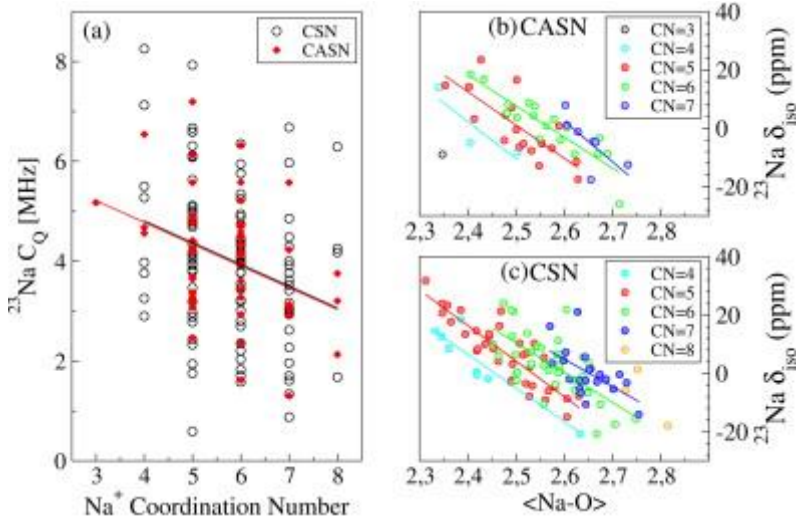

Figure 6.3. Variation of ^{23}Na NMR parameters as a function of some short-range structural features: (a) ^{23}Na C_Q vs Na^+ CN in CSN and CASN, trend lines are reported for visual guide; ^{23}Na δ_{iso} vs average Na-O distance, <Na-O>, for CASN (b) and CSN (c), where Na atoms are differentiated with respect to their CN.

In agreement with the results of the experimental work of Antonijevic et al. [11], and with other DFT investigations, [10] and [9], a dependence of ^{23}Na δ_{iso} on average Na-O distance, denoted $\langle$Na–O$\rangle$, is observed in **Table 6.2**. Here, the MD-GIPAW approach on amorphous systems furnishes further important information: the ^{23}Na δ_{iso} correlates better with <Na-O> when CN is expressly taken into account, as shown in **Figure 6.3.b** for CSN, and in **Figure 6.3.c** for CASN. It is also worth noticing that: (i) the ^{23}Na δ_{iso} regions are strongly overlapped, (ii) for all CNs the linear regressions exhibit a similar slope independently on the composition, and (iii) the intercepts on the ordinate axis (^{23}Na δ_{iso}) increase with CN, preventing the possibility of finding a unique correlation for the overall data set. Conversely, no correlation is observed between ^{23}Na C_Q and $\langle$Na–O$\rangle$, even when the CN is explicitly taken into account. These results imply that the Na average coordination number, $\overline{\mathrm{CN}}$, in amorphous systems is not accurately and directly computable from the experimental NMR parameters ($\bar{\delta}_{\mathrm{iso}}^{\mathrm{exp}}$ and $\bar{\mathrm{C}}_{\mathrm{Q}}^{\mathrm{exp}}$) reported in **Table 6.1**. However, the average NMR parameters computed through the MD-GIPAW approach, $\bar{\delta}_{\mathrm{iso}}^{\mathrm{theo}}$ and $\bar{\mathrm{C}}_{\mathrm{Q}}^{\mathrm{theo}}$, of NaO_n species can be used to constraint the fitting of the ^{23}Na 3QMAS spectra, leading to the quantification of each NaO_n species in the glasses.

The distribution of the CN of Na cations in the CSN and CASN glasses have been obtained by re-fitting their experimental spectra by assuming that different NaO_n sites contribute to the total spectra. During the spectral fitting of the CSN glass, the C_Q values of the most populated NaO_n sites (n = 5, 6, 7) found in the MD models were constrained to be close to the corresponding theoretical values scaled by 0.47. Instead, the NaO_n populations in the CASN glass have not been re-fitted, since the theoretical constraints were

computed on small amount of Na atoms, which was considered not reliable for the accuracy level we wanted to achieve.

Table 6.2 shows that in the CSN glass the majority of Na^+ ions is 5-coordinated (60.3%) and 6-coordinated (30.4%), while a minority (9.3%) is 7-coordinated. This distribution agrees with experimental findings on alkali and alkaline extra-framework cations in glasses, [11] and [16].

By performing a weighted average of the above-mentioned data, the experimental average CN of Na in CSN glass, $\overline{\mathrm{CN}}_{\mathrm{EXP}}$, has been determined. The MD derived and experimental $\overline{\mathrm{CN}}$ for CSN (**Table 6.2**) are 5.6 and 5.5, respectively. These values are in very good agreement, confirming again the validity of the structural model of the CSN glass and the consistency of the procedure adopted. As for the CASN glass, the slightly higher data value of $\overline{\mathrm{CN}}_{\mathrm{MD}}$ 5.9 found with respect to the CSN glass is in agreement with the slightly lower value of C_Q extracted from the experiments. In fact, the theoretical calculations show that C_Q decreases with the increase of the CN (**Figure 6.3.a**). Finally, **Table 6.2** shows that the Na–O bond lengths, computed by averaging all the Na–O distances found within a cut-off of 3.2 Å [17], are 0.1–0.2 Å longer than the ones usually obtained from NMR and EXAFS experiments (2.3–2.4 Å) [5,18–20]. This is due to the approach in which the data have been computed. In fact, by extracting the Na–O distances from the maximum of the corresponding pair distribution functions generated via MD simulations the values of 2.36 and 2.35 Å for CSN and CASN, respectively are obtained.

6.4. Local and medium-range environment: determination of the role of Na^+

The investigation of the first coordination shell around the Na ions in terms of the relative population of bridging oxygens (BOs) and non-bridging oxygens (NBOs) can provide useful information on the structural role played by the Na^+ ions.

Charge compensator ions are located in polymerized region close to network tetrahedral bearing a negative charge such as in $(AlO_{4/2})^-$ units, whereas modifiers are located inside channels delimited by NBOs. It is then reasonable to assume that a pure charge compensator is coordinated mostly by BOs, while a pure network modifier by NBOs. Therefore, a classification of the nature of Na role can be given by the ratio between the number of BOs and the number of total O, $R = n°BOs/CN$, which ranges between 0 and 1.

The greater the population of Na^+ ions with R values close to 1, the more charge compensating is the Na attitude in the glass. **Figure 6.4** shows the distribution of *R* values for Na atoms and **Figure 6.5** shows the typical Na

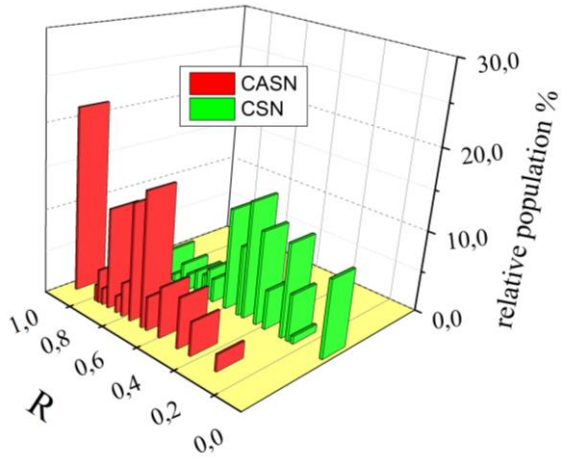

Figure 6.4. Relative percentage populations of Na sites characterized by the same ratio $R = n°BOs/CN$ calculated with respect to the total amount of Na in the CSN and CASN MD-models.

environment in the CSN (**Figure 6.5.a**) and CASN (**Figure 6.5.b**) glasses. The presence of a not negligible population of Na^+ characterized by $R \geq 0.5$ in the CSN glass is ascribable to the simultaneous presence of Ca^{2+} ions. In fact, as also stated in **Chapters 3, 4** and **5**, glasses containing both Ca^{2+} and Na^+ showed that Na^+ tends to coordinate oxygens belonging to glass regions with a lower charge concentration, i.e.: more polymerized regions. Indeed, when Ca^{2+} is present in the glass, it prefers to be coordinated by NBOs and pushes Na^+ in more polymerized domains, conferring it a more compensator character.

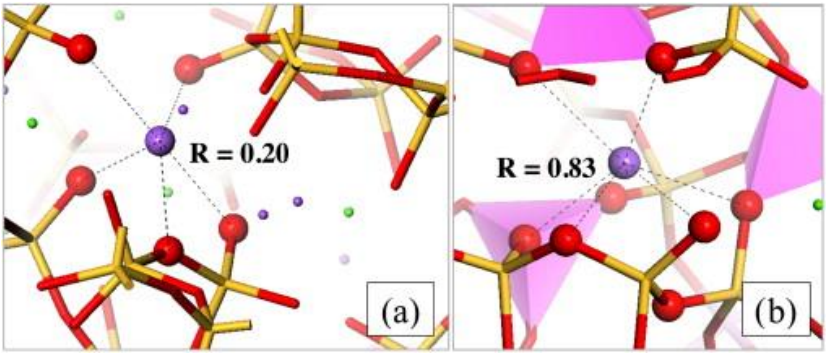

Figure 6.5. Typical Na (violet spheres) environment in CSN (a) and CASN (b). Red spheres are Oxygen atoms coordinating Na in a cut-off of 3.2 Å; yellow sticks are Silicon atoms and green spheres are Calcium atoms.

6.5. Final remarks

The relationships between the ^{23}Na NMR parameters and the Na local structural features such as CNs and average Na–O distances have been investigated by using classical MD simulations and DFT-GIPAW calculations. With respect to previous studies on crystalline samples, the results presented in this work provide a richer statistics of Na environment.

A linear correlation between ^{23}Na δ_{iso} and <Na–O> is observed when different CNs are taken into account. The slope of the linear trends is similar for all NaO_n sites and does not depend on glass composition; the intercept increases with CN but the overlapped signals among the ^{23}Na δ_{iso} regions of different NaO_n sites preclude any unambiguous correlation between ^{23}Na δ_{iso} and CN. Instead, no correlations have been found between ^{23}Na NMR parameters and the local structural features of Na sites.

We have shown that, due to the variability of ^{23}Na NMR parameters of different NaO_n sites, the direct observation of the average CN of Na ions from the experimentally fitted ^{23}Na $\bar{\delta}_{\mathrm{iso}}^{\mathrm{exp}}$ and $\bar{C}_{\mathrm{Q}}^{\mathrm{exp}}$ parameters is not possible in amorphous systems.

Nevertheless, by constraining the fitting of experimental ^{23}Na 3QMAS spectra with the theoretical NMR values found for the different NaO_n sites, we have been able to estimate the experimental distribution of these sites and the average coordination number of Na ions in CSN glass which is 5.5, very close to the one provided by the MD model (5.6).

The environment in the first coordination sphere, expressed in terms of amount of oxygen atoms, is similar for both silicate and aluminosilicate glasses; on the other hand, the speciation of these O atoms in BOs and NBOs confirms previous hypotheses that see Na^+ playing a charge compensator role in CASN and a network modifier role in CSN.

Bibliography

[1] Angeli F, Gaillard M, Jollivet P, Charpentier T. Contribution of 43Ca MAS NMR for probing the structural configuration of calcium in glass. Chem Phys Lett 2007;440:324–8. doi:10.1016/j.cplett.2007.04.036.

[2] Gambuzzi E, Charpentier T, Menziani MC, Pedone A. Computational interpretation of 23Na MQMAS NMR spectra: A comprehensive investigation of the Na environment in silicate glasses. Chem Phys Lett 2014;612:56–61. doi:10.1016/j.cplett.2014.08.004.

[3] Wu G, Rovnyak D, Griffin RG. Quantitative Multiple-Quantum Magic-Angle-Spinning NMR Spectroscopy of Quadrupolar Nuclei in Solids. J Am Chem Soc 1996;118:9326–32. doi:10.1021/ja9614676.
[4] Amoureux J-P, Fernandez C, Steuernagel S. ZFiltering in MQMAS NMR. J Magn Reson A 1996;123:116–8. doi:10.1006/jmra.1996.0221.
[5] Angeli F, Delaye J-M, Charpentier T, Petit J-C, Ghaleb D, Faucon P. Influence of glass chemical composition on the Na–O bond distance: a 23Na 3Q-MAS NMR and molecular dynamics study. J Non-Cryst Solids 2000;276:132–44. doi:10.1016/S0022-3093(00)00259-3.
[6] Bureau B, Silly G, Buzaré J., Legein C, Massiot D. From crystalline to glassy gallium fluoride materials: an NMR study of and quadrupolar nuclei. Solid State Nucl Magn Reson 1999;14:181–90. doi:10.1016/S0926-2040(99)00027-2.
[7] Angeli F, Charpentier T, Faucon P, Petit J-C. Structural Characterization of Glass from the Inversion of ^{23} Na and ^{27} Al 3Q-MAS NMR Spectra. J Phys Chem B 1999;103:10356–64. doi:10.1021/jp9910035.
[8] Tikhonov AN, Arsenin VY. Solution of III-Posed Problems. Washington DC: Winston/Wiley; 1997.
[9] Angeli F, Villain O, Schuller S, Ispas S, Charpentier T. Insight into sodium silicate glass structural organization by multinuclear NMR combined with first-principles calculations. Geochim Cosmochim Acta 2011;75:2453–69. doi:10.1016/j.gca.2011.02.003.
[10] Koller H, Engelhardt G, Kentgens APM, Sauer J. 23Na NMR Spectroscopy of Solids: Interpretation of Quadrupole Interaction Parameters and Chemical Shifts. J Phys Chem 1994;98:1544–51. doi:10.1021/j100057a004.
[11] Antonijevic S, Ashbrook SE, Walton RI, Wimperis S. A multiple-quantum 23Na MAS NMR study of amorphous sodium gallium silicate zeolite precursors. J Mater Chem 2002;12:1469–74. doi:10.1039/b201581c.
[12] Dec SF, Maciel GE, Fitzgerald JJ. Solid-state sodium-23 and aluminum-27 MAS NMR study of the dehydration of sodium aluminate hydrate (Na2O.cntdot.Al2O3.cntdot.3H2O). J Am Chem Soc 1990;112:9069–77. doi:10.1021/ja00181a006.
[13] Dirken PJ, Jansen JBH, Shuiling RD. Influence of octahedral polymerization on 23Na and 27Al MAS NMR in alkali fluoroaluminates. Am Min 1992;77:718–24.
[14] Heidemann D, Hübert C, Schwieger W, Grabner P, Bergk K-H, Sarv P. 29Si- und23Na-Festkürper-MAS-NMR-Untersuchungen an Modifikationen des Na2Si2O5. Z Für Anorg Allg Chem 1992;617:169–77. doi:10.1002/zaac.19926170129.
[15] Wong A, Wu G. Solid-State ^{23} Na Nuclear Magnetic Resonance of Sodium Complexes with Crown Ethers, Cryptands, and Naturally Occurring Antibiotic Ionophores: A Direct Probe to the Sodium-Binding Sites. J Phys Chem A 2000;104:11844–52. doi:10.1021/jp002096p.
[16] Pedone A, Charpentier T, Menziani MC. Multinuclear NMR of CaSiO3 glass: simulation from first-principles. Phys Chem Chem Phys 2010;12:6054–66. doi:10.1039/b924489a.
[17] Malavasi G, Menziani MC, Pedone A, Civalleri B, Corno M, Ugliengo P. A computational multiscale strategy to the study of amorphous materials. Theor Chem Acc 2007;117:933–42. doi:10.1007/s00214-006-0214-1.
[18] Greaves GN. Exafs for studying corrosion of glass surfaces. J Non-Cryst Solids 1990;120:108–16. doi:10.1016/0022-3093(90)90196-S.
[19] Greaves GN, Fontaine A, Lagarde P, Raoux D, Gurman SJ. Local structure of silicate glasses. Nature 1981;293:611–6. doi:10.1038/293611a0.

[20] McGrail BP, Icenhower JP, Shuh DK, Liu P, Darab JG, Baer DR, et al. The structure of Na2O–Al2O3–SiO2 glass: impact on sodium ion exchange in H2O and D2O. J Non-Cryst Solids 2001;296:10–26. doi:10.1016/S0022-3093(01)00890-0.

CHAPTER 7

^{43}Ca NMR spectroscopy: Ca environment in silicate and aluminosilicate glasses

^{43}Ca 3QMAS and MAS spectra were collected for three Na,Ca-containing glass samples, CAS ($60SiO_2{\cdot}20Al_2O_3{\cdot}20CaO$), CSN ($60SiO_2{\cdot}20CaO{\cdot}20Na_2O$) and CASN ($60SiO_2{\cdot}10Al_2O_3{\cdot}20CaO{\cdot}10Na_2O$). Inside these systems, Ca^{2+} ions play different structural roles: when network modifier, Ca ions disrupt two Si-O-Si bonds by forming two non-bridging oxygens (NBOs) leading to a less polymerized glass network and favouring the dissolution of the glass in water solution. On the contrary, when charge compensator, Ca ions locally compensate negative charge of the $[AlO_4]^-$ units, and its reduced mobility disfavours its dissolution in water[1]. In the compositions under study, Calcium acts as a charge compensator of $[AlO_4]^-$ units in the CAS glass, as a modifier in the CSN glass and in both ways in the CASN glass.

In this chapter, the first ^{43}Ca 3QMAS NMR experiments of the aforementioned samples are presented. An inversion fitting procedure, as described in **Chapter 6**, allowed to obtain accurate *experimental* sets of NMR parameters. These were compared to their *theoretical* counterparts obtained with the MD-GIPAW calculations.

By coupling ^{43}Ca 3QMAS experiments, inversion procedure, and NMR-GIPAW calculations on sound MD-derived structural models of the glasses, we have been able to shed light on *i)* Ca short-range environment in terms of

CN distribution and *ii)* the dependence of ^{43}Ca δ_{iso} on Ca-O as a function of Ca CN improving our understanding of Ca environments in glasses.

7.1. History of the challenging ^{43}Ca NMR spectroscopy

The first ^{43}Ca NMR experiments started to appear from the late 90es [2–5] and demonstrated the correlation between ^{43}Ca NMR parameters and Ca environment. ^{43}Ca solid state NMR is intrinsically difficult because ^{43}Ca is a quadrupolar nucleus (spin = 7/2) with a very low natural abundance (0.135%) and a small gyromagnetic ratio (γ). Thus it presents a very low NMR sensitivity with respect to other common, more abundant and high-γ nuclei, such as ^{23}Na [6,7] or ^{27}Al [8,9]. To increase the signal to noise ratio, experiments at high magnetic fields with long acquisition times and/or isotope enrichment of samples are required; hence, the investigation of Ca environment is difficult and expensive [10]. The combination of these factors results in a very limited number of NMR reports for the ^{43}Ca nucleus. So far, our knowledge about ^{43}Ca NMR experiments on silica-based glass samples is limited to two scientific works [10,11].

Shimoda et al. [11] reported very high-field ^{43}Ca MAS and 3Q/5Q/7QMAS NMR spectra of $CaSiO_3$, $CaMgSi_2O_6$ and $CaAl_2Si_2O_8$ with the aim to characterize Ca coordination number (CN). They distinguished three peaks in the 5Q and 7QMAS spectra and assigned them to three distinct Ca sites coordinated by 6, 7 and 8 oxygen atoms, with the latter two being the dominating CNs. From their analysis, calcium CN apparently increased from 7.1 in $CaSiO_3$ to 7.8 in $CaAl_2Si_2O_8$. However, the low sensitivity associated to the manipulation of high quantum transitions implies that they could have

mis-interpreted the 5Q and 7Q data, obtaining wrong distribution of coordination numbers. In fact, in a recent paper, Pedone et al. have demonstrated, through NMR computational spectroscopy, that a Ca coordination environment ranging from 5 to 8 CN well reproduced both the MAS and MQMAS spectra of $CaSiO_3$ glass [12].

The sensitivity of ^{43}Ca NMR parameters toward the structural role played by Ca in silica and aluminosilicate glasses (the same samples studied by us) was investigated by Angeli et al. [2] The ^{43}Ca MAS spectra were collected at a magnetic field of 11.7 T and analysed by using the Gaussian Isotropic Model (GIM) for quadrupolar NMR parameters distribution [13].

It was found that the transition from a charge-compensating role to network-modifying role results in an increase of both the isotropic chemical shift and the quadrupolar coupling constant of ^{43}Ca. For the CASN glass, the intermediate values of the NMR parameters suggest that calcium is probably in both types of environments. However, the CASN MAS spectrum could not be satisfactorily simulated using a combination of the spectra associated to CAS and CSN environment. It was concluded that MQMAS experiments were needed to get more information.

7.2. ^{43}Ca 3QMAS spectra collection

Compared to previous MAS data collected by Angeli et al. [2] at a magnetic field of 11.75 T, here ^{43}Ca MAS and 3QMAS NMR data were acquired on a Bruker 750MHz spectrometer, operating at a magnetic field of 17.6 T. Samples were spun at 12.5 kHz and the chemical shift was measured respect to $CaCl_{2(aq)}$ 1M set at 0 ppm. For 3QMAS, a shifted-echo pulse

sequence was used [14]. Typically 8192 signals were accumulated with a recycle delay of 1s for each t1 point. 16 rotor-synchronized t1 increments (80 us) were collected for each 2D spectrum and processed using an in-house written software.

7.3. Comparing Experimental and theoretical data: validation of the models

Figure 7.1 shows the high field ^{43}Ca experimental 3QMAS and MAS spectra of the CAS, CASN and CSN glasses.

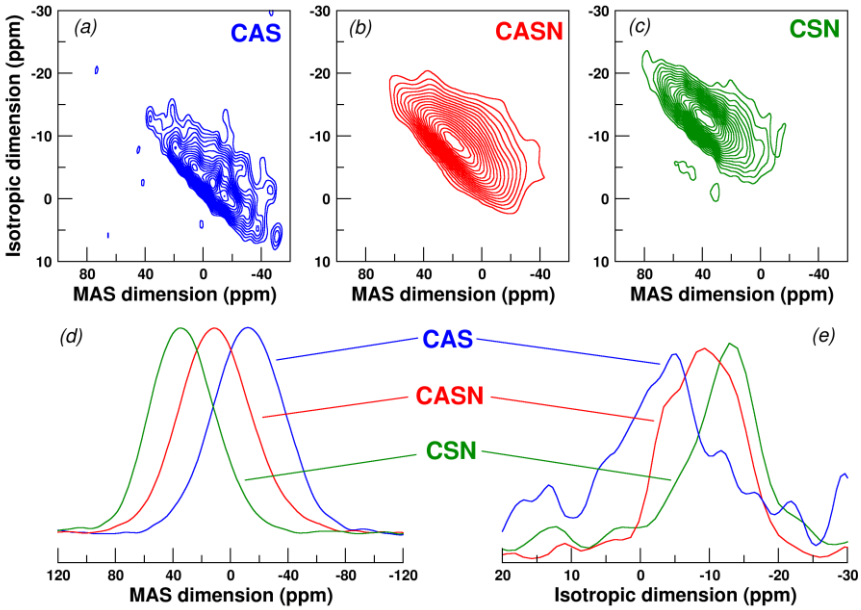

Figure 7.1. ^{43}Ca 3QMAS experimental spectra for CAS (a), CASN (b) and CSN (c) glasses; MAS spectra (d) and isotropic projections (e).

On one hand, the shape of MAS spectra (**Figure 7.1.d**) and isotropic projections, (**Figure 7.1.e**) are rather similar but widths are slightly different, suggesting similar but not identical ordering of Ca short-range environments in the three compositions. On the other hand, their positions are different, as observed in the previous study by Angeli et al [2]. The simulated spectra using the GIM and the inversion methods are also reported in **Figure 7.2** from which it is evident that the second method better reproduces the tails of the experimental spectra. It worth to note that a single line is observed on the MQMAS spectra for all compositions, especially for the CASN glass.

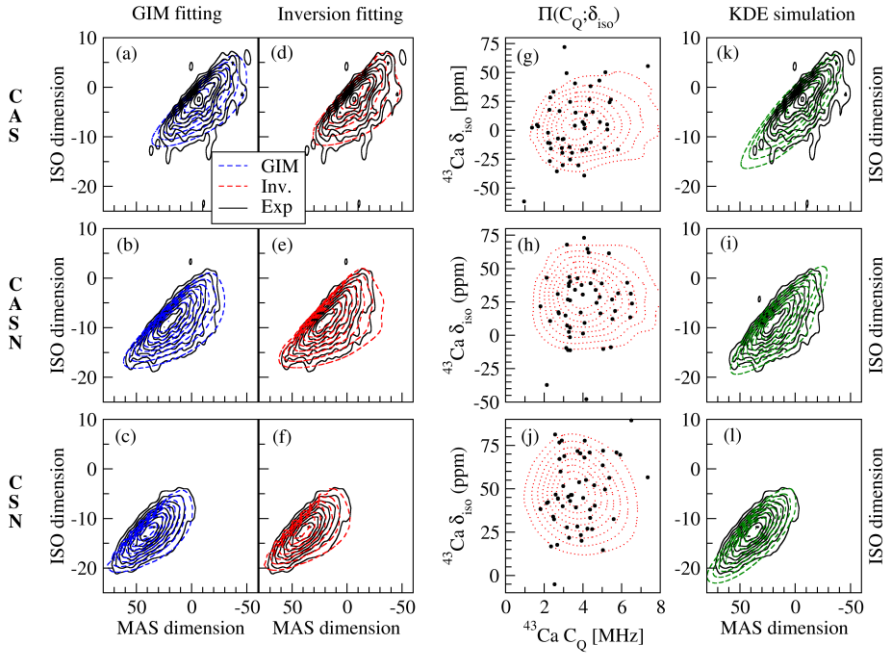

Figure 7.2. ^{43}Ca 3QMAS experimental spectra (solid lines) for CAS, CASN and CSN glasses are compared to spectra simulated by using the GIM (panels a, b, c) and the inversion (panels d, e, f) fitting procedures. Panels g, h, j report the comparison of the experimental (dotted lines) and MD-GIPAW (full circles) $\Pi(C_Q;\delta_{iso})$ distributions. Panels k, i, l report the comparison of experimental and MD-GIPAW (dashed lines) ^{43}Ca 3QMAS spectra.

Figure 7.2 shows both experimental and theoretical NMR parameter distributions $\Pi(C_Q; \delta_{iso})$ (panels g, h and j). The former are extracted with the inversion method from experimental MQMAS spectra, the latter results from MD-GIPAW calculations. Since the agreement of the two counterparts is very good for CAS and CASN and good for CSN, we can conclude that these models reproduce the vast majority of the chemical environments experienced by Ca in our samples. A further confirmation of the soundness of the MD-derived models is provided by the fact that theoretical MD-GIPAW ^{43}Ca 3QMAS spectra (simulated with Kernel Density Estimation formalism) fit satisfactorily the experimental spectra, as shown in panels (k), (i) and (l).

The distributions of ^{43}Ca isotropic chemical shift (^{43}Ca δ_{iso}) for the CAS, CASN and CSN glasses extracted by using both the GIM and the inversion fitting methods are displayed in **Figure 7.3**. The width of ^{43}Ca δ_{iso} distributions are rather similar. In summary, ^{43}Ca C_Q does not provide valuable information on the role played by Ca.

However, an in-depth analysis of the MD-derived structural features is justified by the good agreement between MD-GIPAW and the experimental NMR parameter distributions. This also allows to investigate NMR/structural relationships.

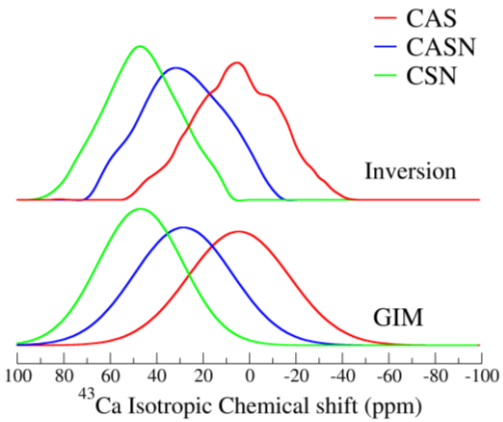

Figure 7.3. Distribution of ^{43}Ca isotropic chemical shift (^{43}Ca δ_{iso}) for the three compositions: a comparison between the GIM and the inversion fitting methods.

7.4. Correlations between ^{43}Ca NMR parameters and Ca local structural features

In analogy to the correlations found between ^{23}Na δ_{iso} and <Na-O> in silicate crystals, [15,16] both experimental and computational works presented correlations between ^{43}Ca δ_{iso} and <Ca-O> [4,5,17–19] or Ca coordination number (CN) [18,19] in crystalline samples. However, in 2010 Pedone et al. [12] studied the $CaSiO_3$ glass and demonstrated that ^{43}Ca δ_{iso} barely correlates with Ca CN and <Ca-O> distances, and that only qualitative trends can be pointed out. Beside the lack of effective correlations, experimental uncertainties for ^{43}Ca NMR usually make NMR parameter distributions very close in shape and in width, making the associated structural information difficult to extract. Nonetheless, mean values of experimental δ_{iso} distributions extracted with the inversion fitting method (**Figure 7.3**) evidence that Ca experiences different short-range environments, which can be ascribed to different CN distributions. A confirmation derives from MD-derived models, where Ca CN is 5.7, 5.8 and 5.3 for CAS, CASN and CSN glasses, respectively (**Table 7.1**).

Table 7.1. Average ^{43}Ca C_Q and δ_{iso} fitted from 3QMAS spectra (^{exp}) and calculated on MD-derived models (^{comput}), fitting errors and standard deviations on (^{comput}) values are in parenthesis.

Glass	$^{exp}C_Q$ [MHz]	$^{comput}C_Q$ [MHz]	$^{exp}\delta_{iso}$ [ppm]	$^{comput}\delta_{iso}$ [ppm]	fitting error	^{MD}<Ca-O> [Å]
CAS	3.7 (1.1)	3.6 (1.2)	6 (18)	5 (27)	11%	2.53 (0.20)
CASN	3.8 (1.2)	4.1 (1.2)	29 (17)	24 (25)	3%	2.50 (0.20)
CSN	2.6 (1.2)	3.7 (1.2)	47 (18)	50 (21)	5%	2.43 (0.15)

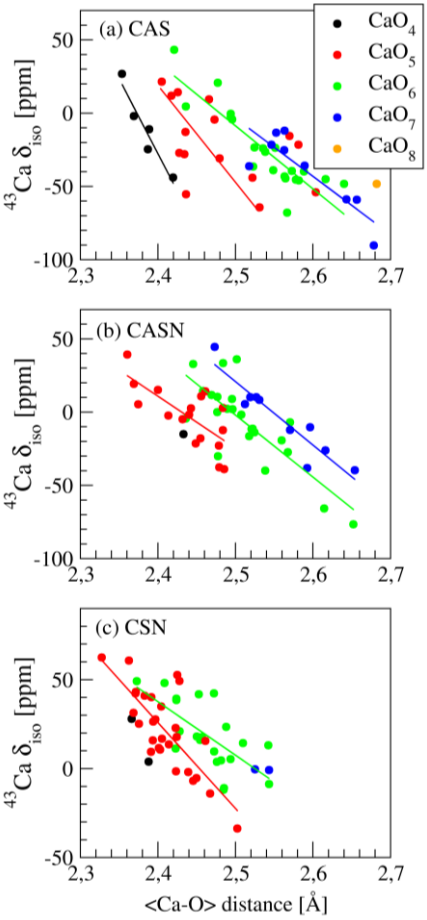

Figure 7.4. Theoretical ^{43}Ca δ_{iso} versus <Ca-O> bond distances as a function of Ca CN for CAS (a), CASN (b) and CSN (c) glasses. Trend lines are presented in coherent colours for most populated CN sites.

More in detail, CSN glass exhibits mostly 5- (51.9%) and 6-coordinated (40.7%) Ca, CASN glass presents significantly populated 5- (33.3%), 6- (45.1%) and 7-coordinated (19.6%) Ca atoms, and all coordination numbers from 4 to 8 are populated in the CAS glass.

Amorphous computational models provide a wide variety of chemical environments experienced by ^{43}Ca, thus a higher number of points with respect to crystals. Under these conditions, the reliability of the aforementioned correlations can be verified. As in a previous work [12], ambiguous trends between ^{43}Ca C_Q and Ca first coordination shell (data not reported) are observed, even though ^{43}Ca C_Q tends to slightly decreases with CN.

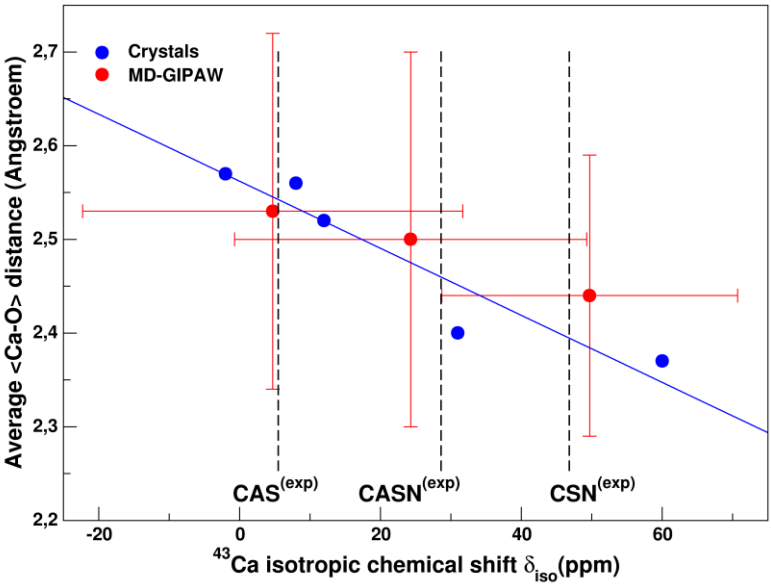

Figure 7.4. Distribution of the ratio X = n°BOs/CN of Ca ions for the CAS, CASN and CSN glasses.

However, in line with the results presented in **Chapter 6** for ^{23}Na, the correlation between δ_{iso} and <Ca-O> substantially improves when CN is expressly taken into account (**Figure 7.4**). Unluckily, the signal/noise ratio of the acquired ^{43}Ca 3QMAS spectra do not allow us to fit the experimental data and to obtain an estimation of the population of different Ca CN sites, as also proposed in **Chapter 6** for Na in glasses. This impedes us to evaluate <Ca-O> by using a bivariate correlation.

However, MD simulations provide <Ca-O> and reveals that it becomes shorter moving from CAS (2.53 Å) to CSN (2.43 Å), showing an intermediate values in CASN glass (2.50 Å). This trend is reflected in an increases of the δ_{iso} from CAS to CSN passing through the CASN glass. These results are in good agreement with the ones reported by Angeli et al.[12], who estimated a

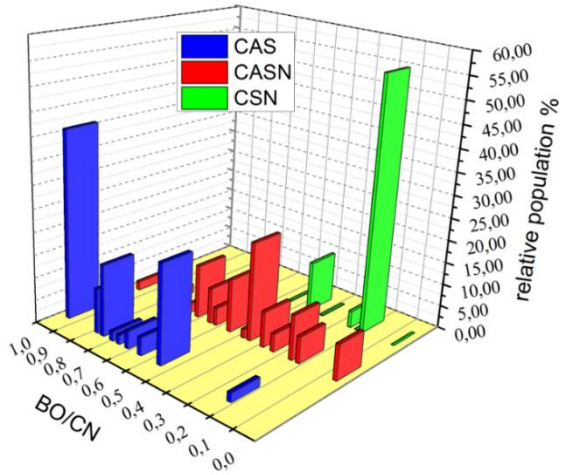

Figure 7.5. Correlation between <Ca-O> and ^{43}Ca δ_{iso} elaborated on crystalline samples (blue). <Ca-O> from MD-derived models (red) and ^{43}Ca δ_{iso} obtained in this work from MQMAS spectra (dashed lines). For MD data, error bars represents width (standard deviation value) of the distribution.

<Ca-O> bond length of 2.58 Å, 2.47 Å and 2.36 Å for CAS, CASN and CSN glasses by exploiting an empirical correlation between ^{43}Ca δ_{iso} and <Ca-O> elaborated on crystalline samples [5] and reported as a blue line in **Figure 7.5**.

In the latter, the intersection between the vertical black dashed lines representing the values of ^{43}Ca δ_{iso} extracted in this work from MQMAS spectra and the blue lines provides an estimation of the average <Ca-O> distances in the glasses (2.54 Å, 2.46 Å, 2.40 Å for CAS, CASN and CSN respectively) which are very close to the values provided by MD-derived models.

7.5. Dependence of local structural features on Ca role

The variation of <Ca-O> with composition has to be ascribed to the different roles played by Ca in the compositions under study: network modifier in CSN, charge compensator in CAS, both roles in CASN. As a network modifier, Ca

depolymerizes the network and is coordinated mainly by NBOs, while when acting as network charge compensator Ca is allocated into polymerized network regions that need charge compensation for $[AlO_{4/2}]^-$, and is coordinated mainly by Bridging Oxygens (BOs). The quantification of the nature of the Ca role in the three glasses can be given by the ratio $X = n°BOs/CN$, which ranges between 0 and 1. When X = 1, all O around Ca are BO, thus Ca plays the role of a pure network charge compensator; when X = 0 all O around Ca are NBO, thus Ca plays the role of a pure network modifier.

Figure 7.6 reports the populations of the different X values in the three glasses. As expected, the distribution of X values is narrower for CAS and CSN glasses, and wider for CASN glass. The weighted average of X on the populations is 0.79 in the CAS glass, 0.45 in the CASN glass and 0.19 for the CSN glass. As previously discussed in **Chapter 6**, when Na and Ca are both present, Na prefers to act as network charge compensator when Al is present in the network. This behaviour was also pointed out in previous computational-experimental works [20,21]. Nonetheless, extended Ca/Na intermixing around NBOs in Ca-Na silicate, aluminosilicate and borosilicate glasses was proved by both experimental [22] and computational (**Chapter 5**) approaches.

7.6. Final remarks

The acquisition of ^{43}Ca MQMAS spectra allowed us to obtain, for the first time, a good set of NMR experimental data of the challenging ^{43}Ca nucleus in three silicate glass samples. Full δ_{iso} and C_Q distributions were provided by

the inversion fitting procedure with small fitting errors. The set of theoretical NMR parameters, calculated on sound structural models of the glasses, provided us a valuable data set to find out that ^{43}Ca δ_{iso} better correlates with <Ca-O> distances when CN is expressly taken into account, and to conclude that CN does not correlate with any NMR parameter. Nonetheless, the study of Ca coordination in glasses has been possible thanks to the structural models: CN distribution is sharper when Ca acts as charge compensator and wider when it acts as network modifier.

Bibliography

[1] Angeli F, Gaillard M, Jollivet P, Charpentier T. Influence of glass composition and alteration solution on leached silicate glass structure: A solid-state NMR investigation. Geochim Cosmochim Acta 2006;70:2577–90. doi:10.1016/j.gca.2006.02.023.

[2] Angeli F, Gaillard M, Jollivet P, Charpentier T. Contribution of 43Ca MAS NMR for probing the structural configuration of calcium in glass. Chem Phys Lett 2007;440:324–8. doi:10.1016/j.cplett.2007.04.036.

[3] Bryce DL. Calcium binding environments probed by 43Ca NMR spectroscopy. Dalton Trans 2010;39:8593. doi:10.1039/c0dt00416b.

[4] Gervais C, Laurencin D, Wong A, Pourpoint F, Labram J, Woodward B, et al. New perspectives on calcium environments in inorganic materials containing calcium–oxygen bonds: A combined computational–experimental 43Ca NMR approach. Chem Phys Lett 2008;464:42–8. doi:10.1016/j.cplett.2008.09.004.

[5] Dupree R, Howes AP, Kohn SC. Natural abundance solid state 43Ca NMR. Chem Phys Lett 1997;276:399–404. doi:10.1016/S0009-2614(97)00863-4.

[6] Angeli F, Delaye J-M, Charpentier T, Petit J-C, Ghaleb D, Faucon P. Influence of glass chemical composition on the Na–O bond distance: a 23Na 3Q-MAS NMR and molecular dynamics study. J Non-Cryst Solids 2000;276:132–44. doi:10.1016/S0022-3093(00)00259-3.

[7] Gambuzzi E, Charpentier T, Menziani MC, Pedone A. Computational interpretation of 23Na MQMAS NMR spectra: A comprehensive investigation of the Na environment in silicate glasses. Chem Phys Lett 2014;612:56–61. doi:10.1016/j.cplett.2014.08.004.

[8] Angeli F, Charpentier T, Faucon P, Petit J-C. Structural Characterization of Glass from the Inversion of ^{23} Na and ^{27} Al 3Q-MAS NMR Spectra. J Phys Chem B 1999;103:10356–64. doi:10.1021/jp9910035.

[9] Angeli F, Delaye J-M, Charpentier T, Petit J-C, Ghaleb D, Faucon P. Investigation of Al–O–Si bond angle in glass by 3Q-MAS NMR and molecular dynamics. Chem Phys Lett 2000;320:681–7. doi:10.1016/S0009-2614(00)00277-3.

[10] Laurencin D, Smith ME. Development of 43Ca solid state NMR spectroscopy as a probe of local structure in inorganic and molecular materials. Prog Nucl Magn Reson Spectrosc 2013;68:1–40. doi:10.1016/j.pnmrs.2012.05.001.
[11] Shimoda K, Tobu Y, Shimoikeda Y, Nemoto T, Saito K. Multiple Ca2+ environments in silicate glasses by high-resolution 43Ca MQMAS NMR technique at high and ultra-high (21.8T) magnetic fields. J Magn Reson 2007;186:156–9. doi:10.1016/j.jmr.2007.01.019.
[12] Pedone A, Charpentier T, Menziani MC. Multinuclear NMR of CaSiO3 glass: simulation from first-principles. Phys Chem Chem Phys 2010;12:6054–66. doi:10.1039/b924489a.
[13] Bureau B, Silly G, Buzaré J., Legein C, Massiot D. From crystalline to glassy gallium fluoride materials: an NMR study of and quadrupolar nuclei. Solid State Nucl Magn Reson 1999;14:181–90. doi:10.1016/S0926-2040(99)00027-2.
[14] Massiot D, Touzo B, Trumeau D, Coutures JP, Virlet J, Florian P, et al. Two-dimensional magic-angle spinning isotropic reconstruction sequences for quadrupolar nuclei. Solid State Nucl Magn Reson 1996;6:73–83. doi:10.1016/0926-2040(95)01210-9.
[15] George AM, Stebbins JF. High-temperature 23Na MAS NMR data for albite: Comparison to chemical-shift models. Am Min 1995;80:878–84.
[16] Xue X, Stebbins J. 23Na NMR chemical shifts and local Na coordination environments in silicate crystals, melts and glasses. Phys Chem Miner 1993;20. doi:10.1007/BF00215100.
[17] Bryce DL, Bultz EB, Aebi D. Calcium-43 Chemical Shift Tensors as Probes of Calcium Binding Environments. Insight into the Structure of the Vaterite $CaCO_3$ Polymorph by ^{43}Ca Solid-State NMR Spectroscopy. J Am Chem Soc 2008;130:9282–92. doi:10.1021/ja8017253.
[18] Lin Z, Smith M, Sowrey F, Newport R. Probing the local structural environment of calcium by natural-abundance solid-state Ca43 NMR. Phys Rev B 2004;69. doi:10.1103/PhysRevB.69.224107.
[19] Wong A, Laurencin D, Wu G, Dupree R, Smith ME. An Ab Initio Quantum Chemical Investigation of ^{43}Ca NMR Interaction Parameters for the Ca^{2+} Sites in Organic Complexes and in Metalloproteins. J Phys Chem A 2008;112:9807–13. doi:10.1021/jp801015y.
[20] Cormier L, Neuville DR. Ca and Na environments in Na2O–CaO–Al2O3–SiO2 glasses: influence of cation mixing and cation-network interactions. Chem Geol 2004;213:103–13. doi:10.1016/j.chemgeo.2004.08.049.
[21] Lee SK, Sung S. The effect of network-modifying cations on the structure and disorder in peralkaline Ca–Na aluminosilicate glasses: O-17 3QMAS NMR study. Chem Geol 2008;256:326–33. doi:10.1016/j.chemgeo.2008.07.019.
[22] Angeli F, Charpentier T, Molières E, Soleilhavoup A, Jollivet P, Gin S. Influence of lanthanum on borosilicate glass structure: A multinuclear MAS and MQMAS NMR investigation. J Non-Cryst Solids 2013;376:189–98. doi:10.1016/j.jnoncrysol.2013.05.042.

CHAPTER 8
Conclusions

This final chapter resumes the potentiality of the MD-GIPAW computational protocol and of the experimental-computational approach, and provides an overall descriptions of those glass structural features that were highlighted thanks to computational NMR spectroscopy and MD-derived models.

8.1. Interpretation and predictive ability of the MD-GIPAW method

NMR theoretical signal of specific sites, calculated over MD-derived glass models, allowed the identification of their spectroscopic fingerprints on MAS and MQMAS spectra. This information was exploited to determine which sites provide clearly recognizable signals on the spectra, and which sites do not because of their overlapping with other site signals.

In the latter case, NMR theoretical constraints were found to be critical in the quantification of species of interest. For example, in **Chapter 3** we highlighted that asymmetries in ^{29}Si MAS spectra are ascribable to the presence of different amount of Al atoms around Si atoms and, by fitting a ^{29}Si MAS spectrum with constraints provided by MD-GIPAW calculations, we were able to estimate network chemical disorder in the Na-aluminosilicate glass (MAS).

The interpretation ability of MD-GIPAW calculations was also exploited in **Chapter 4**, where the spectroscopic fingerprint of Al atoms bonded to TBOs were assigned to a shoulder in ^{27}Al MAS spectra. Analogously, Al-O-Al bridges were found to cause a broadening in ^{27}Al C_Q distributions towards higher

values. Another useful interpretation of NMR experimental data was described in **Chapter 5**. Here, an investigation on TBOs spectroscopic fingerprints in ^{17}O MQMAS confirms that NMR parameters of the OAl_2Si and $OAlSi_2$ sites fall in the same range of δ_{iso} and C_Q of OSi_2 and OSiAl sites, making TBO detection via ^{17}O NMR spectroscopy very unlikely. However, it was possible to demonstrate that NMR parameters of the OAl_3, where 2 Al are involved in a 2-membered ring, fall close to the edge of the main Si–O–Al peak; their signal occupies a distinct region of ^{17}O MQMAS spectra and are clearly detectable.

In **Chapter 6**, the interpretation ability of the method was exploited to determine the Na average coordination number in the CSN glass by constraining the fitting of experimental ^{23}Na 3QMAS spectra with the theoretical NMR values found for different NaO_n sites. It was then possible to estimate the experimental distribution of these sites and the average coordination number of Na ions, which is 5.5, in good agreement to the value provided by the MD model (5.6).

The predictive power of MD-GIPAW calculation lays in the ability to study direct correlations between NMR parameters and structural features. In **Chapter 3** we demonstrated that accurate correlations between <Si-O-T> angles and ^{29}Si δ_{iso} in glasses could be established as multivariate correlations that include, beyond the inter-tetrahedral angle, Q^n speciation and structural features concerning the nature of Si second coordination shell, Ca and Al. In **Chapter 4**, analogous conclusions were established about the correlation between the ^{27}Al δ_{iso} and Al-O-T angles. In this case, structural inversion using a well-known univariate correlations is a possible path, being Al speciated as Q^4 only.

The predictive power of the method also allowed us to conclude that all empirical correlation, elaborated on crystalline samples between ^{17}O, ^{23}Ca and

^{23}Na, and respective structural features, are not valid in glass sample. In particular, we mention here that linear correlation between ^{23}Na (or ^{43}Ca) δ_{iso} and <Na–O> (or <Ca–O>) is observed when different CNs are taken into account, and that network modifier cation average CN can be potentially estimated starting from high-quality ^{23}Na or ^{43}Ca δ_{iso} experimental data sets.

8.2. Improvement of structural characterization of glasses

The characterization of glass structure was mainly achieved by consulting MD-derived models, which soundness was verified by comparing MD-GIPAW results with experimental counterparts.

Regarding network former cations, Si and Al, we found that aluminosilicate glasses exhibit Al(Q^4) species and that Al clustering is lower than that expected for a random network chemical disorder. Si-O-Al bridges are statistically preferred with respect to Al-O-Al bridges, however our models confirm that Lowenstein's rule is not respected in glasses. Moreover, we could observe that Si-O-Al bridges are preferentially formed between Al and Si(Q^4) species.

Extra-framework cations location around network former cations was found to be not randomized. In fact, when both Ca and Na are present in the composition, Ca prefers to allocate in Si(Q^1) and Si(Q^2) surroundings, while Na is mainly localized around Si(Q^3) and Si(Q^4) units. Ca and Na exhibit different behavior even in terms of allocation around Si or Al. When Ca and Na are both present in aluminosilicate compositions, Na tends to occupy Al surroundings, thus it preferably behaves as the *charge compensator* of tetrahedral $(AlO_{4/2})^-$, while Ca tends to occupy Si depolymerized regions, then acting as *network modifier*.

The study of Oxygen surroundings provided more information on extra-framework cations environment and confirms the results on network former cations. The results clearly indicate that there is extensive mixing of Ca and Na around NBOs in soda-lime silicate glasses. Here, the amount of Si–NBO(Na,Ca) sites is higher than that predicted by employing a random distribution of cations around NBO, whereas the amount of NBO coordinated to only one of the Na or Ca species is lower.

TBOs appear in CAS (4.9 %) and NAS models (1.7%). Although their presence in MD-derived models is overestimated with respect to glass samples, we deduced that higher field strength cations (Ca^{2+} > Na^{+}) promote the formation of NBO and TBO because of the competition for low-coordination states. Instead, all the NBOs present in the three glasses are associated with Si atoms rather than Al ones.

In the two chapters dedicate to Ca and Na, MD-derived models were decisive to evaluate coordination numbers and to highlight any trend with respect to glass composition and cation role. Ca and Na average CNs do not vary significantly with the composition. However, the Ca CN distribution was found sharper when Ca acts as charge compensator (CAS) and wider when it acts as network modifier (CSN). About Na coordination, the speciation of O atoms in BOs and NBOs confirms previous hypotheses that see Na^{+} playing a charge compensator role in CASN and a network modifier role in CSN.

Figure 8.1 shows a snapshot of the CASN MD-derived model, where many of the structural features of aluminosilicate glasses summarized above are showed: Al-O-Si linking in the network, Calcium atoms (green spheres) allocated close to depolymerized silica domains of the network and Sodium atoms (violet spheres) allocated close to $(AlO_{4/2})^{-}$ tetrahedra.

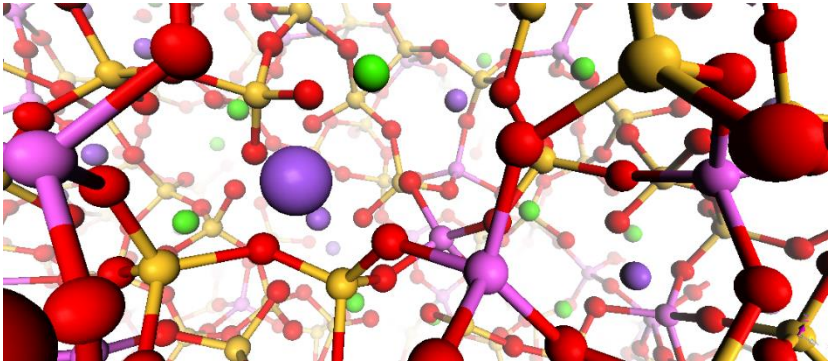

Figure 8.1. Structural model of CASN glass: Si atoms are yellow spheres, Al are light violet spheres, O are red spheres and Ca and Na are green and violet spheres. The following structural featured are shown: Al-O-Si linking in the network, Calcium atoms (green spheres) allocated close to depolymerized silica domains of the network and Sodium atoms (violet spheres) allocated close to $(AlO_{4/2})^-$ tetrahedra.

8.3. Future perspectives

The interpretative and predictive abilities of the DFT-GIPAW method, when coupled to experimental data, have been largely demonstrated. This encourages the employment of the method for other families of multicomponent glasses for a detailed characterization of their short- and medium-range environment.

However, the method itself needs improvements on both computational efficiency of DFT calculations and theoretical formalism.

In fact, lower computational costs would allow to get wider sets of theoretical spectroscopic and structural data, which could be obtained by generating larger models. These sets would be an ideal starting point for the evaluation of those multivariate correlations that are necessary to perform reliable *structural inversions* of NMR experimental data sets to achieve structural information directly from NMR spectra.

Moreover, we saw in **Chapter 6** that ^{23}Na C_Q values are systematically overestimated because vibrational ways of degrees of Na at 300 K cannot be taken into account by the protocol. Thus, there is a clear need for developing and implementing computational strategies capable of taking into account even those motions that NMR is sensitive to, like micro/millisecond time motions. A further improvement of DFT-GIPAW needs to account for relativistic effects, making the design of improved XC functional a key task.

The combination of MD and GIPAW calculations holds a promising prospect for providing both structural and dynamical information in solids.

Acknowledgements

My sincere thankfulness goes to my supervisor, Alfonso Pedone, who encouraged me to move steps along the way of graduate studies and taught me all the things I know about computational chemistry. Prof. M. Cristina Menziani is also acknowledged for her supervision activity. My gratitude even goes to Thibault Charpentier, who hosted me in his laboratory during 9 month and gave me a precious teaching about experimental and theoretical aspects of solid state NMR.

I thank Davide and Giulia, two colleagues whose company had been precious.

Finally, I thank my family for supporting me and for taking pride in me, which definitely is the most important achievement of my life.

Appendix A

Calculation of random population of the species Al(Q^4)[*j*Si,*4-j*Al].

Calculating Random Population (RP) of Al(Q^4)[*j*Si,*4-j*Al] species means to evaluate random distribution of *b*Al and *c*Si atoms around an Al(Q^4) atom. RP are given by multiplying combination weigh (CW) of the considered distribution by the sum of populations of all the species surrounded by the same number $n = b + c$ of former cations (SUM_n).

$$RP = CW \cdot \mathrm{SUM}_n = a \cdot {\chi_{\mathrm{Si}}}^{\mathrm{c}} \cdot {\chi_{\mathrm{Al}}}^{\mathrm{n-c}} \cdot \mathrm{SUM}_n$$

where χ_{Al} and χ_{Si} are the molar ration of Al and Si atoms respect to the total amount of network former atoms. and *a* is the binomial coefficient of the distribution:

$$a\left(\frac{n}{c}\right) = \frac{n!}{c!\,(n-c)!}$$

By definition. Al(Q^4) are bonded to bridging oxygens only. thus must be always surrounded by 4 network formers. This implies that all the species we are investigating are characterized by the same value of $n = 4 = (4\text{-}j) + j$. hence SUM_n is equal to 1 and RP coincide to CW:

$$RP = a \cdot {\chi_{\mathrm{Si}}}^{\mathrm{j}} \cdot {\chi_{\mathrm{Al}}}^{4-\mathrm{j}}$$

For example, the molar composition percentage of CASN glass is 60.0% SiO_2·10.0% Al_2O_3·10.0% Na_2O·20.0% CaO and molar ratio of Al and Si are:

$\chi_{Al} = (2 \cdot 10.0/(2 \cdot 10.0+60.0)) = 0.25$

$\chi_{Si} = 1-\chi_{Al} = 0.75$

There are 5 possible distribution of Al and Si around a Al(Q^4) atom, each of them associable to a Al(Q^4)[*j*Si,*4-j*Al] species and characterized by a binomial coefficient, *a*, and by a RP:

- Al(Q^4)[*4*Si,*0*Al], $a = \frac{4!}{4!0!} = 1 \rightarrow RP = 1 \cdot 0.75^4 \cdot 0.25^0 =$ 0.316
- Al(Q^4)[*3*Si,*1*Al], $a = \frac{4!}{3!1!} = 4 \rightarrow RP = 4 \cdot 0.75^3 \cdot 0.25^1 =$ 0.422
- Al(Q^4)[*2*Si,*2*Al], $a = \frac{4!}{2!2!} = 6 \rightarrow RP = 6 \cdot 0.75^2 \cdot 0.25^2 =$ 0.211
- Al(Q^4)[*1*Si,*3*Al], $a = \frac{4!}{1!3!} = 4 \rightarrow RP = 4 \cdot 0.75^1 \cdot 0.25^3 =$ 0.047
- Al(Q^4)[*0*Si,*4*Al], $a = \frac{4!}{0!4!} = 1 \rightarrow RP = 1 \cdot 0.75^1 \cdot 0.25^4 =$ 0.004

Percentage Random Population (RP%) are given by: RP% = RP·100.

Appendix B

Formulae for the calculation of random distribution of Na and Ca around Oxygen atoms.

We consider the molar composition percentage of CSN glass: 60.0% SiO_2 – 20.0% Na_2O – 20.0% CaO and define χ_{Na} = (20.0/(20.0+20.0)) = 0.5 as the molar ratio of Na cations respect to the whole amount of modifier cations in the glass, while χ_{Ca} =1-χ_{Na} is the molar ratio of Ca.

We then calculate homogeneous distribution of modifier cations around BO and NBO. Firstly, it is necessary to determine the weight of a certain combination of modifiers around (N)BO, that means the probability of existence of a certain specie (N)BO-*b*Ca,*c*Na, where (*b*+*c*) = *n* is the total number of modifier cations around (N)BO.

$$\text{Combination Weigh} = a \cdot {\chi_{\text{Ca}}}^{n-c} \cdot {\chi_{\text{Na}}}^{c}$$

Where *a* is the binomial coefficient:

$$a\left(\frac{n}{c}\right) = \frac{n!}{c!\,(n-c)!}$$

The number so obtained is multiplied by a molar ratio of (N)BO coordinated by the same number *n* of modifier cations. Since we cannot know these ratio by calculating them from glass composition, we employ the sum of the MD population of each specie of (N)BO coordinated by *n* modifiers.

This means, still considering CSN glass, that the random population 1 Ca and 2 Na around NBO species is so calculated:

1) $a\left(\frac{3}{2}\right) = \frac{3!}{2!(3-2)!} = 3$
2) $\text{Combination Weigh} = 3 \cdot 0{,}5^1 \cdot 0{,}5^2 = 0{,}375$
3) Random Population = 0,375*(pop $_{\text{Si-NBO(3Na)}}$ + pop$_{\text{Si-NBO(3Ca)}}$ + pop$_{\text{Si-NBO(1Na,2Ca)}}$ + pop$_{\text{Si-NBO(2Na,1Ca)}}$) =

   = 0,375*(MDpop $_{\text{Si-NBO(3Na)}}$ + MDpop$_{\text{Si-NBO(3Ca)}}$ + MDpop$_{\text{Si-NBO(1Na,2Ca)}}$ + MDpop$_{\text{Si-NBO(2Na,1Ca)}}$)

Appendix C

Formulae for the calculation of random distribution of Al and Si around bridging Oxygen atoms.

We consider the molar composition percentage of NAS glass: 78.0% SiO_2 – 11.0% Na_2O – 11.0% Al_2O_3

We now have to define define $\chi_{Si} = 0.78$ and $\chi_{Al} = 0.22$

*b*Al-BO-*c*Si, where (*b*+*c*) = 2, as the 3 possible species are Al-O-Al, Al-O-Si and Si-O-Si; the binomial coefficient of the first one is:

$$a_{Al-O-Al}\left(\frac{2}{2}\right) = \frac{2!}{2!\,(2-2)!} = 1$$

And its combination weight:

$$\text{Combination Weigh Al} - \text{O} - \text{Al} = 1 \cdot 0.22^2 = 0.048$$

Then:

Random Population Al-O-Al = 0.048 · (pop $_{Al\text{-}BO\text{-}Al}$ + pop$_{Al\text{-}BO\text{-}Si}$ + pop$_{Si\text{-}BO\text{-}Si}$) = 0.048 · (pop $_{BO}$)

pop $_{BO}$ is known by the composition of the glass as χ_{BO}: in a tectosilicate glass, like CAS and NAS, according to the compensated continuum random network model, NBO are not present and we define $\chi_{BO} = 1$ and $\chi_{BO} = 0$.

Random Population Al-O-Al = 0.048 · χ_{BO} = 0.048 · 1

Please note that CASN glass composition (60.0% SiO_2 – 10.0% Na_2O – 10.0% Al_2O_3 – 20,0% CaO) implies the presence of NBO: χ_{BO} = 160/180 = 0,83 and χ_{BO} = 20/180 = 0,17.

List of Publications

1) "Evidence of Catalase Mimetic Activity in Ce^{3+}/Ce^{4+} Doped Bioactive Glasses" (**2015**) under revision for *J. Phys. Chem. B*; Valentina Nicolini, Elisa Gambuzzi, Gianluca Malavasi, Ledi Menabue, Maria Cristina Menziani, Gigliola Lusvardi, Alfonso Pedone, Francesco Benedetti, Paola Luches, Sergio D'Addato and Sergio Valeri.

2) "Calcium Environment in Silicate and Aluminosilicate Glasses Probed by ^{43}Ca MQMAS NMR experiments and MD-GIPAW calculations." (**2015**) submitted to *Solid. State Nucl. Mag.*; Elisa Gambuzzi, Alfonso Pedone, Maria Cristina Menziani, Frédéric Angeli, Pierre Florian and Thibault Charpentier

3) "Experimental and computational achievements on the immobilization of high-level nuclear wastes." (**2014**) *La Chimica e l'Industria,* 4, 51-52; Elisa Gambuzzi, Alfonso Pedone

4) "On the Structure of Ce-containing Silicophosphate Glasses: a Core-Shell Molecular Dynamics Investigation." (**2014**) *Phys. Chem. Chem. Phys, 16*, 21645-21656; Elisa Gambuzzi and Alfonso Pedone

5) "Computational interpretation of ^{23}Na MQMAS NMR Spectra: a comprehensive investigation of the Na environment in silicate glasses" (**2014**) *Chem. Phys. Lett.* 612, 56-61; Elisa Gambuzzi, Thibault Charpentier, Maria Cristina Menziani and Alfonso Pedone

6) "Probing silicon and aluminium chemical environments in silicate and aluminosilicate glasses by solid state NMR spectroscopy and accurate first-principles calculations" (**2014**) *Geo. Cosmo. Acta*, 125, 170-185; Elisa Gambuzzi, Alfonso Pedone, Maria Cristina Menziani, Frédéric Angeli, Daniel Caurant, Thibault Charpentier.

7) “Understanding the photophysical properties of coumarin-based Pluronic-Silica (PluS) nanoparticles by means of time-resolved emission spectroscopy and accurate TDDFT/stochastic calculations.” (**2013**) *Phys. Chem. Chem. Phys.*, 15, 12360-12372; Alfonso Pedone, Elisa Gambuzzi, Vincenzo Barone, Sara Bonacchi, Damiano Genovese, Luca Prodi, Enrico Rampazzo, Marco Montalti.

8) “Unambiguous Description of the Oxygen Environment in Multicomponent Aluminosilicate Glasses from 17O Solid State NMR Computational Spectroscopy” (**2012**) *J. Phys. Chem. C*, 116, 14599-14609; Alfonso Pedone, Elisa Gambuzzi, Maria Cristina Menziani.

9) “First-principles simulations of the 27Al and 17O solid-state NMR spectra of the $CaAl_2Si_3O_{10}$ glass” (**2012**) *Theor. Chem. Acc*., 131, 1-11; Alfonso Pedone, Elisa Gambuzzi, Gianluca Malavasi, Maria Cristina Menziani